The effects of porosity clogging on the transport properties of porous materials under geochemical perturbation

Experimental approach and modeling

A dissertation
Submitted in partial fulfillment of the Requirements for the
Degree of Doctor of Natural Science (Dr. rer. nat.)

To the department of
"Fachbereich Geowissenschaften der Freien Universität Berlin"

by
Aurélie M. CHAGNEAU

Berlin, 2015

Supervisor: Prof. Dr. Habil. Thorsten Schäfer
Second Examiner: Prof. Dr. Michael Schneider

Date of Defense: 15.07.2015

Declaration of authorship

I herewith declare that I autonomously carried out the PhD thesis entitled *"The effects of porosity clogging on the transport properties of porous materials under geochemical perturbation. Experimental approach and modeling"*.

In appendix A of my PhD thesis is a publication which is already published. Below, the citation is given as well as the contributions of each authors.

Holliday, K.; Chagneau, A.; Schmidt, M.; Claret, F.; Schäfer, T. and Stumpf, T. (2012). *Discriminating factors affecting incorporation: comparison of the fate of Eu^{3+}/Cm^{3+} in the Sr carbonate/sulfate system.* Dalton Transactions, Vol. 41, pp. 3642-3647.

Kiel Holliday performed the TRLFS measurements and wrote the manuscript. I (Aurélie Chagneau) performed the co-precipitation experiments and help for the redaction of the experimental part. Moritz Schmidt, Francis Claret, Thorsten Schäfer and Thorsten Stumpf helped with the redaction and correction of the paper.

I did not receive any assistance in return for payment by consulting agencies or any other person. No one received any kind of payment for direct or indirect assistance in correlation to the content of the submitted thesis.

The thesis was conducted at the Karlsruhe Institute of Technology (KIT)/ Institute for Nuclear Waste Disposal (INE).

The thesis has not been submitted elsewhere for an exam, as thesis or for evaluation in a similar context.

I hereby affirm the above statements to be complete and true to the best of my knowledge.

Aurélie Chagneau

Acknowledgments

The author thanks dearly the many people - co-workers, collaborators, friends and family - without who the completion of this work would not have been possible. Namely,

- **Prof. Dr. Habil. Thorsten Schäfer**, my supervisor, for his constant support, help and deep engagement in this work.
- **Prof. Dr. Michael Schneider**, for presiding the jury, and for his much appreciated help and advices.
- **Dr. Francis Claret**, my advisor, for his helpful discussions and for teaching me the obscure ways of geochemical modeling with so much patience.
- **Dr. Claire Fialips** and **Dr. Benoît Madé**, my advisors from ANDRA, for their helpful discussions.
- **PD Dr. Frieder Enzmann** for providing us with gorgeous μCT data, and for teaching me how to analyze the data as well as for his priceless help in the analyzing procedures, and for giving me so much of his precious (CPU) time.
- **PD. Dr. Carl Steefel, Dr. Christophe Tournassat** and **Dr. Nicolas Marty** for the great help and teachings they provided for the geochemical modeling.
- The **INE analytic team**, and especially **Stephanie Heck**, for their patience and kindness in assisting me and the countless measurements they have performed.
- **Dr. Kiel Holliday** for his collaboration, advices and friendship; as well as his awesome wife, **Cheryl**. The great

evenings and week-end trips they organized in Baden-Württemberg will always be remembered.

- The **many students** who came and went in room 207c, and more especially **Andrea Kutzer** for her great friendship, sharing her experiences and for her (somewhat satirical) sense of humor that got me through more than one tough days.

- All dear friends and co-workers who were not named or especially cited.

Finally, to the very special people in my life: my parents, my sisters and my brother, and my significant other - *Thank you for everything.*

Abstract

To reliably predict contaminant migration through the geosphere and the biosphere a fundamental process understanding is prerequisite. To name a few of these processes: sorption/desorption, precipitation/dissolution, redox equilibrium/ disequilibrium, entrapment in mineral lattices by co-precipitation and matrix diffusion, colloidal transport, porewater diffusion, advective flow... Studying natural systems in which several, if not all, of these processes occur at the same time is very challenging. This is the reason why experimentalists tend to study simplified systems, where the contribution of individual parameters can be identified and quantified separately, until the complex interrelation of these processes is understood. Frequently, geochemical and reactive transport models are used to identify the contribution of each individual process involved and design experimental programs to verify the equations implemented. These models can later be used to predict contaminants migration in natural systems.

The work in hand focuses on the change of transport parameters during precipitation of simple salts (sulfates, carbonates) in porous media under diffusive conditions via monitoring of non-reactive (conservative) tracers. The main goal was to verify the general applicability of the relationship between porosity (ε) and effective diffusivity (D_e), and determine if the empirical Archie's law in its simplest form - $D_e/D_w = \varepsilon^m$, with D_w as free water diffusivity and m as fitting factor - is universally applicable in reactive systems. Sand was used as a simple but well-defined porous material, and non-swelling clay illite as a complex porous media possessing permanent negative charge. The initial transport parameters (D_e, ε, m, geometric factor) were quantified by several complementary experimental approaches: conservative tracer through diffusion (tritiated water), Mercury

Intrusion Porosimetry (MIP) and micro-Computed Tomography (μCT) coupled to a pore-morphology model. The methods used to estimate the transport parameters were in good agreement (e.g. porosity of 0.42 $\pm$ 0.09 with HTO tracing, 0.42 $\pm$ 0.02 with MIP and 0.40 $\pm$ 0.08 with μCT). One- and two-dimensions (1D/2D) continuum reactive transport models were developed with CrunchFlow and successfully calibrated on the through diffusion experimental data.

Then, a counter-diffusion method was used to precipitate celestite ($SrSO_4$) or calcite ($CaCO_3$) in the porous media. The evolution in diffusivity of the systems was followed by conservative radio-tracers: HTO and ^{36}Cl and in addition with ^{85}Sr in a lesser proportion.

The HTO flux during porosity clogging showed a reproducible behavior for both celestite and calcite precipitation: the flux first increased in proportions indicating no effects of porosity reduction, then decreased quickly when the first signs of precipitation were observed, and stabilized at a non-zero value. The steady state reached after the drop indicated that the pore space remained open, as part of the tracer was still diffusing through the precipitation front. The fronts were thin ($<$ 1 mm) white disks visible to the naked eye.

The porosity evolution was followed by imaging methods: μCT for the sand and autoradiography for the clay. A detailed μCT analysis of one diffusion cell confirmed that the pore space was still open and connected. The porosity in the front was reduced to a value of about 0.30, three quarters of the initial porosity. A pore morphology model applied to the 3D volume showed that this small porosity reduction had an impact on the tracer migration greater than anticipated. The most likely explanation was a drastically increased complexity of the diffusion path. In addition, the reacted medium and celestite precipitates were analyzed *post-mortem* (SEM-EDX and selective dissolu-

tion). The SEM-EDX images showed crystals in a wide range of sizes and morphologies arranged in different possible microporous aggregates. The aggregates filled the pore spaces and cemented the sand grains together.

The calibrated 1D continuum models were used on the experimental data in an attempt to reproduce the precipitation induced transport changes and develop a predictive model. The 1D continuum reactive transport models did not satisfactorily fit the experimental data. The reason could be an oversimplified D_e-ε relationship (Archie's law) using just one cementation factor and a more developed model based on an extended Archies law should be tested.

The clay material, a Na-exchanged and purified illite (illite-du-Puy), was well described in the literature. The initial transport parameters of the compacted illite (1700 $kg \cdot m^3$ dry density) have been determined to be $\varepsilon \approx$ 0.40-0.60, HTO-$D_e \approx$ 1.8-2.0$\times 10^{-10}$ $m^2 \cdot s^{-1}$, ^{36}Cl-$D_e \approx$ 0.7-1.1$\times 10^{-10}$ $m^2 \cdot s^{-1}$. Celestite was precipitated in the pore space of two samples. The HTO flux ($\approx 6.7\times 10^{-9}$ $m \cdot s^{-1}$) was about 2 times lower than for an undisturbed sample ($\approx 1.3\times 10^{-8}$ $m \cdot s^{-1}$) used as a reference. It was constant for the duration of the experiments (360 days). The ^{36}Cl flux was much different than the reference flux: the through diffusion was delayed by 18 days, stayed at a very low value for 57 days, and decreased below detection limits for the rest of the experiment. These results were interpreted as a full clogging of the anions accessible porosity, while the smaller pores - negatively charged and therefore inaccessible to anions - remained fully open and available for the neutral species and cations diffusion. The porosity in the precipitation front ($\approx$ 0.29) of the sample analyzed by autoradiography was reduced by half of its initial value ($\approx$ 0.53). This should correspond to the portion of the porosity accessible to anions.

As for the sand systems, the 1D and 2D continuum reactive

transport models could not reproduce the experimental data. Therefore, continuing work should include:

1. a realistic pore space geometry implementation in a 2D or 3D pore scale model,
2. the consideration of more complex kinetics (e.g. nucleation and surface growth, inhibition processes and critical saturation indexes) as well as
3. the implementation of different pore water types and the permanent clay surface charges inducing ion specific accessible porosity in the compacted clay system.

Zusammenfassung

Zuverlässige Aussagen zum Schadstofftransport und der Mobilität von Gefahrstoffen durch die Geosphäre und Biosphäre erfordern ein grundlegendes Verständnis der kontrollierenden Prozesse; um nur einige hier zu nennen: Sorption/Desorption, Mineralfällungs und Auflösungsvorgänge, Redoxprozesse inklusive deren Kinetiken, Matrix-Diffusion, kolloidalen Transport, Porenwasserdiffusion, advektiven Fluss...

Das Studium des Schadstofftransports in natürlichen Systemen zur Erlangung eines fundamentalen Prozessverständnisses ist oftmals dadurch erschwert, dass mehrere der oben genannten Prozesse parallel ablaufen und eine klare Differenzierung sehr anspruchsvoll wenn nicht sogar unmöglich ist. Dies ist einer der Hauptgründe, warum oftmals in einem sogenannten "Bottom-up" Ansatz Experimentatoren in vereinfachten Systemen den Beitrag einzelnen Prozesse/Parameter identifizieren und separat quantifizieren. Häufig werden geochemische und reaktive Transportmodelle verwendet, um über Parametervariation den Beitrag jedes einzelnen beteiligten Prozesses zu identifizieren und somit auch experimentelle Versuchsprogramme zu gestalten, um die implementierten oftmals auch auf empirischen Zusammenhängen basierenden Gleichungen zu überprüfen. Solche validierten reaktiven Transportmodelle ermöglichen dann die zuverlässige langfristige Prognose der Schadstoffmobilität in der Umwelt.

Die hier vorgestellte Arbeit fokussiert auf die Veränderung der Transportparameter während der Ausfällung einfacher Salze (Sulfate, Carbonate) in porösen Medien unter diffusionskontrollierten Bedingungen. Das Hauptziel der Arbeit ist es, die allgemeine Anwendbarkeit der Beziehung zwischen Porosität (ε) und effektivem Diffusionskoeffizient (D_e) unter diesen transienten Bedingungen zu quantifizieren und festzustellen, ob die empirischen Archie-Gleichung in ihrer einfachsten Form - $D_e/D_w = \varepsilon^m$,

mit D_w als ionenspezifischer Diffusionskoeffizient im freies Wasser und m als Anpassungsfaktor - universell in reaktiven Transportsystemen anwendbar ist.

Sand wurde als einfaches, aber gut definiertes poröses Material und ein nicht-quellfähiges Tonmineral (Illit) als ein komplexes poröses Medium mit permanenter negativer Schichtladung verwendet. Die initialen Transportparameter (D_e, ε, m, geometrische Faktor) wurden mittels komplementärer experimenteller Ansätze quantifiziert: Diffusion konservativer Tracer (tritiiertes Wasser; HTO), Quecksilber-Porosimetrie (MIP) sowie Mikro-Computertomographie (μCT) und Einbindung in ein Poren-Morphologie-Modell (GeoDict). Die eingesetzten Methoden zur Abschätzung der initialen Transportparameter des gewählten porsen Mediums (Sand) zeigten ein sehr gute Übereinstimmung (z.B. Porosität von 0,42 $\pm$ 0,09 mittels HTO, 0,42 $\pm$ 0,02 mit MIP und 0,40 $\pm$ 0,08 mit μCT). Ein- und zweidimensionale (1D/2D) Kontinuum Modelle zum reaktiven Transport wurden mit CrunchFlow entwickelt und erfolgreich auf Basis der konservativen Tracerdaten kalibriert.

In einem nächsten Schritt sind Gegendiffusionsexperimente zur Ausfällung von Coelestin ($SrSO_4$) oder Calcit ($CaCO_3$) in diesem porösen Medium durchgeführt worden. Die Entwicklung der Diffusivität des Systems wurde durch die konservative Radio-Tracer HTO bzw. ^{36}Cl verfolgt und zusätzlich in einigen Versuchen ^{85}Sr eingesetzt. Der HTO Diffusionsfluss während der Porenraumverstopfung (Clogging) zeigte ein reproduzierbares Verhalten sowohl für induzierte Coelestin- als auch Calcit-Fällung: (1) Die Durchflussmenge erhöht sich ver-gleichbar zu dem nicht reaktiven System und weißt keine Effekte einer Porenraumreduktion auf und (2) fällt beim ersten Anzeichen einer Präzipitation schnell ab und stabilisiert sich auf einem über Null liegenden Wert. Der erreichte stationäre Zustand nach dem Abfall des Durchflusses deutet darauf hin, dass der Porenraum

offen bleibt und der konservative Tracer trotz gebildeter Präzipitationsfront weiterhin diffundieren kann. Die Präzipitationsfront ist dünn (< 1 mm) und als solche mit dem bloßen Auge im experimentellen Plexiglas- Aufbau erkennbar. Die Porositätsentwicklung wurde durch bildgebende Verfahren verfolgt: μCT für den Sand und Autoradiographie für den kompaktierten Illit. Die detaillierte μCT Analyse einer Diffusionszelle bestätigt, dass der Porenraum unter der μCT Auflösung (5,89 μm) noch offen und zu 100% verknüpft ist (keine Dead-End Poren). Die Porosität in dieser Präzipitati-onsfront reduziert sich auf etwa 0.30, und somit drei Viertel der ursprünglichen Porosität. Ein auf das 3D Volumen angewandtes Poren Morphologie Model zeigte eindeutig, dass diese geringe Porositätsreduktion eine größere Auswirkung auf den Tracertransport als erwartet hat. Die hierfür plausible Erklärung ist eine signifikant erhöhte Komplexität des Diffusionspfads (Tortuosität). Zusätzlich wurde das reagierte Medium und die Coelestin Präzipitate *post-mortem* mittels REM-EDX und selektivem Säureaufschluss analysiert. Die REM-EDX-Bilder zeigten Kristalle in einer Vielzahl von Größen und Morphologien in verschiedenen möglicherweise auch mikroporösen Aggregaten angeordnet.

Die kalibrierten 1D Kontinuum Modelle der initialen Transporteigenschaften des Sand wurden in einem nächsten Schritt auf die experimentellen Daten angewandt, um die Mineralausfällungs- induzierten Transportparameteränderungen zu reproduzieren und ein Prognosemodell zu entwickeln. Die 1D Kontinuum reaktive Transportmodelle konnten nicht zufriedenstellend die experimentellen Daten anpassen. Der Grund hierfür ist die zu grob vereinfachte D_e-ε Beziehung (Archie-Gleichung) mit der Verwendung von nur einer Zementierung-Faktor m und weiterführende Arbeiten müssen auf eine Modellentwicklung fokussieren, in der eine erweiterten Archie-Gleichung getestet wird.

Bezüglich des Transport im kompaktierten Ton wurde als

Tonmineral, ein Na-ausgetauschter und aufgereinigter Illit (Illite-du-Puy) verwendet, der bereits in der Literatur sehr gut beschrieben ist. Die initialen Transportparameter des verdichteten Illit (1700 kg$\cdot m^{-3}$ Trocken-dichte) wurden mit $\varepsilon \approx$ 0,43-0,60, HTO-$D_e \approx$ 1,8-2,0 $\times 10^{-10}$ $m^2 \cdot s^{-1}$, ^{36}Cl-$D_e \approx$ 0,7-1,1 $\times 10^{-10}$ $m^2 \cdot s^{-1}$ bestimmt. Coelestin wurde im Porenraum von zwei kompaktierten Illit-Proben gefällt. Der HTO-Fluss im Falle der Präzipitation war mit $\approx 6.7 \times 10^{-9}$ $m \cdot s^{-1}$ ungefhr um die Hlfte im Vergleich zur ungestrten Referenzprobe $\approx 1.3 \times 10^{-8}$ $m \cdot s^{-1}$ reduziert und blieb im weiteren Verlauf des Experiments über 360 Tage konstant. Das Verhalten im Anionen-Transport (^{36}Cl) war jedoch deutlich unterschiedlich zum Referenzsystem: das ^{36}Cl Signal konnte in den Durchdiffusionsexperimenten erst mit 18 Tagen Verzögerung gemessen werden und blieb auf einem sehr niedrigen Fluss für weitere 57 Tage bevor es auf einen Wert unterhalb der Nachweisgrenze für den Rest der experimentellen Laufzeit abfiel. Diese Ergebnisse können als eine volle Verstopfung (Clogging) der Anionen verfügbaren Porosität interpretiert werden, währendem die kleineren Poren - negativ geladen und daher unzugnglich fr Anionen - völlig offen sind und weiterhin für die Diffusion neutraler Spezies und Kationen zur Verfügung stehen. Die in der Fällungsfront durch Autoradiographie an der Probe bestimmte Porosität von $\approx$ 0,29 entspricht etwa der Hälfte der ursprünglichen Porosität von $\approx$ 0,53 und stimmt gut mit dem Anteil an Anionen-zugänglichen Porosität in Referenzexperimenten überein.

Wie für die Sandsysteme konnten die 1D- und 2D-Kontinuum reaktiven Transportmodelle auch hier nicht die experimentellen Daten reproduzieren. Daher sollten zukünftige Arbeiten folgende Punkte näher untersuchen;

1. Realistische Porenraumgeometrie-Implementierung in 2D-/3D-Porenskalenmodellen,

2. die Berücksichtigung auch komplexerer Kinetiken (z.B. Keimbildung und Oberflächen-wachstum, Inhibierungsprozesse und kritische Sättigung Indizes) sowie

3. die Umsetzung der verschiedenen Porenwasserarten und die Permanentladung der Tonmineraloberflächen induzierten ionenspezifische zugängliche Porosität im kompaktierten Ton.

Contents

List of Tables

List of Figures

Introduction

The diffusion of conservative radio-tracers (HTO, ^{36}Cl and ^{85}Sr) through simplified porous media (compacted sea sand and purified illite) was followed during porosity reduction by precipitating simple salts ($SrSO_4$ and $CaCO_3$). The main goal was to describe the relationship between porosity (ε) and effective diffusivity (D_e), and determine if Archie's law was applicable to reactive and heterogeneous systems.

General context

The migration of contaminants through the geosphere towards the biosphere and drinking water reservoirs is an important subject of study in many fields. Contaminants can be dissolved green-house gases in the case of CO_2 storage (Wasch et al., 2013), heavy metals and acidic fluids in the case of acid mine drainage remediation (Ayora et al., 2013), radio-nuclides in the case of hydrothermal systems (Guarracino et al., 2014; Steefel and Lasaga, 1994) and high level nuclear wastes repositories (Liu et al., 2014; Xie et al., 2011), or a combination of many in the case of permeable reactive barriers efficiency (Indraratna et al., 2014).

The dissolved contaminants migrate in the geosphere via two main mechanisms: fluid flow in pores and fractures and/or molecular diffusion in the pore network of low hydraulic conductivity rocks. The impact of geochemical reactions on these con-

taminants transport must be assessed in order to predict the evolution of contamination fronts with time. The main geochemical reactions influencing the transport of dissolved species are: (1) sorption/desorption processes, (2) uptake in minerals by lattice diffusion and co-precipitation and (3) precipitation-recrystallization/dissolution. These processes are highly dependent on the fluids geochemical conditions (redox, pH, ionic strength, composition, temperature). The first two processes influence directly dissolved species transport, while the last one influences the migration indirectly by changing the pore space geometry (e.g. porosity, tortuosity).

Motivation and description of the work

Archie's law and similar relationships were mainly derived from non-continuous measurements in homogeneous and simple porous media (e.g., compacted sands and/or beads, sandstones, limestones). The powders grain sizes and compaction states were varied to vary porosity. In the case of gaseous diffusion, the materials were partly saturated with water to vary accessible porosity. Even for such simple systems, strong derivations from Archie's law were observed at low porosity (< 0.20, Ioannidis et al. (1997)). Very few experiments were performed on geochemically disturbed media, where the porosity was varied by partial dissolution of the mineral phases (Molins et al., 2014; Navarre-Sitchler et al., 2009). No published experimental works described continuous diffusion experiments during porosity changes (precipitation or dissolution).

To better understand the diffusivity response of a porous material to geochemical perturbations - and considering the previous observations - it appears necessary to perform continuous diffusivity measurements on various porous media during porosity variations. In a first time, a very simple system was studied:

purified sea sand compacted in laboratory. Its mineralogical composition and petro-physical properties were characterized. The two main methods used to quantify the initial transport parameters and follow the evolution of porosity and diffusivity during porosity clogging were: (1) conservative radio-tracer through diffusion and (2) micro-Computed Tomography (μCT) coupled to pore-morphology modeling:

1. The through diffusion method uses double reservoir diffusion in transient conditions experiments (Boving and Grathwohl, 2001; VanBavel, 1952; VanLoon et al., 2003a) to directly estimate the effective diffusivity and porosity from the experimental data. Combined to the counter-ion diffusion method, the precipitation of salts in the pore space of the material can be controlled (Prieto et al., 1997, 2002).

2. μCT coupled to pore morphology modeling is a powerful and non-destructive analysis tool that gained increasing interest in the past two decades in domains like CO_2 sequestration (Molins et al., 2014; Sell et al., 2013) and soil sciences (Khan et al., 2012). It is used to characterize and predict the evolution of porous materials under various petro-physical, geochemical and hydro(geo)logical conditions (Andra et al., 2013a,b; Hilpert and Miller, 2001; Saenger et al., 2011). This method was used to quantify the materials initial transport parameters and the amount of precipitate that formed during clogging experiments. A pore morphology model was used to estimate the effects of the precipitation front on the materials transport properties.

In addition, the precipitates were analyzed with SEM-EDX, to characterize their nature, shapes and sizes. Then, they were dissolved, to quantify the amount of precipitation. One and two

dimensions (1D and 2D) reactive transport models were build with CrunchFlow. They were calibrated on the experimental data obtained from the simple through diffusion of HTO prior to porosity clogging. Precipitation of celestite or calcite was introduced in the models, and the code applied Archie's law to calculate the response of porosity. The results of the models could be compared with the experimental data on several points - e.g., the HTO flux, the mass of precipitate, the position of the precipitation front and the minimum porosity reached in the precipitation front.

A slightly more complex system was studied in addition to the compacted sand: a compacted purified and Na-exchanged non swelling clay (illite from le Puy en Velay, called illite-du-Puy). The main difference with the sand was the dual porosity, characteristic of clays, where the anions are excluded from a part of the pore water due to high surface charges. To keep the system simple, a typical non-swelling clay was used, excluding the interlayer diffusion processes. The illite used was very well described in the literature. Its composition and physico-chemical properties were well known (Fialips and Robinet, 2011), as well as its initial transport parameters (Glaus et al., 2010, 2012). It was used in experiments very similar to the published works of Glaus et al. (2010). For this system, the standard double-reservoir and counter-diffusion methods were used. Celestite was precipitated in the pore space of two samples. One of these samples was impregnated with ^{14}C-MMA resin, cut in different places and exposed to an autoradiographic film. The porosity of the exposed surfaces was estimated following the method of Hellmuth and Siitari-Kauppi (1990) and Sammartino et al. (2002).

State of knowledge

The present work focused on the description of porosity clogging effects on molecular diffusion of radiotracers in pore water. The molecular diffusion is a well known phenomenon, however it is not fully understood when taking place in natural porous media, and especially in clays and clay-rocks. In such systems, the porosity is complex and may vary as a function of the (geo)chemical conditions.

Molecular diffusion in pore water

Diffusive solute transport, or volume diffusion, is the random motion of ions and dissolved species in a liquid, or of gaseous species in a gas. It occurs in response to temperature, pressure or concentration gradients. In porous media, two types of pore volume diffusion can be differentiated: (1) molecular diffusion and (2) Knudsen diffusion (Park et al., 1996). When the ratio of the pore radius to the mean free path of the diffusing species is big (≥ 10), molecular diffusion dominates the transport. Knudsen diffusion dominates when the ratio is small (≤ 0.1). The diffusive flux, F, through the unit cross-sectional area of a porous medium under steady state conditions can be described by Fick's first law (Boving and Grathwohl, 2001; Crank, 1975; Garrels et al., 1949):

$$F = -D_e \cdot \frac{dC}{dx} \tag{1}$$

where C is the concentration of the diffusing element, x is the space coordinate measured normal to the section, dC/dx represents the concentration gradient and D_e is the effective diffusion coefficient of the diffusing element. When the boundary conditions are constant (transient conditions), the diffusive flux is

described by Fick's second law:

$$\varepsilon \cdot \frac{\partial C}{\partial t} = D_e \cdot \frac{\partial^2 C}{\partial x^2} - \rho \cdot \frac{\partial C_s}{\partial t} \tag{2}$$

where ε is the porosity, ρ is the bulk dry density of the medium, C_s is the sorbed concentration of the diffusing species in the medium and $\partial C_s/\partial t$ is called the sink term and is due to the sorption of the species. In the case where the sorption is linear and can be described by a distribution coefficient $K_d = C_s/C$, at local equilibrium:

$$\frac{\partial C}{\partial t} = \frac{D_e}{\varepsilon + K_d \cdot \rho} \cdot \frac{\partial^2 C}{\partial x^2} = \frac{D_e}{\alpha} \cdot \frac{\partial^2 C}{\partial x^2} \tag{3}$$

where α is the rock capacity factor. In the cases where the diffusing species are conservative (no sorption), $K_d \cdot \rho = 0$ and therefore $\alpha = \varepsilon$.

The through diffusion of dissolved species is largely influenced by the porosity, as seen form eqs. 2 and 3, and by the geometry of the pore space. The geometry is often described by the geometric factor, G (Boving and Grathwohl, 2001), also called the tortuosity factor, τ_f^2 (Agbogun et al., 2013; Shackelford and Moore, 2013). This factor is the ratio of the constrictivity, δ to the tortuosity, τ^2. The constrictivity accounts for the steric hindrance when relatively large molecules pass through relatively small pores. It is only important if the size of the diffusing species is comparable to the size of the pores (nano- and sub-nanopores) (Boving and Grathwohl, 2001). The definition of tortuosity varies in the literature (Ghanbarian et al., 2013; Shackelford and Moore, 2013). In the majority of the cases, it is defined as the square of the ratio of the effective path length, l_e, to the length of the porous medium, l (see illustration fig. 1):

$$\tau^2 = \left(\frac{l_e}{l}\right)^2 \tag{4}$$

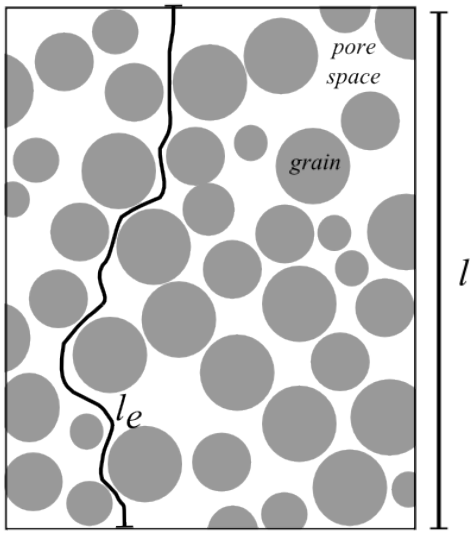

Figure 1: Schematic illustration of the tortuosity, where a tortuous path length, l_e, is compared to the porous material length, l.

When the pores are large compared to the diffusing species, the constrictivity equals 1 and therefore $G = 1/\tau_f^2 = 1/\tau^2$ (Boving and Grathwohl, 2001; Ghanbarian et al., 2013). The geometric factor is a parameter that cannot be measured experimentally. It can be calculated when the porosity and resistivity factor, R_f - equivalent to the diffusivity ratio, D' - is known. The relationship that allows this calculation is derived from Archie's law (Archie, 1942):

$$R_f = \frac{R_e}{R_w} = \varepsilon^{-m} \tag{5}$$

where R_e is the resistivity of the fluid in the pore space, R_w is the resistivity of the free fluid, and m is a fitting factor, often called cementation factor or exponent (Appelo et al., 2010). This relation is also known as the Bruggeman equation in soil sciences. When the diffusivity of the species is measured instead

of the resistivity of the fluid, Archie's law is written as (Boving and Grathwohl, 2001; Klinkenberg, 1951):

$$D' = \frac{D_e}{D_w} = \varepsilon^m \tag{6}$$

where D_e is the effective diffusion coefficient of the species in the pore solution and D_w is the diffusivity of the same species in pure water. When taking into account the geometric factor (Boving and Grathwohl, 2001):

$$D' = \frac{D_e}{D_w} = \varepsilon^m = \frac{\varepsilon}{G} \tag{7}$$

Eq. 7 was widely used in the literature to describe various porous materials (e.g., Garrels et al., 1949; Klinkenberg, 1951; Marshall, 1959; Millington, 1959; Reible and Shair, 1982). Its reliability is widely discussed, especially for complex porous materials (e.g., nano-porous catalysts, clays and clay rocks, heterogeneous materials like soils) (Boving and Grathwohl, 2001; Navarre-Sitchler et al., 2009). Often, a different version of the law had to be used in order to explain experimental results. For example (Currie, 1960; Shearer et al., 1965):

$$D' = \gamma \cdot \varepsilon^{\mu} \tag{8}$$

where γ is dependent on the porosity and μ is a measure of the pore space or accessible porosity and pore continuity ($\mu \leq m$). Other variations of the relationship imply the use of constants being multiplied and/or added to the porosity term (e.g., Dye and Dallavalle, 1958; Flegg, 1953; Rust et al., 1957). In most of the cases, the law was modified in order to fit the experimental data, when simply adapting the fitting factor m was not enough. More recently, Boving and Grathwohl (2001) and Navarre-Sitchler et al. (2009) suggested to use the accessible (or

effective) porosity, ε_a, rather than the total porosity. The accessible porosity is the portion of the porosity that is available for diffusion. If the saturation of the material is complete, there is no anion-exclusion due to charged water layers and there is no isolated pores, then $\varepsilon = \varepsilon_a$.

The cementation exponent in Archie's law formula can deviate strongly between different publications on the same systems, e.g., m = 2.0 (Shao et al., 2013) and m = 1.0 (Steefel and Lichtner, 1998) for the Maqarin natural analogue site. Gao et al. (2013) found that two groups of rocks belonging to the same sandstone formation could not be described with the same m. More complex systems - like clays and clay rocks - containing both nano- and microporosity could only be described in terms of a sum of two power laws (Tyagi et al., 2013). The later theoretical work demonstrated the important effects of nanopores on the overall transport parameters of clay systems.

Pore water in clays

In compacted clays, up to three types of water coexist (Appelo et al., 2010; Glaus et al., 2010; Montavon et al., 2009): (1) the free (mobile) water, which fills the micro and part of the nanopores, (2) a charged double layer, bound to the surface of the clay particles and (3) bond water between the layers of swelling clays, called the interlayer. These different types of water are illustrated in fig. 2. The charged double layer, or diffuse double layer, is an electrostatic water layer at the surface that balances the clays negative charge (Sposito, 2004). The most common swelling clays are smectites. Their interlayer may have different thicknesses (from 1 to 3 water layers), depending on the chemical conditions (pH, ionic strength) (Holmboe et al., 2012). The interlayer water is not accessible to anions due to their large sizes. The diffuse double layer is also not accessible to anions,

as it is positively charged. The free water, the most abundant type, is accessible to both cations and anions.

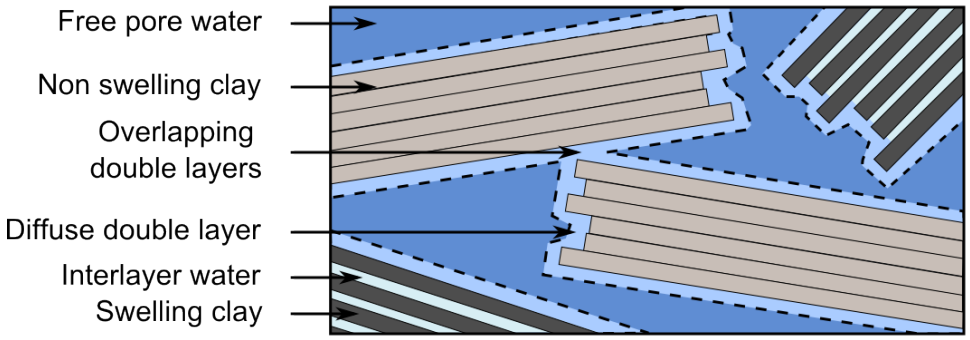

Figure 2: Schematic illustration of the different types of water found in compacted clays.

The combination of these three types of water creates a double porosity: the totality of the pore space is accessible to cations and neutral species, while anions can diffuse only in the free pore water (Montavon et al., 2009; Tournassat and Appelo, 2011). This is called the anion exclusion phenomenon. The paths available for anion diffusion are even more complex due to the overlapping of diffuse double layers (higher tortuosity). The cations diffusion is furthermore enhanced by the surface diffusion, a process by which the cations migrate in the diffuse double layer at the surface of the clays at a faster rate than in the free pore water (Glaus et al., 2012). A typical diffusion experiment in such systems will see the cations diffuse faster than expected, and the anions be delayed (Glaus et al., 2010, 2012; Van Laer et al., 2014).

The overall and anion accessible porosity of a compacted clay are dependent on the pore water (geo)chemistry and degree of compaction (Shackelford and Moore, 2013). At high ionic strength and/or high pH, the charged double layer is thicker, therefore decreasing the anion accessible porosity. In a similar

fashion, at high degrees of compaction the portion of free water is smaller than at low compaction, resulting in a smaller overall and anion accessible porosity. The charged double layers tend to superpose more, further decreasing the anion accessible porosity.

Reactive barriers and predictive modeling

Molecular diffusion in pores is the major migration process occurring in most of the engineered reactive barriers, e.g., CO_2 sequestration and long term geological disposal of high activity and long life radioactive wastes. The aim of the barriers is to limit - if not completely eliminate - the migration of contaminants towards the biosphere. The multi-barrier systems in the case of geological waste storage consist of the superposition of several barriers: the steel canisters containing the wastes are stored in concrete chambers, in some cases surrounded by a few meters of compacted bentonite. The whole is embedded in a deep and thick host rock with very low hydraulic conductivity (saline formation, granite, clay rock).

In such systems, the geochemistry of the concrete, bentonite and host rock are very different and vary with time and corrosion. The high contrasts between the different pore waters generate several complex processes that affect the contaminants migration, directly or indirectly (sorption, precipitation, dissolution...). The exact role of each different process and the quantification of their impact cannot be experimentally assessed, especially over the long periods (1,000 to 1,000,000 years) that are of interest in most safety assessment cases. Very often, reactive transport models are needed to interpret the experimental data and predict the long term evolution of reactive barriers. The models are calibrated on short term experiments (a few days to a few years), where the processes were studied separately. The reactive transport modeling is in itself a field in development, as

many different codes exist, that may give similar, complementary or different results, as different transport equations and scales (continuum or pore scale models) are taken into account. Some models focus more on the geochemistry, others on the hydraulics or the transport. All present serious limitations and are in constant improvement.

Structure of the manuscript

This manuscript is divided into two parts. Part I describes the materials and methods. In part II, the experimental and modeling results are described. Part I and Part II are made of four and three chapters, respectively, for a total of 7 chapters:

Chapter 1 describes the tools used to characterize the purified sea sand's composition and chemical properties (XRD, XRF, N_2-BET and sorption). The methods used to characterize the compacted sand - Mercury Intrusion Porosimetry (MIP) and μCT- are also described. An in-depth description of the illite-du-Puy is given as a literature review.

Chapter 2 explains the double-reservoir and counter-diffusion methods. The diffusion cells and experimental protocols used for each material are presented, as well as the linear regression method used to estimate the transport properties from HTO through diffusion data.

Chapter 3 relates the *post-mortem* analysis performed on the sand (selective dissolution and SEM-EDX of the precipitates) and illite (impregnation and autoradiography).

Chapter 4 describes the reactive and non reactive modeling procedures performed with CrunchFlow (1D and 2D models).

Chapter 5 concerns the full characterization of the sand's composition, physico-chemical properties and initial transport parameters, obtained from the combination of the methods described in chapters 1 and 2.

Chapter 6 presents the experimental results obtained for the clogging experiments in sand and illite, obtained from the combination of the methods described in chapters 2 and 3.

Chapter 7 presents the modeling results, and compares them to the experimental data.

The conclusions are presented together with expectations for future work on the topic. A published paper on the uptake of radionuclides during co-precipitation with celestite ($SrSO_4$) and strontianite ($SrCO_3$) is reported in appendix A. A complete sensitivity analysis of the model was performed, and the results are presented in appendix B.

Part I

Materials and methods

Chapter 1

Characterization of the porous materials

Two porous materials were used in the diffusion-controlled column experiments: commercially available purified sea sand (Merck product no. 1.07711.5000, average particle size 100 to 300 μm) and purified Na-exchanged illite (illite-du-Puy; Blanc et al. (2007b); Fialips and Robinet (2011); Glaus et al. (2012); Van Laer et al. (2014)). The purified sea sand was thoroughly analyzed. The illite is a material of well known properties, both in a powder and compacted state. A literature review describing the properties of the material is given.

1.1 Purified sea sand

The purified sea sand was characterized as a powder (surface properties, chemical and mineralogical composition) and as a compacted material (porosity, effective diffusivity, tortuosity...) by different methods. Before performing any analyzes and experiments, the sea sand was cleaned and prepared.

1.1.1 Cleaning procedure

A batch of sand was put in MilliQ water with a volume to mass ratio of 2:1. A small aliquot of 100 μL HNO_3 was added to the suspension (pH $\approx$ 3-4), which was then vigorously agitated for a few seconds. The turbid supernatant was poured out of the vessel a few seconds after agitation, giving enough time for the biggest particles to sediment and leaving the fines in suspension. This procedure was repeated 7-10 times until the supernatant appeared clear and a stable and a neutral pH was reached. The sand was then dried in an oven at 105°C for at least 24 hours.

Prior to setting up the diffusion experiments, aliquots of the clean and dry sand were resuspended in the same background electrolyte planned to be used in the experiments, and left to equilibrate for a minimum of three days. The background electrolyte used was spanning a concentration range between 1 and 500 mmol $\cdot$ L^{-1} NaCl.

1.1.2 Composition and chemical properties

The composition and chemical properties of the sand powder were characterized with several complementary methods: X-Ray diffraction (XRD), X-Ray fluorescence spectrometry (XRF), N_2-BET and batch sorption experiments.

Mineralogical and chemical composition

The sand's mineralogical composition was characterized by XRD. The analysis on the bulk powder and fines were performed on a Bruker D8 Advance equipped with a Cu-alpha radiation source and a Sol-X energy dispersive detector. The fines were extracted from the bulk powder during the cleaning procedure. During the first wash, a few drops of the supernatant were put on a sample holder, where they were left to dry at room temperature for a

few days before being analyzed.

The chemical composition of the raw and of the cleaned powder was obtained with XRF spectrometry, on a MagiXPRO, Fa. Philips, with a Rh anode at 3.6 kW. The trace elements were measured for undiluted powder pellets, and the major elements were diluted 14 times in melted glass pellets and measured at 3.2 kW.

Surface area

The nitrogen Brunauer-Emmett-Teller gas adsorption method (N_2-BET) was used to quantify the specific surface area of the raw and cleaned purified sea sand using a Quantachrome Autosorb 1 with a 5 points measurement. The sample was outgased at 150°C for 72 hours. In addition, N_2 adsorption and desorption isotherms were performed, to check for a possible micro-porosity within the grains.

Sorption of strontium

The strontium retardation by sorption could have an important impact on celestite precipitation in diffusion experiments. Such mechanisms should be taken into account in the interpretation of the results and models. Therefore, the strontium sorption on sand was measured in batch experiments. Aliquots of the sea sand powder were put in suspension in 20 mL 1-100 $\text{mol} \cdot \text{L}^{-1}$ NaCl background electrolyte solution spiked with $SrCl_2$ ranging from 1 to 100 $\mu\text{mol} \cdot \text{L}^{-1}$. In these conditions, a speciation model predicted that more than 99.9% of the strontium in solution is free Sr^{2+} ions. The solid/liquid ratio was varied (between 10 and 150), as well as the contact times and the pH of the solution. All experimental conditions are summarized in table 1.1. The suspensions were filtered with a 0.22 μm cut-off membrane filter (Millipore), and the equilibrated so-

lutions were analyzed with ICP-OES (PerkinElmer Optima 4300 DV).

Table 1.1: Summary of the initial experimental conditions for the sorption experiments of Sr^{2+} on purified sea sand.

Run	Contact time hours	S/L ratio g L^{-1}	[NaCl] mmol $\cdot$ L^{-1}	$[Sr]_{ini}$ mmol $\cdot$ L^{-1}	pH
1	36	10	1	0.001 to 1	5.5
2	24	25	1	0.05 to 0.1	5.5
3	24	50	1	0.05 to 0.1	5.5
4	24	100	1	0.05 to 0.1	5.5
5	24	150	100	0.05 to 0.1	5.5
6	24	100	100	0.05	2 to 11.2
7	24	100	1	0.05	2 to 11.2
8	24	50	1	0.05 to 0.09	10
9	24	100	1	0.05 to 0.09	10

1.1.3 The compacted material

Prior to the diffusion experiments, the porosity of the compacted material was characterized by Mercury Intrusion Porosimetry (MIP) and micro-tomography (μCT) imaging coupled to pore-morphology modeling.

Mercury Intrusion Porosimetry

The MIP was performed at Federal Institute of Material Research and Testing (BAM, Berlin, Germany) with an Autopore III (Micromeritics, USA) apparatus, following a modified approach after Minagawa et al. (2008). Two small cells were especially designed to fit in the MIP apparatus (fig. 1.1). These cells were composed of a glass tube of 10 mm length by 7 mm

inner diameter made in-house. They were closed on both ends by glued-on glass frits of 200 μm average pore diameter (ROBU glass filter, porosity 0, Hattert, Germany). The sand was compacted using the same method as for the diffusion cells (see section 2.1.2): one glass frit was glued to one end of the empty glass tube, and then the sand (kept in MilliQ water suspension) was scooped in the tube, which was firmly and repeatedly hit on the preparation table throughout the procedure. Once the tube was filled, it was left to dry at room temperature for one hour, and the second glass frit was glued on top of the sample. The samples were then dried in an oven at 105°C for 24 hours.

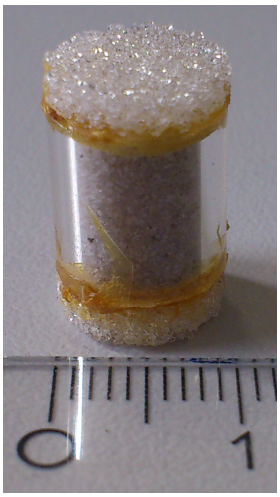

Figure 1.1: Glass cell filled with compacted purified sea sand used for MIP analysis.

Computed Tomography

The diffusion cells used for the experiments with purified sea sand are specifically designed for μCT measurements. They are made of Plexiglas, a material that has little X-rays absorption as compared to sand (Hubbell and Seltzer, 2004). The cells are cylindrical with rotational symmetry, portable, and their position is adjustable as their reservoirs are inclusive and not

linked with tubing and pumps (fig. 1.2). Their dimensions are thought to be large enough to provide a representative volume of the porous material for the diffusive transport conditions, and still small enough to obtain a good resolution with μCT and to perform the diffusion experiments within reasonable time-frames (1-2 months).

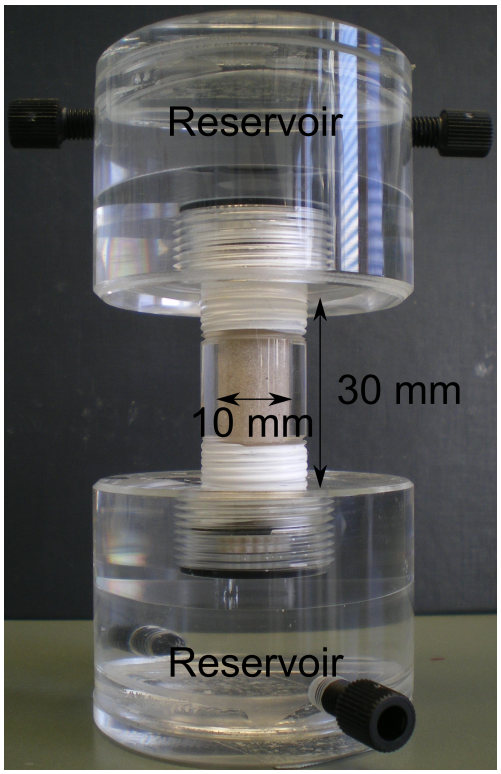

Figure 1.2: Photograph of a diffusion cell used for the sand material.

The measurements were performed on a CT-alpha 160 X-ray device (Procon, Germany) at 100 keV X-ray energy and 125 μA tube current, with a 1 mm Al-filter on diamond-coated target, with 10 times 2 second exposure time on a Hamamatsu flat panel detector. The cells were placed at a distance from the source that allowed the measurement of the central 30 mm of the 50 mm long columns, with a resolution in the order of 15 μm. A high resolution measurement (5.89 μm) was also performed on

one sample. The samples were placed vertically on the rotating plate, resting on either their low concentration reservoir (diffusion experiments without clogging) or SO_4-reservoir (diffusion experiments with porosity clogging). The measurements were made for 800 angles of rotation. The approach used to treat the μCT data and characterize the porous material is summarized in fig. 1.3.

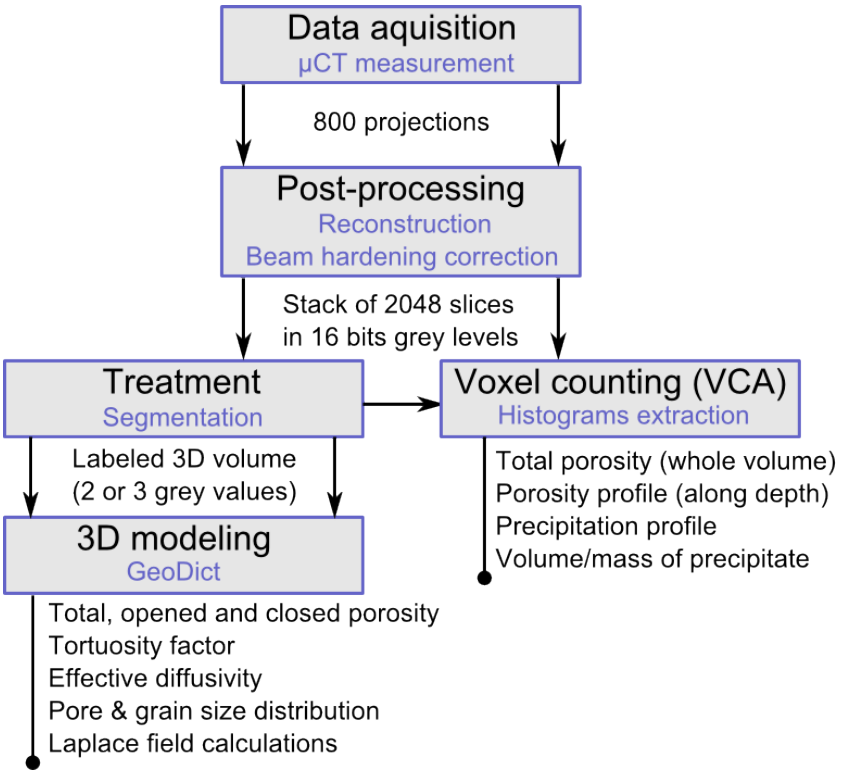

Figure 1.3: Treatment procedures used for the data acquired through μCT and approach used to characterize the porous materials from the treated data sets.

The volumes were reconstructed from the 800 projections with Octopus (Inside Matters, Ghent, Belgium). The reconstructions produced 2048 images, or slices, of 2048×2048 pixels resolution and perpendicular to the direction of diffusion. The slices were directely treated for beam hardening correction with Octopus. The stacks of images were then treated as 3D volumes

with the image treatment software Avizo (FEI Visualization Sciences Group, Bordeaux, France). For some of the volumes measured, a non-local mean filter was applied to homogenize the gray levels of the images and soften the edges (Buades et al., 2005). The volumes were then segmented, meaning that the constituting elements (e.g., the sand grains, the pore space, the precipitated secondary phase) were differentiated and labeled. The segmentation process was based on the gray levels of the images. The user defined a threshold within the histogram of the images that corresponded to one element (e.g., the sand grains), and the rest of the gray values were assigned to the other element (e.g., the pore space). This process could be done either in 16 bits (65536 gray values) or 8 bits (256 gray values). The segmentation process for the diffusion cells without porosity clogging resulted in a 2-color 3D volume, with one value assigned to the sand grains, and the other to the pore space. When the diffusion cells contained a secondary phase (celestite), that phase was either segmented separately from the two other materials to characterize the precipitate itself, or together with the sand grains to characterize the changes in porosity.

The segmented volumes were implemented in a commercially available pore-morphology model, GeoDICT (Math2Market, Kaiserslautern, Germany). This model allows the estimation of the average porosity (total, open and closed), pore and grain size distributions, effective diffusivity and tortuosity, amongst other properties, of the implemented volumes in the 3 Cartesian directions. For the porosity estimation, the model interprets neighbor voxels as belonging to the same connected group if they are in contact by either their face, or edge or vertex. Isolated connected groups of the voxels with the pore value are seen as isolated pores. The effective diffusivity was calculated with a bulk (Laplace) diffusion approach. It is a continuum mechanics approach, with a Laplace equation in pores with Neumann

boundary conditions at the pore-surface interface. The tortuosity factor was calculated as the ratio of the porosity to the effective diffusivity (eq. 7). The geometrical pore and grain size distributions were calculated by fitting spheres of increasing radius in the pores. The centers of the spheres were placed in the center of the pores, and their radius increased with a step size of 1 voxel length, until the spheres reached the surface of the sand and celestite grains. The final radius of the spheres corresponds to the radius of the pores or grains (Wiegmann et al., 2013).

1.2 Illite-du-Puy

Illite is a non-swelling phyllosilicate of the dioctahedral 2:1 type, or TOT (Fialips and Robinet, 2011). The O-sheet is essentially aluminous with Fe^{2+}/Fe^{3+} and Mg^{2+} substitutions, and the T-sheet is essentially siliceous with Fe^{3+} and Al^{3+} substitutions. The permanent negative charge of the layers, ranging generally between 0.8 and 0.9 per half cell (4T+3O sites), is due to substitutions of Al^{3+} by divalent cations (Fe^{2+} and Mg^{2+}) in O-sites. This charge is compensated by cations, mostly K^+, on the surface and interlayer spaces. As the permanent negative charge is high, the ionic bounds with the K+ are strong. These strong bounds keep the layers close together, preventing water from entering in the interlayer space. The clay particles are thus non-swelling (Fialips and Robinet, 2011).

The clay material used in the present study was the illite-du-Puy, a natural clay extracted from the Puy-en-Vellay (Massif Central, France) Upper Eocene clay formation. The material contains up to 40% of carbonates and quartz, with a clay fraction composed primarily of illite (80-100%) (Fialips and Robinet, 2011). The illite-du-Puy used in this study was purified (removal of quartz and carbonaceous phases) and Na-exchanged in a standardized way, described in details by Glaus et al. (2012). The

purification method consists of an acid treatment using buffered formic acid during which calcite is removed and the illite exchangeable ions are replaced by Na^+. The illite-du-Puy was provided by PSI, Switzerland. The sample powder contained the < 63 μm size fraction, which was obtained through crushing and sieving of the rock pieces (Poinssot et al., 1999). For the acid treatment, the received illite sample was equilibrated in formate buffer solution (0.05 mol $\cdot$ L^{-1} formic acid and 0.05 mol $\cdot$ L^{-1} Na-formate in 1 mol $\cdot$ L^{-1} NaCl, pH $\approx$ 3.5) at a mass to volume ration (m:V) of 100g:1L for 4 hours by gentle magnetic stirring. The solid phase was separated by centrifugation (500 g for 5 minutes), re-suspended in 1 mol $\cdot$ L^{-1} NaCl and equilibrated overnight (also by gentle magnetic stirring). This washing procedure was applied three times. After removing 80 to 85% of the liquid phase, the settled suspension was transferred in dialysis bags and dialysed against MilliQ water in a volume ratio of 1:5 to 1:10 (internal volume: external volume). The volume of the internal solutions increased during dialysis due to swelling effects. The external solution was replaced twice every 24 h, until no NaCl was detectable in the external solution (checked by adding $AgNO_3$). In the last step, the clay suspensions were freeze dried. The characterization of the transport properties were carried out with this material in standardized diffusion experiments.

1.2.1 Generalities about illite-du-Puy

XRD patterns of the purified and Na-exchanged material agreed with the presence of 2/1 type clay minerals (80-90%), K-feldspar (5-12%) and micas (1-5%) (Blanc et al., 2007a; Fialips and Robinet, 2011). XRD was also performed on oriented preparations (<2 μm fraction). The mineralogical quantification of the clay fraction led to the detection of well crystallized illite (70-80%)

and an illite/smectite (I/S) mixed layer (20-30%) (Blanc et al., 2007b). The I/S mixed layer has a low proportion of smectite (80/20) and low ordering (R=1). Grain density measurements, repeated 5 times, yielded a mean value of 2.789 ± 0.001 g·cm^{-3} (Fialips and Robinet, 2011).

Fialips and Robinet (2011) published an in-depth review of the known physico-chemical propertied of the illite-du-Puy. They found an average specific surface area of 110.5-132.1 m^2·g^{-1} and a total CEC of 189-191 meq·Kg^{-1} determined by the Cohex method. The formula of the Na-exchanged illite-du-Puy half-cell is:

$$K_{0.64}Na_{0.12}Ca_{0.04}(Al_{1.17}Fe_{0.49}Mg_{0.33})[Si_{3.52}Al_{0.48}]O_{10}(OH)_2$$

1.2.2 Transport properties of the compacted material

Glaus et al. (2012) performed several diffusion experiments with HTO and ^{85}Sr in illite-du-Puy pellets compacted to a bulk-dry density of 1700 kg·m^{-3} (estimated porosity of 0.39). In experimental conditions similar to the present study (pH ≈ 5.5, ionic strength ≈ 0.5 mol · L^{-1}, ambient air and room temperature), they obtained an effective diffusion coefficient of (2.1 ± 0.2)×10^{-10} $m^2 \cdot s^{-1}$ for HTO, and an accessible porosity of 0.60 ± 0.21 from a 1D modeling fit. The effective diffusivity of ^{85}Sr in the same clay pellet was found equal to 1.6 ×10^{-10} $m^2 \cdot s^{-1}$, and the accessible porosity to 0.42. The fast diffusion of the ^{85}Sr was attributed to surface-diffusion phenomenon, where the cations have an enhanced mobility on the negatively charged surface of the clay particles constituting the porous material (Oscarson, 1994; Gimmi and Kosakowski, 2011).

Similar experiments, performed by Van Laer et al. (2014) in illite-du-Puy pellets compacted to a bulk-dry density of 1700 kg·m^{-3}, gave an HTO effective diffusivity of (1.8 ± 0.3)×10^{-10} $m^2 \cdot$

s^{-1}, in good agreement with the results of Glaus et al. (2012), and an accessible porosity of 0.42 ± 0.11. These values were obtained by fitting the experimental data with 1D transport models.

These experimental procedures were reproduced by a co-worker of the author (unpublished work), and the results were fitted with a 3D model (COMSOL) taking into account the real geometry of the pierced filter supports. The HTO effective diffusivity was $(1.97 \pm 0.05)\times10^{-10}\ m^2 \cdot s^{-1}$ and the ^{36}Cl effective diffusivity was $(1.00 \pm 0.05)\times10^{-10}\ m^2 \cdot s^{-1}$ for a total accessible porosity of 0.43 ± 0.09 and an anion accessible porosity of 0.25 ± 0.08. These values are compared to the published values in table 1.2.

Table 1.2: Values of effective diffusivity (D_e, in $\times10^{-10}\ m^2 \cdot s^{-1}$) and accessible porosity (ε_a) for various tracers found in the literature for the 1700 kg·m^{-3} compacted Illite at 0.5 mol $\cdot$ L^{-1} NaCl and pH ≈ 5.5.

Tracer	ε_a	D_e	Source
HTO	0.60 ± 0.21	2.1 ± 0.2	Glaus et al. (2012)
	0.42 ± 0.11	1.8 ± 0.3	Van Laer et al. (2014)
	0.43 ± 0.09	1.97 ± 0.05	unpublished work
^{85}Sr	0.42	1.6	Glaus et al. (2012)
^{36}Cl	0.25 ± 0.08	1.00 ± 0.05	unpublished work

Chapter 2

Diffusion experiments

The non-steady state through diffusion method, also called time-lag or transient method, was used to measure the effective diffusivity (D_e) and porosity (ε) of the materials (Barrer, 1953; Boving and Grathwohl, 2001; VanLoon et al., 2003a). This method also allows the continuous measurement of the two parameters during porosity clogging by precipitation.

The experimental set-ups used for diffusion in sand and illite differed slightly, as the two materials have very different properties. The diffusion cells used were optimized for the different materials used. However, the protocols for through diffusion prior to and during porosity clogging were very similar.

2.1 Diffusion and porosity clogging in sand

An extensive characterization of the compacted sea sand initial properties (prior to porosity clogging) was performed with conservative tracer through-diffusion experiments. The transport properties of the sand were determined on 10 different samples, in up to 4 duplicates, and in 2 different ionic strengths (1 and 500 mmol $\cdot$ L^{-1} NaCl). Once the properties were well characterized, precipitation experiments in diffusion-controlled conditions were performed by counter-diffusion of Sr^{2+} and SO_4^{2-} (precip-

itation of celestite) or Ca^{2+} and CO_3^{2-} (precipitation of calcite), following the method of Prieto et al. (1997, 2002) with other porous matrix material.

2.1.1 The diffusion cells

As discussed previously, the diffusion cells used for the sand were especially designed to be suitable for computed tomography measurements. Their dimensions were chosen to allow good resolution with μCT and to perform diffusion experiments within reasonable time-frames (1-2 months). They are built of 50 mm long and 10 mm inner diameter cylinders (or column) with a 5 mm wall thickness filled with the porous material, and of two 20 mL capacitance reservoirs screwed at each end of the cylinder (fig. 2.1). A few of the results that are presented in section 5.2.2 were obtained with 1.5 mL reservoirs.

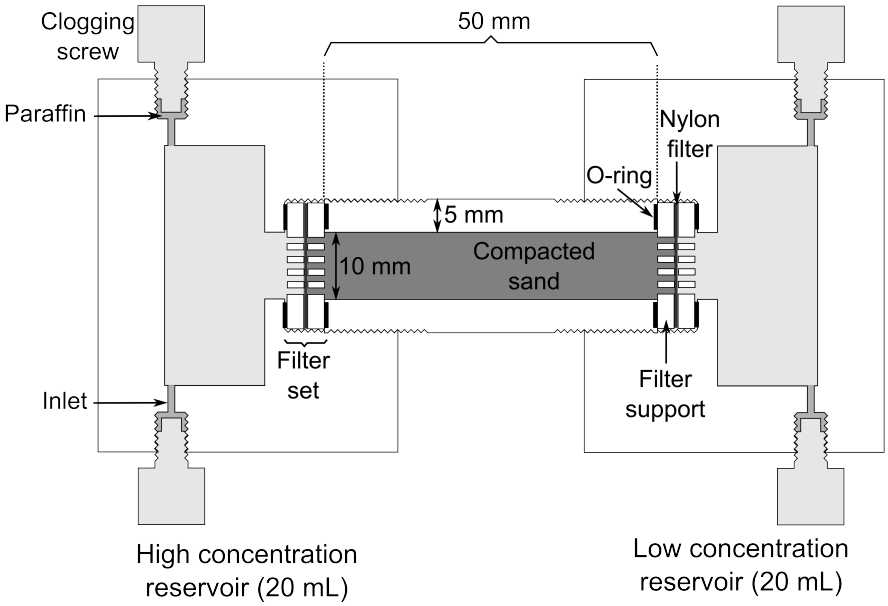

Figure 2.1: Schematic representation of a typical cell used for the diffusion experiments with purified sea sand.

The column and reservoirs are separated by a filter set, composed of a 18 μm nylon gaze (Millipore) placed between two filter supports. The filter supports were 2 to 3 mm thick disks of Plexiglas pierced by 37 holes of 1 mm diameter in their center (fig. 2.2). These filter supports had a porosity of 0.37, very similar to that of the compacted sand, and a tortuosity of 1 (straight cylindrical pores). Two inlets were drilled in each reservoir, for the sampling and renewing of the solutions within.

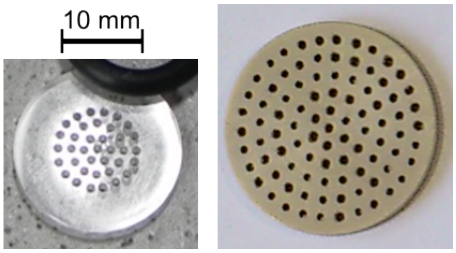

Figure 2.2: Photos of the pierced filter supports used in the sea sand (left) and illite-du-Puy (right) diffusion cells. The holes are straight cylinders of about 1 mm diameter.

To prevent any leaks possibly leading to pressure gradients in the cells, many precautions were taken. The screws of the column were covered with Teflon band prior to the coupling with the reservoirs. In addition, the inlets and remaining space between reservoirs and column screws were clogged with paraffin. In order to prevent density driven flows, the cells were kept perfectly horizontal on a leveled metallic plate.

2.1.2 Filling the columns with the porous material

The filling procedure was designed to be reproducible in terms of compaction, and to obtain a homogeneous porous material free of air bubbles. First of all, one reservoir was filled with the background electrolyte. Then, one filter set was mounted and the empty, dried and clean column was screwed on top of it. A

small aliquot of the background electrolyte was poured into the column up to the third of its height. The equilibrated sand still in its suspension was slowly scooped into the column, allowing the sand to gently and homogeneously settle, up to the top of the column. The excess of solution was removed as the sand column formed. Throughout the whole procedure, the cell was firmly and repeatedly hit on the preparation table in order to compact the sand. Once the column was filled, the second filter set was mounted on top of it. The remaining reservoir, still empty, was screwed and then filled with the same background electrolyte solution.

2.1.3 Characterization of the initial properties

The initial properties of the compacted sand (porosity, diffusivity and tortuosity) were determined by through diffusion of a conservative tracer, here tritiated water (HTO). This method is relatively simple to setup and gives reliable results, although such experiments have to be conducted over relatively long periods (up to 2 months).

The background electrolyte composition and concentration were constant throughout the whole system: the pores and both reservoirs were filled with the same background solution. Tracings were performed in 1 $mmol \cdot L^{-1}$ and 0.5 $mol \cdot L^{-1}$ NaCl. One of the reservoir - called the high concentration reservoir - was spiked with the conservative tracer at around 4.5 $kBq \cdot mL^{-1}$- (4×10^{-9} $mol \cdot L^{-1}$) or around 8.5 $kBq \cdot mL^{-1}$ (8×10^{-9} $mol \cdot L^{-1}$). The amount of tracer measured in the opposite reservoir - the low concentration reservoir - was used to determine the initial parameters of the material as described later in section 2.3. The boundary conditions were kept constant by regularly renewing the solutions in the reservoirs (twice a week). This ensured that the amount of tracer in the low concentration reservoir did not

exceed 1% of the amount in the high concentration reservoir, and the variation in activity in the high concentration reservoir did not exceed 5%, as recommended by VanLoon et al. (2003a). Experimental conditions are reported in table 2.1.

Table 2.1: Summary of the experimental conditions for the HTO through diffusion experiments performed to characterize the initial properties of the compacted sea sand.

Cell ID	Run	[HTO] $kBq \cdot mL^{-1}$	$[NaCl]_{background}$ $mmol \cdot L^{-1}$
S1	HTO1	4.81	1
S1	HTO2	5.00	1
S1	HTO3	4.39	500
S2	HTO1	4.78	1
S2	HTO2	4.75	1
S2	HTO3	9.50	1
S2	HTO4	4.39	500
S3	HTO1	4.39	500
S3	HTO2	9.35	500
S4	HTO1	8.45	500
S5	HTO1	8.43	500
S6	HTO1	8.44	500
S7	HTO1	8.45	500
S8	HTO1	9.36	500
S9	HTO1	8.41	500
S10	HTO1	8.39	500

2.1.4 Clogging of the pore space

The counter-diffusion protocol used for the precipitation of secondary phases in the compacted sand pore space was similar to the simple through diffusion experiment described previously. One of the two reservoirs contained the cation of the mineral

to be precipitated (**Sr**Cl_2 for celestite or **Ca**Cl_2 for calcite) and the other reservoir contained the anion (Na_2**S**O_4 for celestite and Na_2**C**O_3 for calcite). The cation and anions were present in equal concentrations. These concentrations were varied between 0.01 and 0.50 $mol \cdot L^{-1}$. The NaCl background electrolyte initially saturating the porous material had either the same concentration or the same ionic strength as the solutions in the reservoirs. For some of the celestite precipitation (runs CEL) and all of the calcite precipitation (runs CAL) cells, the reservoirs were spiked with H_4SiO_4 in a concentration corresponding to equilibrium with quartz (1.74×10^{-4} $mol \cdot L^{-1}$), in order to have similar conditions as in the pore space. The cation reservoirs were spiked with HTO (2 to 8.4 $kBq \cdot mL^{-1}$) or a cocktail of HTO (2 $kBq \cdot mL^{-1}$), ^{36}Cl (2 or 1 $kBq \cdot mL^{-1}$) and ^{85}Sr (0.2 $kBq \cdot mL^{-1}$). All initial conditions are reported in tables 2.2 and 2.3. The experiments noted with a "°" were performed on new samples which were not used previously for HTO through diffusion experiments.

Table 2.2: Summary of the experimental conditions for the through diffusion experiments performed in sea sand for porosity clogging by precipitation of celestite ($SrSO_4$).

Cell ID	Run	Tracers, in $kBq \cdot mL^{-1}$			$[NaCl]_{background}$	$[Sr^{2+}]$ & $[SO_4^{2-}]$
		HTO	^{36}Cl	^{85}Sr	$mmol \cdot L^{-1}$	$mmol \cdot L^{-1}$
S4	CEL	1.96	1.96	0.23	30 [a]	10
S5	CEL	1.98	1.08	0.22	150 [a]	50
S6	CEL	1.91	0.99	0.22	300 [a]	100
S7	CEL	1.94	0.98	0.22	750 [a]	250
S3	CEL	9.35	-	-	500	500
S13	CEL°	4.21	-	-	500	500
S14	CEL°	4.24	-	-	500 [b]	500

[a] Si^{4+} added to the reservoirs.

[b] KI was used as background in the pore space instead of NaCl.

Table 2.3: Summary of the experimental conditions for the through diffusion experiments performed in sea sand for porosity clogging by precipitation of calcite ($CaCO_3$).

Cell ID	Run	Tracers, in $kBq \cdot mL^{-1}$ HTO	^{36}Cl	$[NaCl]_{background}$ $mmol \cdot L^{-1}$	$[Ca^{2+}]$ & $[CO_3^{2-}]$ $mmol \cdot L^{-1}$
S1	CAL	2.12	0.82	30	10
S2	CAL	2.21	-	150	50
S9	CAL	2.21	-	300	100
S10	CAL	2.17	-	750	250
S8	CAL°	8.43	-	500	500

The activities of the tracers in the cation and anion reservoirs were measured with Liquid Scintillation Counting for all three tracers (PerkinElmer Tri-Carb 3110 TR).

2.2 Diffusion and porosity clogging in clay

For the illite-du-Puy system, no simple tracing experiments were performed prior to the clogging experiments, as such studies were already performed by other authors in similar experimental conditions (Glaus et al. (2010, 2012) and a coworker, unpublished work). The counter-diffusion protocol was also used for the precipitation of celestite within the pore space, in conditions comparable to the experiments performed on the sea sand. The clogging experiments were performed on two identically prepared samples.

2.2.1 The diffusion cells

The diffusion cells used for the illite-du-Puy were made of PEEK and had a smaller thickness than for the sand. The system was similar: a cylinder of 25 mm inner diameter and 33 mm length held the 10 mm thick compacted clay pellet, and two end

pieces were fixed at each opening of the column (fig. 2.3). The material and end pieces were separated by a 22 μm membrane filter placed on supporting plates. The filter supports were 25 mm diameter and 2 mm thick PEEK plates pierced with 91 holes of 1 mm diameter (porosity of 0.15 and tortuosity of 1, fig. 2.2). In this set up, the end pieces were not reservoirs. They had one inlet and one outlet connected by an inclusive weaving channel, so that the solution circulating in the channel was in direct contact with a maximum of the filter supports surface.

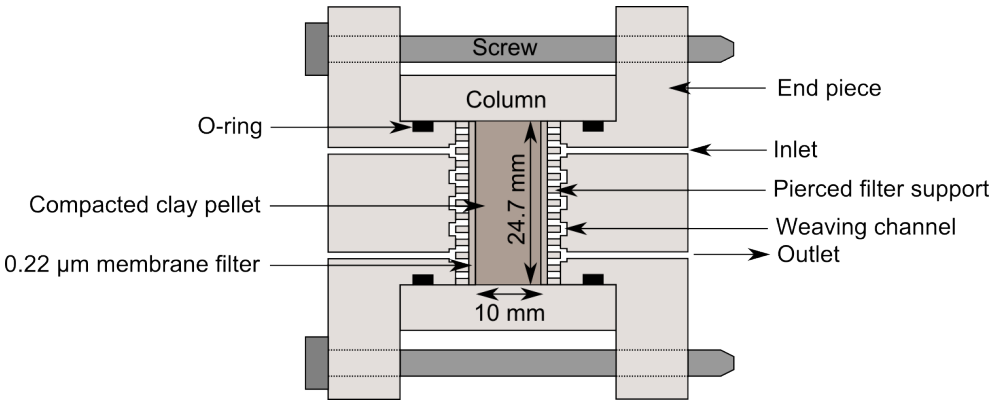

Figure 2.3: Schematic representation of a typical cell used for the diffusion experiments in compacted illite-du-Puy (longitudinal section).

2.2.2 Preparation of the porous material

The purified and Na-exchanged illite powder provided by the CatClay project (Fialips and Robinet, 2011) was pressed into pellets of 10 mm thickness and 24.7 mm diameter. Approximately 8.6 g of the powder was placed in a half-open diffusion cell and compressed to a bulk dry density approaching 1700 kg·m^3, resulting in a porosity of 0.40 for a water content of 2%. The cell was then closed by the remaining end piece, and the background electrolyte solution was circulated through one of the end pieces with the help of a peristaltic pump, while the in-

let and outlet of the other end were left open to let the air escape. This method allowed the full saturation of the clay with solution by capillary suction. After a saturation period of at least 2 days, the second end piece was connected to the background electrolyte reservoir and the system was left to equilibrate for an additional day.

2.2.3 Clogging of the pore space

For the clogging of the porosity by precipitation of celestite, two samples were prepared (IdP1 and IdP2). The experimental set-up is schematically presented in fig. 2.4. One of the reservoirs was filled with 0.5 mol $\cdot$ L^{-1} $SrCl_2$, and the other with 0.5 mol $\cdot$ L^{-1} Na_2SO_4. The pore space was initially filled with a 0.5 mol $\cdot$ L^{-1} NaCl solution, in the same concentration as the solutions in the reservoirs. The cation bearing solution was spiked with HTO and ^{36}Cl as the conservative tracers, in equal concentrations (2000 Bq $\cdot$ mL^{-1}).

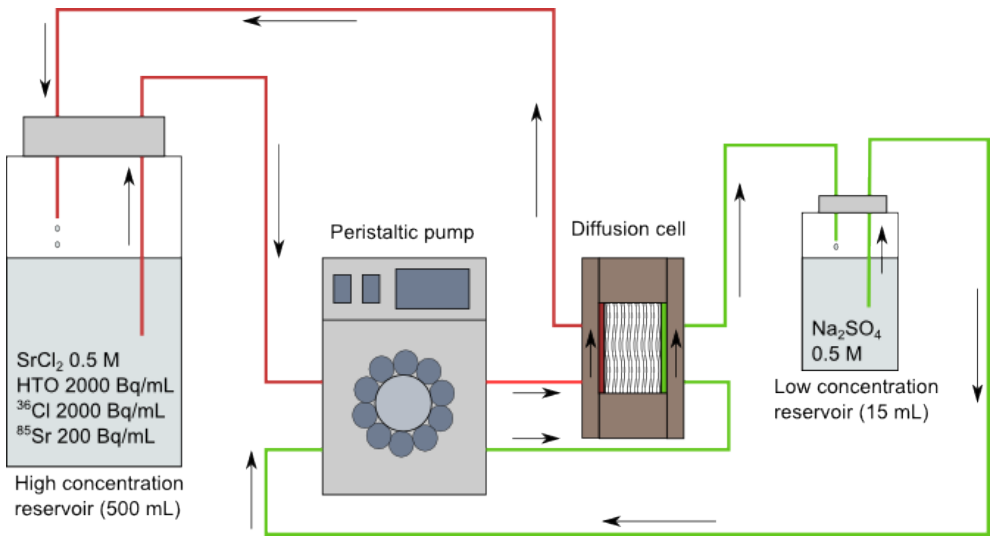

Figure 2.4: Experimental protocol used for the diffusion experiments in compacted illite-du-Puy with porosity clogging by celestite precipitation. Modified from VanLoon et al. (2003a).

The Sr-reservoir of one of the two cells (IdP1) was also spiked with ^{85}Sr (200 $Bq \cdot mL^{-1}$) as a reactive tracer. The Sr-reservoirs were 500 mL bottles and were not renewed during the duration of the experiments, as the large volumes ensured that the system was kept within the ideal conditions for constant boundary conditions (concentration variation of less than 5%). The samples were regularly taken directly from the reservoir. As the volumes required for analyzes were small (1 to 2 mL), the variation in the volume was not significant. The SO_4-reservoir was a 15 mL flask and was renewed every day until the flux of tracers significantly decreased, and then only once a week for the remaining time. A peristaltic pump circulated the solutions at a constant and slow flow rate (50 $\mu L \cdot min^{-1}$) through each end pieces.

2.3 Analytical treatment of the diffusion data

The method used to calculate the effective diffusivity and porosity of the porous materials from through diffusion data obtained in transient conditions was that described in details by VanLoon et al. (2003b,a). This method will be briefly described thereafter. First, the total amount of tracer diffused from the high to the low concentration reservoir, called the cumulative activity, was calculated. Then, the resulting data were plotted against the time, and the effective diffusivity (D_e) and porosity (ε) were given by the slope and intercept of the linear regression of the last points of the diffusion curve (steady state part of the flux), respectively.

2.3.1 The cumulative activity

The total amount of tracer diffused through the porous material, Q_{tracer}, is the sum of the activity measured in the low concentration reservoir at each sampling and renewal, A_{tracer}. When only

HTO was present, its activity was measured in cpm (counts per minute) with LSC. The background, C_{bkg}, was subtracted from the net count rate, C_{net}, to obtain the count rate of the tracer in the sample, C_{HTO}:

$$C_{HTO} = C_{net} - C_{bkg} \tag{2.1}$$

When cocktails of tracers were used in the experiments (HTO, ^{36}Cl and/or ^{85}Sr), the method to differentiate the count-rates of each different tracer from the LSC emission spectra was slightly more complex, as the LSC technique measured the emissions of the 3 tracers. The emission spectra was bimodal with a clear separation of the 2 peaks around 20 KeV. The first peak (0 to 20 KeV) corresponded to the combined emissions of HTO, ^{36}Cl and ^{85}Sr, and the individual count-rates of the 3 tracers could not be differentiated. The second peak (20 to 2000 KeV) corresponded to the emission of ^{36}Cl only.

The concentration of ^{85}Sr in the samples was directly measured with gamma-spectroscopy (in $\mathrm{Bq} \cdot \mathrm{mL}^{-1}$), as it was the only tracer with gamma emissions. The $C_{^{85}Sr}$ was accounted for in the first peak of the LSC emission spectra. It could be back-calculated from the ^{85}Sr concentration measured with gamma spectroscopy, knowing the efficiency of the LSC method for ^{85}Sr in the 0-20 KeV window. The $C_{^{36}Cl}$ was calculated from the 20 to 2000 KeV window, and the ^{36}Cl in the 0-20 KeV window was back-calculated. Finally, the C_{HTO} could be calculated as follows:

$$C_{HTO} = C_{net} - (C_{bkg} + C_{^{36}Cl} + C_{^{85}Sr}) \tag{2.2}$$

These diffused activities were converted from cpm to Bq. For the conversion, one had to take into account the counting efficiency of the LSC device, f, in each energy window. It was measured on standard solutions of the tracers in different concentrations and sample volumes, before and after every batch

of samples. To give an example, it was approximately 0.30 for HTO in the 0-20 KeV window, meaning that the counting recovered approximately 30% of HTO activity in the sample. The conversion was made as follows:

$$A_{tracer} = \frac{C_{tracer}}{60 \cdot f_{tracer}^{window}} \tag{2.3}$$

Finally, the cumulative activity was calculated as:

$$Q_{tracer} = \sum_{i=1}^{n} A_{tracer(i)} \tag{2.4}$$

2.3.2 The linear regression

The linear regression of the diffusion curve ($Q_{tracer} = f(time)$) must be calculated on the last data points of the curve, when the flux of diffused material becomes constant. The flux, F (in $\mathrm{Bq} \cdot \mathrm{m}^{-2} \cdot \mathrm{s}^{-1}$), is calculated as the ratio of activity in the low concentration reservoir, A_{tracer}, at a time t to the surface of the cross section of material normal to the diffusion direction, S, over the time of contact ($\Delta t = t_{i-1} - t_i$):

$$F = \frac{A_{tracer}}{S \cdot \Delta t} \tag{2.5}$$

An example of a typical diffusion and flux curves is illustrated in fig. 2.5. On this example, the linear regression was made on the last points of the diffusion curve, when the flux is constant.

The formula of the linear regression is expressed as follows:

$$Q_{tracer} = a + b \cdot t \tag{2.6}$$

The porosity (ε) can be calculated from the intercept (a):

$$a = -\frac{S \cdot L \cdot C_0 \cdot \varepsilon}{6} \tag{2.7}$$

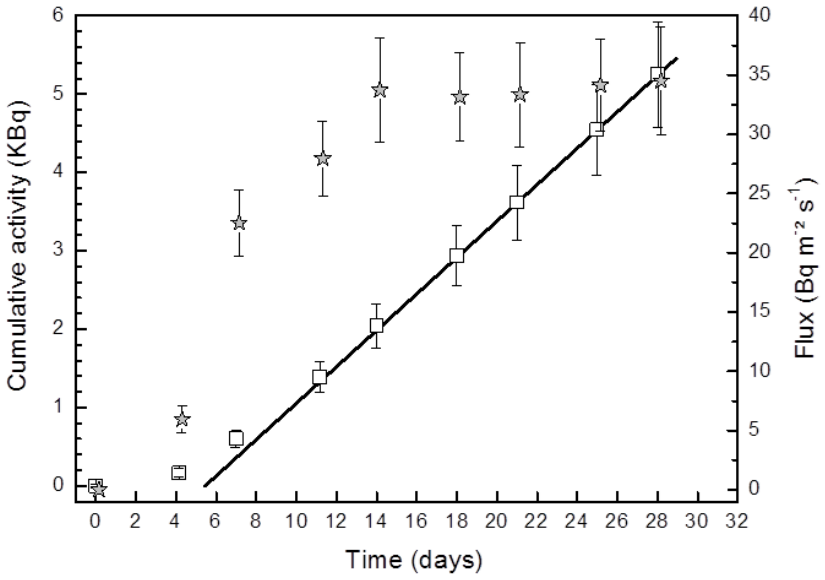

Figure 2.5: Typical diffusion (squares) and flux (stars) curves, with an example of linear regression (straight line) on the last points of the diffusion curve (at constant flux).

Where L is the length of the porous material, in m, and C_0 is the activity in the high concentration reservoir, in $\mathrm{Bq} \cdot \mathrm{m}^{-3}$. The effective diffusivity (D_e) can be derived from the slope of the line (b):

$$b = \frac{S \cdot C_0 \cdot D_e}{L} \tag{2.8}$$

In addition, the geometric factor (G) of the material was calculated as follows:

$$G = \frac{D_w}{D_e \cdot \varepsilon} \tag{2.9}$$

As discussed in the introduction, the geometric factor is the ratio of the tortuosity to the constrictivity. In the case of a simple porous material with relatively large pores like poorly compacted sea sand, the constrictivity for all dissolves species

can be assumed to be 1 (Boving and Grathwohl, 2001). Therefore, one can assume that the tortuosity is approximately equal to the geometric factor in the present case.

Chapter 3

Post-mortem analysis

The *post-mortem* treatment differed with the porous material. The precipitates formed in the sand during clogging experiments were characterized with SEM-EDX, and their mass was estimated from selective acidic dissolution treatment. For one of the two clay samples, the material was impregnated directly in the diffusion cell with a ^{14}C labeled MethylMethAcrylate (^{14}C-MMA) resin and the connected porosity was measured with autoradiography.

3.1 Characterization of the precipitates in the sand system

The reacted sand was simply pushed out of the diffusion cells, separated into small samples, cleaned and analyzed. One small solid sample from the precipitation front was analyzed with SEM-EDX in order to characterize the shape, size and composition of the clogging phase. The rest of the samples were dissolved with a celestite selective acid treatment, in order to estimate the mass of precipitate.

3.1.1 Sampling of the porous material

The reservoirs of the diffusion cells were removed, and the sand was pushed out of the columns with a piston. The compacted sand kept its cylindrical shape once out of the column, allowing to easily cut out samples every 5 mm. Each column provided 10 samples of about 0.5 g of material. The solid samples were rinsed with MilliQ water in a vacuum filter. Large volumes of cleaning solution were used as compared to the volume of the pore solution (about 10 mL of MilliQ water for an estimated 0.2 mL of pore solution) to ensure the complete removal of the pore solution. The contact time between the samples and the cleaning solution were very small (a few seconds) to avoid dissolving the precipitate. The samples were then dried in an oven at 105°C for 24 hours. A few mg of the solid samples containing the precipitation front were sampled for SEM-EDX analysis (FEI Quanta 650 FEG). The remaining solid samples were put separately in suspension in hot acidic solutions for several hours in order to reach complete dissolution of the secondary phase, as described thereafter.

3.1.2 Quantification of the precipitation

The dissolution protocol used for the celestite was adapted from the study on dissolution kinetics of celestite by Aydogan et al. (2006) (see appendix C for details on the procedure). The solid samples were put in suspension in 100 mL of 0.5 $\text{mol} \cdot \text{L}^{-1}$ HCL (pH $\approx$ 2), and stirred at 500 rpm and 70°C for 6 hours. The suspensions were then filtered with a vacuum filter set equipped with 0.22 μm membrane filters, and 2 aliquots of each equilibrated acidic solutions were analyzed by ICP-OES (PerkinElmer Optima 4300 DV) for their contents in Sr and Si. The detection limits were approximately 0.1 $\text{mg} \cdot \text{L}^{-1}$ and 0.01 $\text{mg} \cdot \text{L}^{-1}$ for the Si^{4+} and Sr^{2+}, respectively. The remaining solid (sand matrix)

was rinsed with MilliQ water and dried. Again, a few mg of the solid samples that contained the precipitation front were sampled and analyzed with SEM-EDX (FEI Quanta 650 FEG) to ensure that no secondary phase remained and check the efficiency of the dissolution protocol.

3.2 Characterization of the porosity in the clay system

It is possible to estimate the porosity of materials by using an impregnation and autoradiography method, as described by (Hellmuth and Siitari-Kauppi, 1990; Sammartino et al., 2002). Such a method was used on one of the two compacted illite diffusion cells (IdP1). First, the position of the precipitation front was localized with the help of a μCT scan. Then, the sample was impregnated with ^{14}C-PMMA (polymerized ^{14}C-MMA resin) and cut-out in various samples of different orientations. Finally, numerical and film auto-radiography were performed on the different exposed sections. The average porosity of the compacted clay could be estimated at various locations within the sections thanks to the digital and numerical analysis of the autoradiographs.

3.2.1 μCT

Prior to impregnation, the precipitated celestite within the clay sample was localized by μCT on a Viscom X8050-16 (VISCOM AG). The diffusion cell was scanned without the external metallic screws maintaining the cell (c.f. fig. 2.3), as they present high X-ray absorption. The volume was reconstructed from the 1800 projections obtained over 360° of rotation with the software DigiCT v2.4.2 (@Digisens). The spatial resolution obtained was 27.2 μm.

3.2.2 Impregnation

To remove the pore water from the sample, the diffusion cell was placed in an oven at 105°C for 2 weeks (15 days). After drying, the air was removed from the system by placing the cell in a vacuum chamber on a plate heated at 75°C for three days. The impregnation was conducted in the vacuum chamber with a ^{14}C-MMA resin. The activity of the ^{14}C tracer in the resin was 185 MBq $\cdot$ mL^{-1}. An aliquot of Benzoyle Peroxyde (0.5%) was added to the resin as a thermal catalyst. A two-steps protocol ensured that the resin would penetrate in the sample by capillary forces from the inlets and outlets of the diffusion cells, thus filling all connected pores (isolated pores are not accounted for with such a method). First, 64 mL of the ^{14}C-MMA was slowly introduced in the Teflon beaker containing the diffusion cell within the vacuum chamber. Then, after 2 weeks, a second volume of 36 mL was added. The impregnation lasted 19 more days. The sample was then polymerized in a thermal bath with the temperature going from 75°C to 60°C and back to 55°C in 60 hours.

3.2.3 Sampling

The polymerized sample was cut in different directions and the PEEK column containing the compacted illite was removed with a small diamond coated saw. The orientation of the different sections were based on the μCT and ensured that the precipitation front was present in each of them. The sample was first cut in half along the longitudinal direction (in the direction of diffusion), along the diameter of the cylinder. One of the halves was cut in the transverse direction in 3 semi-cylindrical sections, one of which was cut in the longitudinal section. The sections were polished first with a SiC 400 powder (P600, Buehler), and then with diamond suspensions of decreasing grain sizes (15, 3

and 0.05 μm; Metadi Solution, Beuhler). The result of the sampling procedure was the creation of 4 flat surfaces of different orientations. These surfaces are presented in fig. 3.1.

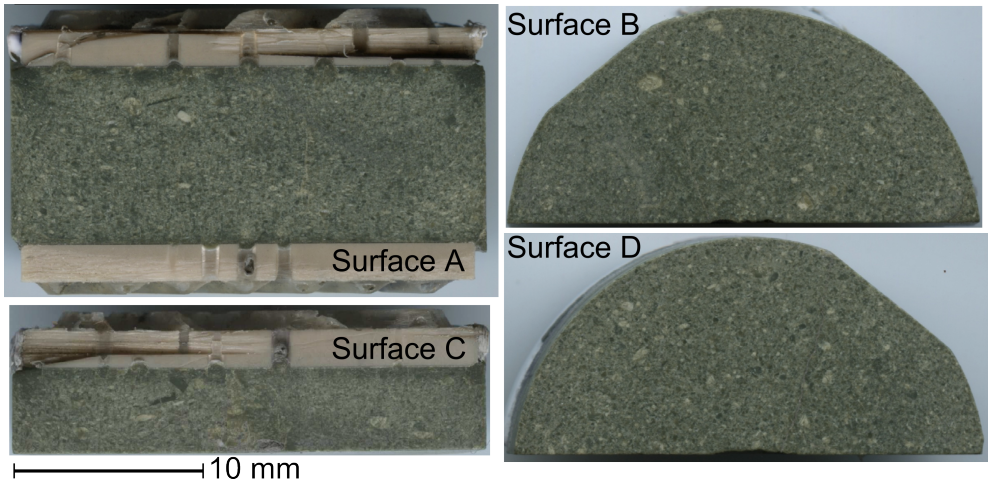

Figure 3.1: Polished surfaces of the different sections cut in the compacted illite-du-Puy sample IdP2.

3.2.4 Autoradiography

Autoradiography is a method that allows the imaging of the tracer activity within the first few tenths of Å below the surface of the samples. The radiographs are digitized to be transcribed into gray-scale images where different gray values correspond to different activity levels. The activity can be correlated with the amount of tracer present in the connected pore-space, and therefore to the average connected porosity of each pixels (or representative volume), given that the density of the mineral phases and of the ^{14}C-PMMA are known. A numerical and film autoradiography techniques were used.

The numerical autoradiography method is based on the excitation of the Eu^{2+} atoms of a photo-sensitive phosphorous screen ($BaFBr:Eu^{2+}$, Fuji Plate BAS TR2025) by the liberation of photons during the photo-stimulation of the surface by a laser

beam. The autoradiographs were digitized in 16 bits images of 25 μm resolution with a scanner. The main advantages of this technique is the short exposure times required for acquisition (a few hours) and a better linearity between optical densities (gray levels) and activities as compared to film autoradiography.

The film autoradiography technique requires the exposition of the polished surface of the samples to a photo-sensitive film (Kodak Biomax MR) in a dark chamber for 5 to 8.5 days. These autoradiographs integrate the beta radiation emitted by the impregnated pores located in a thickness of 100 Å below the surface. For this technique, films have to be exposed to calibration standards of known activity in the same time as the samples. The 20 μm resolution radiographs were digitized in 16 bits with a spatial resolution of 10.4×10.4 μm^2, and converted to 8 bits (256 gray levels).

The local connected porosity is calculated for each pixel using the calibration function, the average grain density (about 2.6 $kg{\cdot}dm^{-3}$ for illite-du-Puy, Fialips and Robinet (2011)) and the tracer activity, as described in details by Sammartino et al. (2002). The estimations and porosity maps of the surfaces were obtained with the software AutoRadio (Prêt, 2003). The software allows for the calculation of the porosity for each pixel of the radiographs, but also for bigger regions and for transects.

Chapter 4

Geochemical modeling

Reactive and non-reactive transport modeling was used to determine the transport properties of the porous materials and reproduce the clogging experiments, to calibrate and build a predictive reactive transport model. The linear regression method presented in section 2.3.2 is a rather simple approach to determine the transport properties of the materials. However, it does not take into account the influence of the filters own transport parameters, a phenomenon called the filter effect. Another method to determine the transport parameters in a more accurate way is by fitting the experimental data with a 1 or 2 dimensions (1D or 2D) transport model, while taking into account the filter properties. The transport models were built with CrunchFlow (Steefel and Lasaga, 1994; Steefel, 2009).

4.1 Non-reactive transport

The HTO through diffusion in compacted sand and illite-du-Puy prior to porosity clogging was modeled in 1D and 2D. The database used with the CrunchFlow gimrt code - thermoddem.dbs (Blanc et al., 2007a) - used the Debye-Hückel formalism. The experiments were often conducted at high ionic strength (up to 0.50 $mol \cdot L^{-1}$ NaCl), a domain where this for-

malism might lead to significant errors. To verify the applicability of this formalism at high ionic strength, a simple activities-fitting study was performed, as described thereafter (section 4.1.1). The main species in solution were HTO, H^+, Cl^-, Na^+ and H_4SiO_4. The secondary species considered were HCl (stability constant at 25°C, $\log K_{HCl} = 0.71$) and NaOH ($\log K_{NaOH}$ =14.75).

The experimental data fitting was done by varying the porosity and tortuosity of the porous material until the modeled HTO flux satisfactorily reproduced the experimental data. To obtain the flux in a constant boundary conditions model, one has to artificially precipitate the tracer in a mesh cell situated just before the reservoirs. Indeed, the reservoirs of the system have constant concentrations, one being the source of the tracer and the other one the sink. As the concentration of HTO in the sink reservoir is kept to 0.0 $\text{mol} \cdot \text{L}^{-1}$, the information on the amount of diffused HTO was retrieved with this simple trick. A phase named HTO_prec was created in the database, with a stability constant at 25°C, $\log K_{HTO\_prec}$ = -99.99, and a precipitation rate of 1×10^{-3} $\text{mol}\cdot\text{m}^2\cdot\text{s}^{-1}$, thus ensuring a complete and fast precipitation of the tracer.

4.1.1 Debye-Hückel vs. Pitzer

To ensure that the Debye-Hückel formalism could accurately describe the system at 0.5 $\text{mol} \cdot \text{L}^{-1}$ NaCl, a simple test was run with PHREEQC code, which contains a Pitzer database (pitzer.dat). The activities of Na^+ and Cl^- ions in a solution of increasing concentrations of NaCl were obtained with the pitzer.dat database. The values were then fitted by changing the activity coefficients of the two main species (γ_{Na^+} and γ_{Cl^-}) when performing the same modeling with the phreeqc.dat database, which uses the Debye-Hückel formalism. The new γ

were then tested in conditions comparable to the experimental conditions.

4.1.2 1D model

The 1D model was based on the diffusion experiments, and was constituted of 2 reservoirs (high and low HTO concentration), 2 filter supports, the porous material and the HTO precipitation grid cell. The conceptual model is schematically presented in figure 4.1. The influence of the meshing of the system was assessed in a parameter sensitivity study (see appendix B), where the mesh size was varied between 1 and 0.05 mm and the results compared. The porosity of the pierced filter supports was set to 0.370 and 0.146 for the sand and illite systems, respectively, with a tortuosity of 1 as the holes were straight cylinders (fig. 2.2). The whole pierced surface was in contact with the compacted material, filters and/or reservoir. The un-pierced part of the supports in the case of the sand system was in contact with the O-rings and diffusion cell walls. Therefore, they were not accounted for in the calculation of the porosity and in the model.

4.1.3 2D models

Two types of 2D models were built: (1) one with homogeneous porosity and tortuosity distribution in the Y direction, and (2) one with a realistic filter sets geometry (heterogeneous distribution of porosity in the Y direction). The second model was built in order to take into account the filter effects in a more realistic way. The porosity and tortuosity values were alternated: grid cells with a value of 1 for both parameters were alternated with grid-cells with a value of 0 for both parameters. The ratio between the two types of grid-cells was equal to the porosity of the filter sets (0.370 and 0.146 for the sand and illite systems,

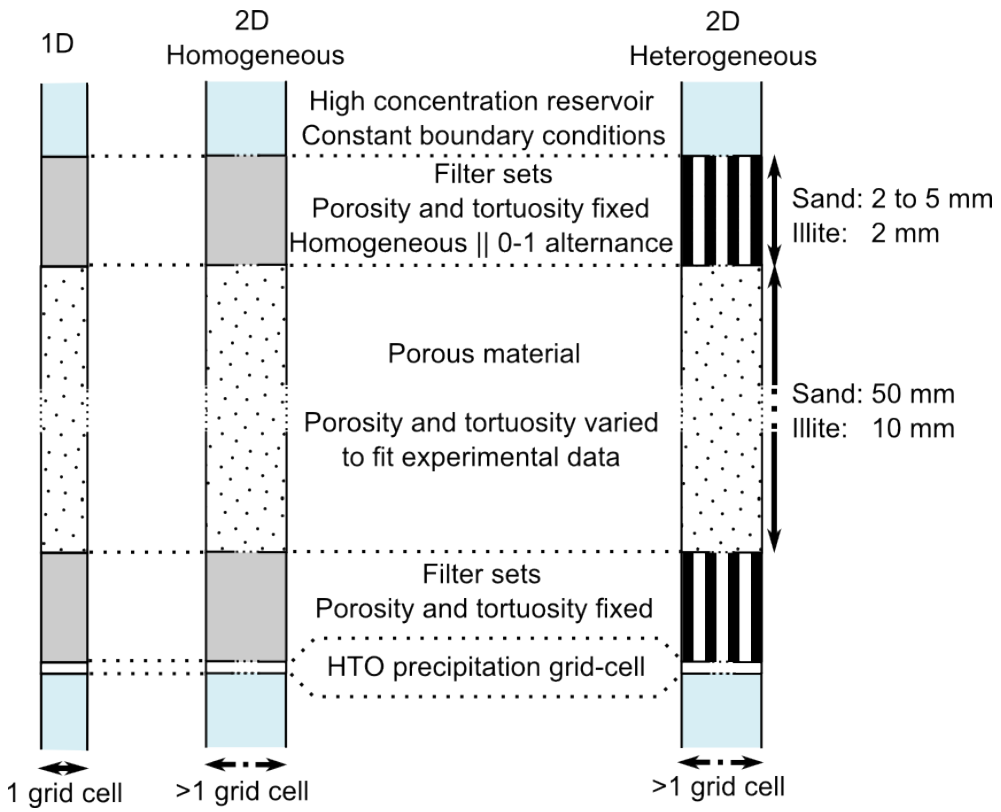

Figure 4.1: Schematic of the conceptual 1D and 2D models used to fit the experimental data on HTO through diffusion in the sea sand and illite-du-Puy systems.

respectively). The conceptual models are illustrated in fig. 4.1. The dimensions and mesh size in the Y direction were varied to test the model's sensitivity to these parameters (appendix B).

4.2 Reactive transport

As for the simple through diffusion (no porosity evolution), the through diffusion during precipitation of celestite and calcite was performed in 1D and homogeneous and heterogeneous 2D models, based on the same conceptual models as depicted in fig. 4.1. The Debye-Hückel activity coefficients were re-calculated for each main species in solution based on a Pitzer fit. The same

trick as for the simple through diffusion simulation consisting in artificially precipitating the tracer in a specific grid-cell was applied in the cases presented thereafter. An extensive parameter sensitivity study was performed on the mesh size, filter geometry, specific surface area of the precipitating mineral phase, precipitation kinetics, reactive or neutral porous material and minimum porosity (see appendix B). The minimum porosity is a limiting value of porosity set in the model input for porosity clogging. It indicates to the code that the porosity cannot decrease below this value, or in other words that once this value is reached, no more precipitation occurs.

The clogging mineral phase was constrained to precipitate only in the porous material. The porosity at a time t (ε_t) was calculated at each time step of the simulation based on the volume fraction of the precipitate formed (ϕ_{prec}) and the volume fraction of the porous material (ϕ_{mat}) or previous porosity (ε_{t-1}), as follows:

$$\varepsilon_t = 1 - (\phi_{prec(t-1)} + \phi_{mat}) = \varepsilon_{t-1} - \phi_{prec(t-1)} \tag{4.1}$$

The volume fraction of the mineral phase was calculated as the number of moles of mineral precipitated in one grid-cell multiplied by the molar volume of said mineral phase (ratio of the molar mass to the density). In a more complex system where several mineral phases are involved in processes of precipitation and dissolution, the volume fractions of each phase must be taken into account. The molar volume of calcite was equal to 36.93 kg·dm^{-3}. The precipitation rate was 1.91×10^{-3} mol·m^2·s^{-1}, and the activation energy was 10.01 kcal·mol^{-1} (from thermoddem.dbs, Blanc et al. (2007a)). The molar volume of celestite was 46.25 kg·dm^{-3}, its precipitation rate was 5.12×10^{-8} mol·m^2·s^{-1}, and its activation energy was 8.13 kcal·mol^{-1} (from thermoddem.dbs, Blanc et al. (2007a), and from Dove and Czank (1995)).

Table 4.1: List of the primary and secondary species considered in the simulation of porosity clogging by celestite and calcite precipitation in the sand and illite system, with stability constants (logK).

Primary species	Secondary species	LogK
Celestite precipitation		
Sr^{2+}	$SrCl^{+}$	0.23
	$SrOH^{+}$	13.29
	$SrSO_4$	-2.30
SO_4^{2-}	HSO_4^{-}	-1.98
	$NaSO_4^{-}$	-0.94
Calcite precipitation		
Ca^{2+}	$CaHCO_3^{+}$	-1.10
	$CaCl^{+}$	0.29
	$CaOH^{+}$	12.78
CO_3^{2-}	$NaCO_3^{-}$	9.06
	$NaHCO_3$	0.25
Common to both systems		
HTO		
H^{+}		
Na^{+}	NaOH	14.75
Cl^{-}	HCl	0.71
H_4SiO_4		

The specific surface area of the reactive phases is an important parameter to take into account. As the specific surface area of the precipitate during the clogging process could not be experimentally determined, different values were tested in order to assess the model sensitivity on this parameter, as it could not be directly measured on the precipitates obtained during diffusion experiments (see appendix B). The value finally chosen was 40 $m^2 \cdot g^{-1}$. The primary and secondary species in solution considered for simulation are listed in table 4.1.

Part II

Results and discussion

Chapter 5

Properties of the purified sea sand

Prior to diffusion experiments, the sand was characterized both as a powder (chemical and mineralogical composition, sorption of strontium) and as a compacted material (porosity, diffusivity and other transport properties). The initial transport properties were also estimated by applying the linear regression method to the conservative tracer (HTO) through diffusion experimental results.

5.1 Physico-chemical properties of the sand powder

The chemical and mineralogical composition of the sand powder was characterized for the raw and the cleaned material. The sorption of strontium was characterized only for the cleaned material.

5.1.1 Chemical and mineralogical composition

The XRD analysis of the bulk powder confirmed that the sand consists almost solely of silica (>99% SiO_2). The impurities

contained at least two minor mineral phases from the kaolinite and mica groups.

The XRD analysis was confirmed by X-ray Fluorescence (XRF) measurements on the bulk powder (table 5.1). The powder mainly consists of silica (97.8 wt% SiO_2). Aluminum was identified as major impurity, with a proportion of 0.9 wt% Al_2O_3. Assuming that Al constitutively enters in the composition of kaolinite would correspond to 2.25 wt% kaolinite in the sea sand. The other major elements found were K, Ti, Fe and Ca, in decreasing order of abundance. The differences in content of the various elements between the cleaned and raw sand are not significant. However, this pre-treatment step is thought to be necessary, as it removes the numerous fine particles that could influence the pore size distribution, and therefore the transport parameters of the compacted material. The presence of fine particles would also lead to greater uncertainties in the μCT measurements, as they might be smaller than the resolution of the apparatus.

Table 5.1: Chemical composition (major and minor elements) of the raw and cleaned sand powder from XRF analysis.

	Major elements (wt%)					
	SiO_2	Al_2O_3	K_2O	TiO_2	Fe_2O_3	CaO
Raw sand	99.1	0.88	0.42	0.10	0.09	0.03
Cleaned sand	99.2	0.89	0.42	0.09	0.09	0.03
	Minor elements (ppm)					
	Ba	Zr	Sr	Rb	Cr	Pb
Raw sand	105	64	19	14	7	3
Cleaned sand	102	55	18	13	7	4

Ba, Ce, Cr, Nd, Rb, Sr and Zr were present in trace amounts (10 to 100 ppm). Their concentration did not change during the cleaning step. Based on the XRF analysis and the total mass of $\approx$ 6.25 g of sea sand inserted in each diffusion column, the Sr

amount is estimated to be 0.12 mg. Such a small amount would not influence the selective dissolution results for the quantification of precipitated celestite. It would lead to an error of +0.25 mg at maximum, under the assumption that all Sr was bond in celestite and would be released during the selective dissolution process.

5.1.2 Specific surface area

The specific surface area (SSA) is a factor that can greatly influence sorption and through diffusion results. The SSA of the sand was not affected by the cleaning procedure, during which the fines were removed. It was equal to 0.53 $m^2 \cdot g^{-1}$ and 0.56 $m^2 \cdot g^{-1}$ for the raw and cleaned material, respectively. The hysteresis in the sorption-desorption curve (fig. 5.1) indicates the presence of meso- to micropores within the sand grains. However, the sorption-desorption curve is of type V, which indicates a poor N_2 sorption on the sand (Brunauer et al., 1940; Balbuena and Gubbins, 1993; IUPAC, 1997). One must be cautious when interpreting such a curve.

5.1.3 Sorption of strontium

Attempts were made to quantify the sorption of Sr^{2+} on the free sand powder, in various ionic strength, pH and solid to liquid ratios. The sorption was found negligible in the conditions relevant to the present study (below 5% at pH $\approx$ 5.5, high ionic strength and 0.001 to 1 $mmol \cdot L^{-1}$ Sr^{2+}). The diffusion experiments with celestite precipitation imply the through diffusion of a high concentration $SrCl_2$ solution (0.01 to 0.5 $mol \cdot L^{-1}$) from a source reservoir to a sink reservoir (SO_4-reservoir), in high background electrolyte (0.03 to 0.75 $mol \cdot L^{-1}$ NaCl) and at constant pH $\approx$ 5.5. The quantity of sorbed Sr^{2+} on the sand surface in these experimental conditions was close to or below

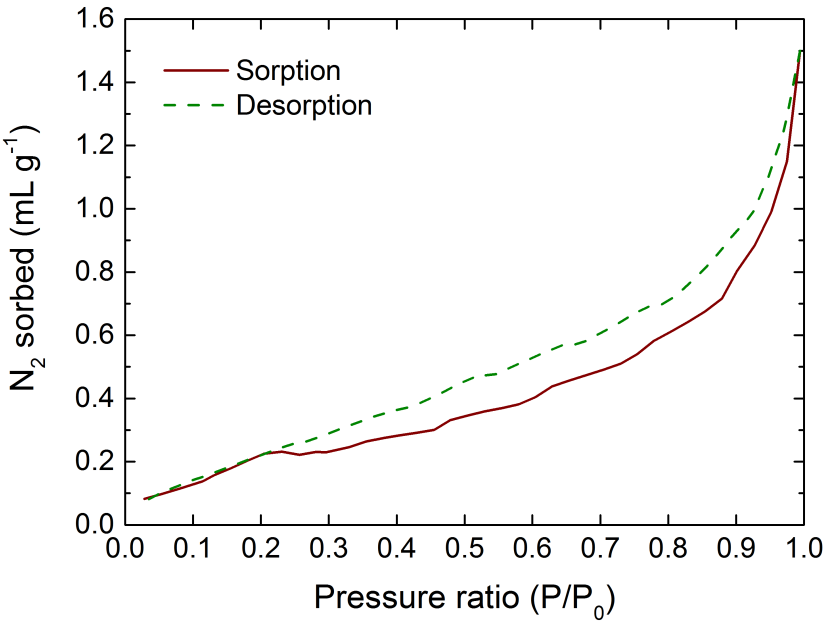

Figure 5.1: N_2-BET sorption-desoption isotherms for the cleaned sea sand.

detection limits ($\approx 5\ \mu g \cdot L^{-1} = 4.4{\times}10^{-4}$ mol $\cdot$ L^{-1}). Based on these results, the retardation of Sr^{2+} ions in their migration in the compacted sand by sorption on the grains surface was not included in the models.

5.2 Initial transport parameters of the compacted sand

The initial transport parameters of the compacted purified sea sand were characterized by (1) MIP (connected porosity and pore size distribution), (2) through diffusion of HTO (accessible porosity, effective diffusivity, geometric factor) and (3) μCT (overall, connected and isolated porosity, effective diffusivity, pore size distribution, tortuosity factor). The results obtained with each of these methods are reported and compared in table 5.2.

Table 5.2: Summary of the average initial transport parameters of compacted sea sand obtained with MIP, HTO through diffusion and μCT.

Technique	ε	ϕ_{av} μm	D_e $\times 10^{-10}$ $m^2 s^{-1}$	G
MIP	0.42 ± 0.01	43.85 ± 0.48	-	-
HTO	0.42 ± 0.09	-	4.48 ± 0.17	2.11 ± 0.42
μCT	0.40 ± 0.08	39.89 ± 5.70	2.21 ± 0.43	2.72 ± 0.39

5.2.1 Mercury intrusion porosimetry

The Pore Size Distributions (Hg-PSD) obtained for the two measured samples (MIP1 and MIP2) are reported in fig. 5.2. The reported distributions are corrected from the glass filters contribution, which had a well known average pore size of 200 μm. The distribution curves are very reproducible, as are the average pore diameter (Φ_{av}), the median pore diameter (Φ_{D50}) and the connected porosity reported in table 5.3.

Table 5.3: Accessible porosity (ε_a) and average and median values of pore diameter (Φ, in μm) obtained on 2 samples of compacted purified sea sand with mercury intrusion porosimetry.

Sample	ε_a	Φ_{av}	Φ_{D10}	Φ_{D50}	Φ_{D90}
MIP1	0.404	43.37	17.90	40.17	63.21
MIP2	0.427	44.32	5.73	41.35	71.44

5.2.2 Tracers through diffusion

The results of the HTO through diffusion experiments - as depicted in fig. 5.3 and table 5.4 - show a high reproducibility in the through diffusion curves and transport parameters obtained with the linear regression method.

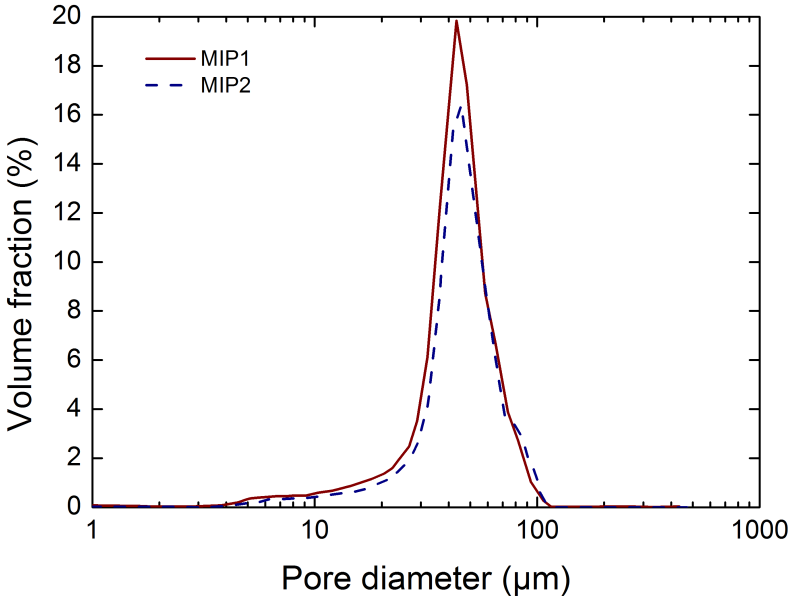

Figure 5.2: Pore size distribution of compacted purified sea sand from MIP measurements (Hg-PSD) on 2 samples.

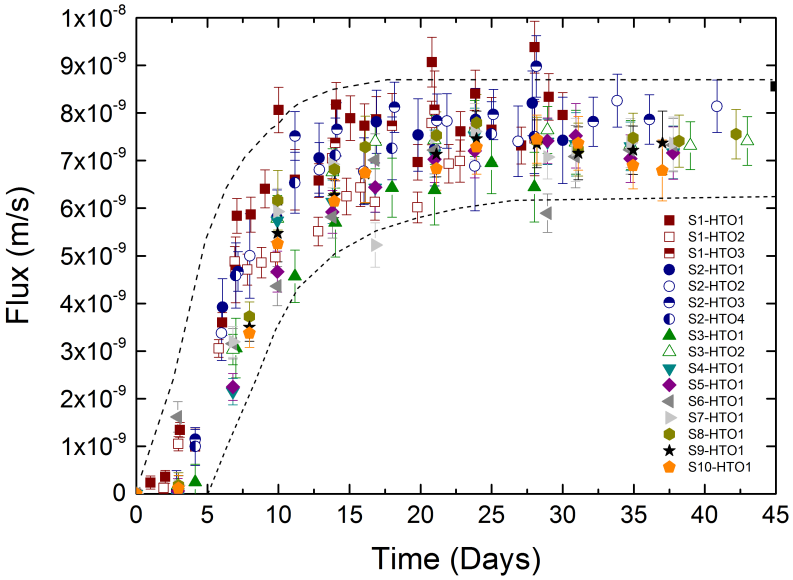

Figure 5.3: HTO flux for through diffusion experiments in compacted purified sea sand prior to porosity reduction. The dashed lines represent the boundaries of the confidence interval.

Table 5.4: Accessible porosity (ε_a), effective diffusivity (D_e, in $\times 10^{-10}$ $m^2 \cdot s^{-1}$), geometric factor (G) and cementation factor (m) obtained on 10 samples of compacted purified sea sand with HTO through diffusion and linear regression method.

Experiment	ε_a	D_e HTO	G $\approx \tau_f^2$	m
S1-HTO1	0.372 ± 0.015	3.43 ± 0.14	2.43 ± 0.24	1.90 ± 0.11
S1-HTO2	0.347 ± 0.014	3.71 ± 0.15	2.09 ± 0.21	1.70 ± 0.10
S1-HTO3	0.393 ± 0.016	4.39 ± 0.18	2.00 ± 0.20	1.74 ± 0.10
S2-HTO1	0.441 ± 0.018	3.46 ± 0.18	2.27 ± 0.23	2.00 ± 0.11
S2-HTO2	0.463 ± 0.019	3.66 ± 0.20	2.28 ± 0.23	2.07 ± 0.09
S2-HTO3	0.331 ± 0.013	4.51 ± 0.18	1.69 ± 0.17	1.48 ± 0.08
S2-HTO4	0.394 ± 0.016	4.23 ± 0.17	2.08 ± 0.21	1.79 ± 0.10
S3-HTO1	0.441 ± 0.018	4.04 ± 0.16	2.44 ± 0.24	2.09 ± 0.12
S3-HTO2	0.394 ± 0.016	4.48 ± 0.18	1.96 ± 0.20	1.72 ± 0.10
S4-HTO1	0.472 ± 0.019	4.52 ± 0.18	2.34 ± 0.23	2.13 ± 0.12
S5-HTO1	0.502 ± 0.020	4.44 ± 0.18	2.53 ± 0.25	2.35 ± 0.13
S6-HTO1	0.409 ± 0.016	4.43 ± 0.18	2.07 ± 0.21	1.81 ± 0.10
S7-HTO1	0.425 ± 0.017	4.52 ± 0.18	2.10 ± 0.21	1.87 ± 0.11
S8-HTO1	0.404 ± 0.016	4.62 ± 0.19	1.95 ± 0.20	1.74 ± 0.10
S9-HTO1	0.442 ± 0.018	4.45 ± 0.18	2.22 ± 0.22	1.98 ± 0.11
S10-HTO1	0.453 ± 0.018	4.46 ± 0.18	2.27 ± 0.23	2.03 ± 0.08
Average	0.418 ± 0.087	4.48 ± 0.16	2.11 ± 0.42	1.92 ± 0.44

5.2.3 μCT imaging

μCT with a resolution of $\approx$ 12 to 15 μm were performed on 7 different diffusion cells prior to porosity clogging, 5 of which were segmented both with and without Non Local Mean (NLM) filtering (Buades et al., 2005). All imaged volumes were segmented and implemented in a pore morphology model.

Table 5.5: Total porosity (ε), effective diffusivity (D_e, in $\times 10^{-10}\ m^2 \cdot s^{-1}$) and geometric factor estimated with μCT coupled to a pore morphology model for 7 different diffusion cells containing compacted purified sea sand, prior to porosity clogging.

Sample	NLM filter	ε ($= \varepsilon_a$)	D_e	G $\approx \tau_f^2$
CT1	no	0.321	1.78	2.84
CT1	yes	0.417	2.81	2.33
CT2	no	0.378	2.29	2.66
CT2	yes	0.383	2.14	2.88
CT3	no	0.420		
CT3	yes	0.328		
CT4-mes1	no	0.369	2.21	2.62
CT4-mes1	yes	0.388	2.02	3.01
CT4-mes2	no	0.432		
CT4-mes2	yes	0.357		
CT4-mes3	no	0.406		
CT4-mes3	yes	0.375		
CT5	no	0.494		
CT5	yes	0.445		
CT6	no	0.359		
CT7-seg1	no	0.462		
CT7-seg2	no	0.402		

The porosities (overall ε, connected or accessible ε_a and closed ε_x), effective diffusivity and geometric factor obtained are reported in table 5.5. All pores were connected, thus $\varepsilon = \varepsilon_a$. The effective diffusivity and tortuosity were evaluated only for 3 samples, as such calculations are expensive in CPU time. In order to test the reproducibility of the procedure, the sample CT4 was measured and implemented in the model three times independently and the same data set of sample CT7 was segmented two times independently.

Pore size distribution (PSD)

The geometrical PSD (Geo-PSD) and the mercury intrusion simulation (Hg-PSD) obtained for the unfiltered sample CT1 with the pore morphology model is similar in the range of pore sizes to the Hg-PSD from mercury intrusion porosimetry (fig. 5.4), as are the average and median pore diameters (table 5.6). The lack of data in the small sizes (<12.7 μm) is due to the μCT resolution limit.

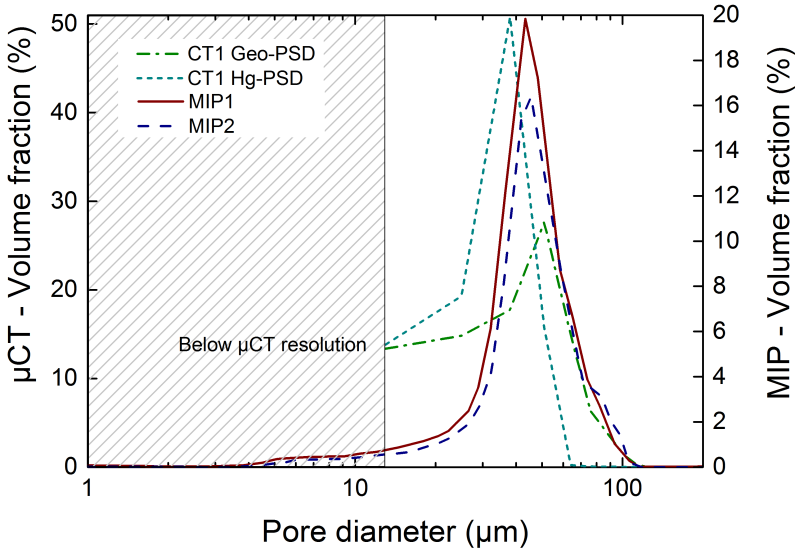

Figure 5.4: Pore size distribution of compacted purified sea sand from μCT, with geometrical calculation and mercury intrusion simulation compared to MIP measurements.

Table 5.6: Average and median values of pore diameter (ϕ, in μm) obtained on a sample of compacted purified sea sand with μCT coupled to pore morphology modeling, from geometrical calculations (Geo) and mercury intrusion simulation (Hg).

Sample	ϕ_{av}	ϕ_{D10}	ϕ_{D50}	ϕ_{D90}
CT1 (Geo)	45.49	9.73	39.92	66.82
CT1 (Hg)	34.21	9.40	29.32	43.06

Total porosity

The effects of the NLM filtering on the porosity estimation does not show a clear tendency towards either a larger or a smaller porosity as compared to the non-filtered datasets, as evidenced by the variability in $\Delta\varepsilon = \varepsilon(NLM) - \varepsilon(no - NLM)$ depicted in fig. 5.5. The range of porosities is slightly smaller in the case of filtered data (0.328-0.445) compared to the unfiltered sets (0.321-0.494). When comparing the 3 different measurements obtained for the same sample (CT4), the same variability in porosity is observed. The average porosity for this sample is equal to 0.402 ± 0.033 for the non-filtered and 0.373 ± 0.016 for the filtered data sets.

All data sets presented here were obtained in identical apparatus settings (distance of the sample from the source, physical filter, energy, acquisition angles and time). A slight variation in energy during the acquisition could partly explain the variability observed. However, the most probable source of discrepancy in this particular case would be during the post processing of the data sets, when the volumes are segmented by the post-processor. The post-processor selects the thresholds on the grey scale corresponding to the porous material and pore space from the histogram of the 16 bits images. Small differences in threshold values can results in significantly different porosities, as evidenced by the results obtained for two different segmentations of the same measurement of CT7 (0.462 and 0.402). Considering all data, an average porosity of 0.396 ± 0.075 is obtained.

Porosity spatial variability

To assess the porosity spatial variability of the compacted sand columns, the porosity profiles of a few samples were calculated with a simple voxel-counting approach (VCA). For this approach, the 2D slices of the reconstructed volumes were considered inde-

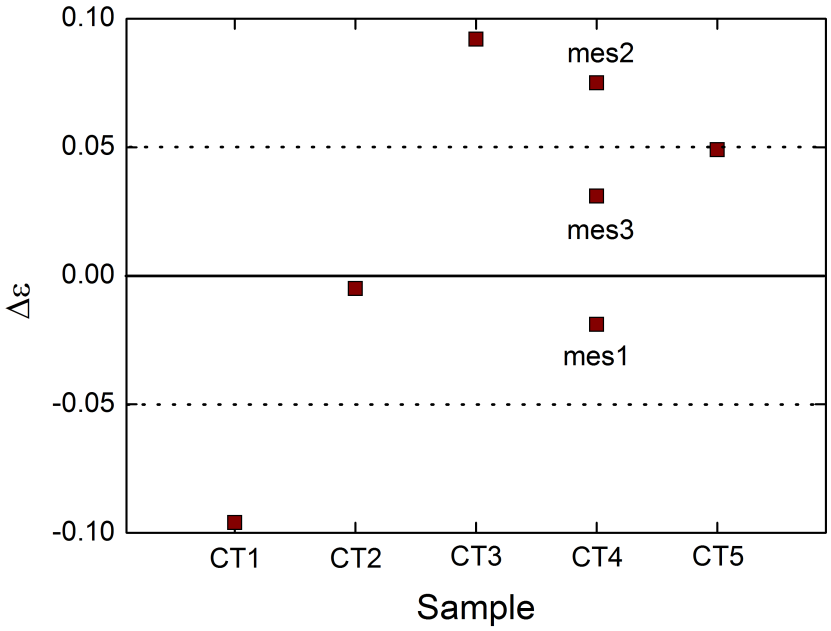

Figure 5.5: Differences in porosities estimated with a pore-morphology model between filtered and unfiltered μCT data sets.

pendently, and the number of pixels corresponding to the pore space were counted from the histograms. This number was then converted in terms of porosity, by simply calculating the ratio between the pixels corresponding to the pore space to the total number of pixels of the column (pore space and grains). To better compare the different data sets, the variation of the porosity along the sand columns was calculated as the difference between the average porosity of the stack of images (ε_{av}) and the porosity of each independent slices (ε_{slice}). The profiles are reported in fig. 5.6 as a function of the distance from the filter supports of the high concentration reservoir.

The porosity varies with the height of the sand column, with more or less intensity depending on the samples. At maximum, the difference between the smallest and biggest value of porosity for the same sample is 0.097 (sample CT1). This variability is most likely due to the compaction method used for the sample:

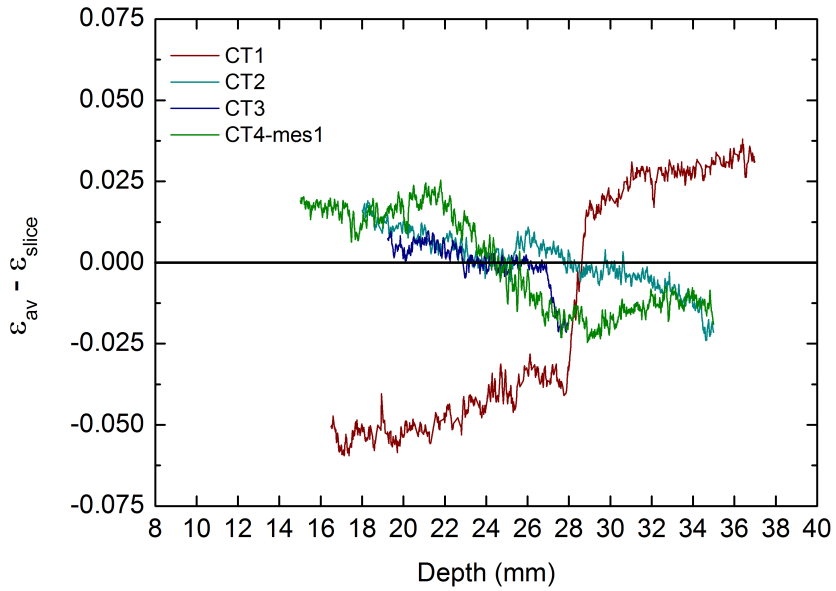

Figure 5.6: Porosity profiles from μCT measurements on different compacted sand columns.

a progressive gravity settling of particles in suspension, with episodes of compaction by tapping the column on the preparation table (section 2.1.2). The effects of such variations on the overall diffusivity of the conservative tracer and precipitation of secondary phases were tested in the reactive transport models.

Diffusivity and tortuosity

As for the porosity, the differences between the effective diffusivity and tortuosity values between the different CT samples are small - but significant - and no clear trend appears when comparing the filtered to the non-filtered data sets. The average effective diffusivity value obtained ($(2.21 \pm 0.43) \times 10^{-10}\ m^2 \cdot s^{-1}$) is only half of the value obtained by HTO tracing ($(4.48 \pm 0.17) \times 10^{-10}\ m^2 \cdot s^{-1}$), and the average tortutosity value (2.72 $\pm$ 0.39) is 1.3 times smaller than the HTO one (2.11 $\pm$ 0.42). This difference between the two approaches most likely lies in the low resolution and poor contrast of the μCT images. Dur-

ing the segmentation process, it appeared that the smaller pores and pore throats could not be differentiated from the sand grains (fig. 5.7), thus leading to a loss of connectivity of the pore space. The number of pore throats and small pores that could not be resolved is small enough that it does not influence the overall porosity. However, the loss of connections has a big influence on the complexity of the diffusion pathways, and therefore on the tortuosity and effective diffusivity.

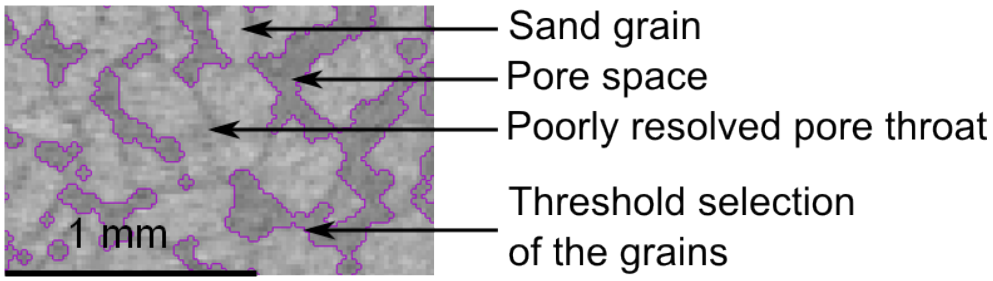

Figure 5.7: Close-up of a CT slice of diffusion cell CT1 during the segmentation process. The purple line correspond to the selection of the grains from the histogram.

Chapter 6

Effects of porosity clogging on transport properties

The HTO flux during porosity reduction by precipitation of celestite and calcite was an indicator of the clogging onset (change of slope), and of its effects on the transport properties of the materials. The precipitation fronts in the compacted sand were analyzed both *in-vivo* (μCT imaging) and *post-mortem* (SEM-EDX and selective dissolution). In the case of the illite-du-Puy, the precipitation front was analyzed only *post-mortem* (autoradiography).

6.1 The compacted purified sea sand

In the compacted sand, the precipitation fronts were sharp disks located near the middle of the diffusion columns. One compacted sand column used for the precipitation of celestite from 0.5 mol $\cdot$ L^{-1} stock solutions (sample named CTprec1) was analyzed with μCT at 2 different resolutions (5.89 and 15.2 μm) and its transport parameters (porosity, diffusivity and tortuosity) were characterized with pore-morphology modeling. For this experiment, no radioactive tracer was used, as the μCT scans were performed in a regular laboratory. The initial experimental

conditions were the same as for the diffusion cell S13-CEL° and S14-CEL° (1 mmol $\cdot$ L^{-1} NaCl pore solution).

6.1.1 HTO through diffusion

The HTO fluxes obtained for celestite and calcite precipitation experiments are reported in fig. 6.1.

Clogging by celestite

Two different patterns can be distinguished between the high concentrations ($\geq$ 0.50 mol$\cdot L^{-1}$ $SrCl_2$ and Na_2SO_4) and the low concentrations ($\leq$ 0.10 mol$\cdot L^{-1}$ $SrCl_2$ and Na_2SO_4). In the first case, a normal increase in the HTO flux - behavior corresponding to an undisturbed porous material - is observed during the first few days, followed by an important decrease leading to a seemingly steady state flux ($\approx 2.4 \times 10^{-9}\ m \cdot s^{-1}$) about 3 times lower than for undisturbed compacted sand ($\approx 7.6 \times 10^{-9}\ m \cdot s^{-1}$). The onset of the flux decrease at about 7 to 9 days corresponds to the appearance of a precipitation front visible to the naked eye, shaped as a thin white disk (<1 mm thick) and perpendicular to the direction of diffusion. The front was close to the middle of the sand columns, though slightly closer to the Sr-reservoir (table 6.1). The non-zero steady state HTO flux indicates that the pore space in the precipitation zone was not fully clogged, and that it remained at least partially open and connected. It also seems to indicate that most of the precipitation occurred very rapidly and stopped abruptly. A good reproducibility was observed for the two experiments conducted at 0.50 mol $\cdot$ L^{-1} concentrations (fig. 6.2), which validated the reliability of the approach.

In the case of low concentrations, the HTO flux did not seem to be affected by porosity reduction. Indeed, the shape of the curve was similar to the curves obtained prior to poros-

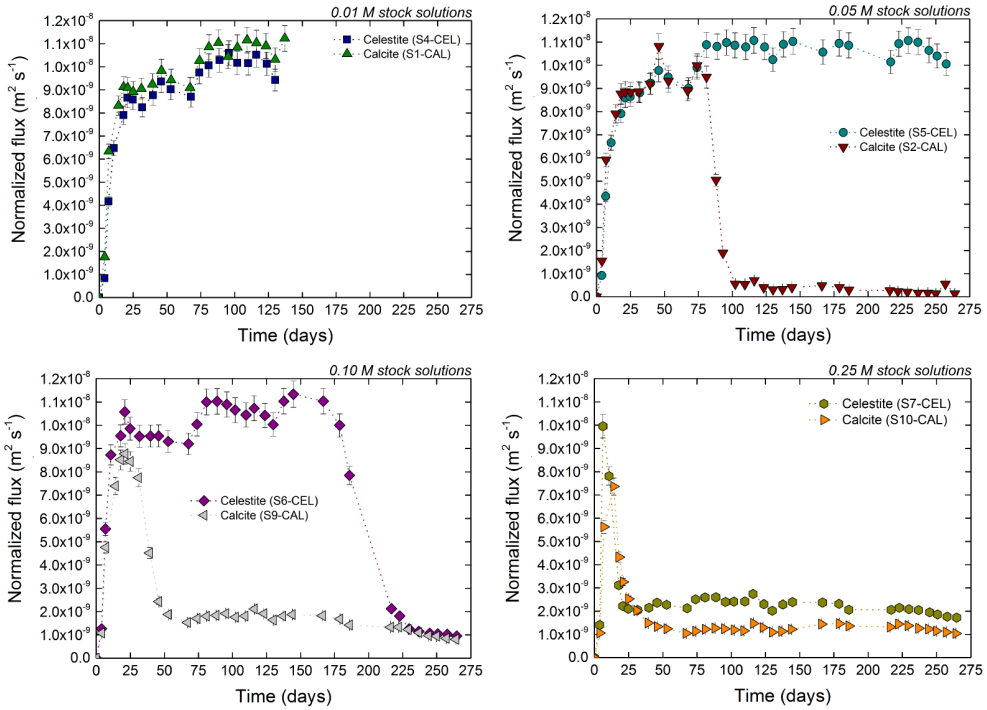

Figure 6.1: HTO through diffusion fluxes during compacted sand porosity reduction by celestite and calcite precipitation from different concentrations ($SrCl_2$ and Na_2SO_4; $CaCl_2$ and Na_2CO_3).

ity reduction. However, the value of the steady state flux ($\approx 1.08 \times 10^{-9}\ m \cdot s^{-1}$) is slightly higher than for no-precipitation experiments ($\approx 7.6 \times 10^{-9}\ ms^{-1}$). This 30% difference is significantly higher than the experimental error of 5 to 10%, and could be due to the differences in initial conditions. Indeed, for the no-precipitation experiments, the HTO through diffusion was performed at homogeneous NaCl concentration (0.001 and 0.500 $mol \cdot L^{-1}$ NaCl in the reservoirs and pore space), while the precipitation experiments S5-CEL, S6-CEL and S7-CEL (fig. 6.1) were performed at homogeneous ionic strength (different salt concentrations between the reservoirs and the pore solution). These high concentration gradients could lead to faster diffusion rates.

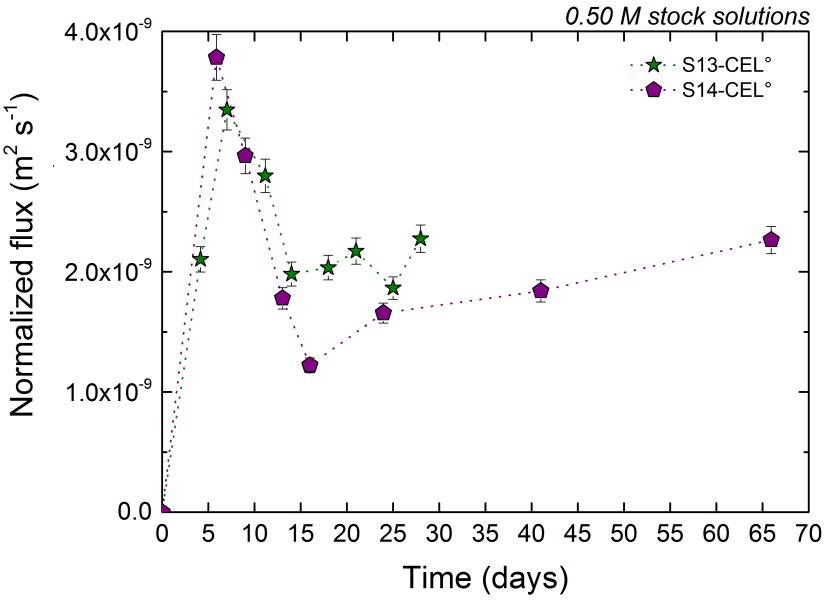

Figure 6.2: HTO through diffusion fluxes during compacted sand porosity reduction by celestite precipitation from 0.50 mol $\cdot$ L^{-1} $SrCl_2$ and Na_2SO_4.

Clogging by calcite

The HTO fluxes obtained during the sand porosity clogging by precipitation of calcite (fig. 6.1) follow the same general trend as for the high concentration reservoir celestite experiments. A first increase in the flux corresponding to the HTO migration through an undisturbed media is followed by a rapid decrease and a steady-state. However in the calcite case, the HTO fluxes are influenced by porosity reduction also at relatively low concentrations (0.10 and 0.05 mol $\cdot$ L^{-1} $CaCl_2$ and Na_2CO_3). The time corresponding to the flux drop increases with decreasing concentrations, and was not reached for the smallest reservoir concentration (0.01 mol $\cdot$ L^{-1}). The flux reached a steady state value of 0.4×10^{-9} $m \cdot s^{-1}$ for S2-CAL, 1.8×10^{-9} $m \cdot s^{-1}$ for S35-CAL and 1.3×10^{-9} $m \cdot s^{-1}$ for S36-CAL after precipitation. These values are about 4 to 20 times lower than for simple through diffusion, the effects of the porosity reduction be-

ing particularly strong in the 0.05 mol $\cdot$ L^{-1} concentration case. This significant difference with the 0.25-0.10 mol $\cdot$ L^{-1} reservoir concentrations could possibly be due to different precipitation mechanisms involved (clogging of the pores and pore throats or of the pores only).

Clogging by celestite vs. calcite

The trends observed for celestite and calcite precipitation are very different. Calcite precipitation seems to clog the sand porosity faster and more efficiently than celestite. This difference cannot be explained only in terms of precipitation kinetics. The precipitation rate at 25°C for calcite (1.82×10^{-7} mol $\cdot$ $m^{-2}\cdot s^{-1}$) is about 3.6 times higher than for celestite (5.18×10^{-8} mol $\cdot$ $m^{-2}\cdot s^{-1}$) (from thermoddem.dbs database, Blanc et al. (2007a)). However, the precipitation rates are not expected to play such an important role in diffusive conditions, as the migration of the constituting elements is slow enough to consider that the reactions are taking place at local equilibrium. We compared the results obtained for local equilibrium to kinetic regime for celestite in a model sensitivity analysis (appendix B): the differences between both regimes were insignificant. Celestite and calcite also have different molar volumes (46.25 $cm^3\cdot$ mol^{-1} for celestite and 36.93 $cm^3\cdot$ mol^{-1} for calcite), that could explain the faster clogging in the case of calcite. A mass of 10 mg of precipitate would correspond to 9.7 mm^3 of calcite and only 2.5 mm^3 of celestite, a value about 4 times smaller. Finally, experimentalists have observed significant effects of H_4SiO_4 in solution on celestite precipitation (Pina and Tamayo (2012); Louis Temgoua, personal communication). For example, a H_4SiO_4 concentration as low as 1.5 ppm increased the precipitation induction time by 180 min at SI = 0.90 (Louis Temgoua, personal communication). The amount of H_4SiO_4 in solution in our experimental

conditions was 4.8 ppm (added in the reservoirs and calculated pore concentration for equilibrium with quartz). A combination of these three processes could explain the differences between calcite and celestite clogging rates.

Continuous measurements

The results presented and discussed above were obtained on diffusion cells that were previously used in simple through diffusion experiments. The reservoirs and pore water were exchanged against a non-active NaCl solution until no activity could be measured, and then used for the precipitation experiments. A particular set of experiments was run with directly exchanging the 0.50 $mol \cdot L^{-1}$ NaCl solutions in the reservoirs after a first tracing experiment for 0.50 $mol \cdot L^{-1}$ $SrCl_2$-Na_2SO_4 (S12-CEL) and $CaCl_2$-Na_2CO_3 (S34-CAL) solutions while skipping the cleaning step, so that a continuous through diffusion flux could be obtained (fig. 6.3). The exchange was performed at 43 days, after the HTO flux reached a first steady state value of $\approx 7.6 \times 10^{-9}$ m$\cdot$ s^{-1} for both experiments.

Changing the reservoir contents drastically increased the HTO flux in the 3 days following the exchange. The flux peaked at 1.21×10^{-8} m$\cdot$ s^{-1} for the celestite experiment and at 1.91×10^{-8} m$\cdot$ s^{-1} for the calcite experiment. These particularly high values could be due to the ionic strength heterogeneities introduced by exchanging the reservoirs, which had higher ionic strength than the pore water. In the calcite system, the increase was further enhanced by the high heterogeneities in the pH of the solutions, which was 5.5 for the pore water and Ca-reservoir and 11.5 for the CO_3-reservoir. After only 3 to 4 days, the HTO flux of both systems drastically decreased and reached a similar steady state value of $\approx 2.7 \times 10^{-9}$ m$\cdot$ s^{-1}, a value about 3 times lower than the first steady state. In both cases, a clear white disk-shaped

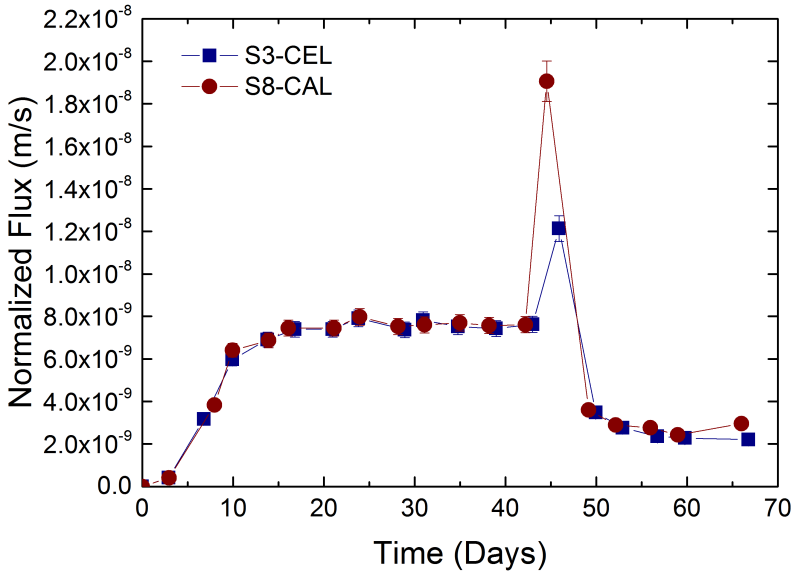

Figure 6.3: HTO through diffusion fluxes prior to and during compacted sand porosity reduction by celestite and calcite precipitation from 0.50 $\text{mol} \cdot \text{L}^{-1}$ concentrations.

precipitation front was visible to the naked eye after 5 to 7 days following the change in reservoir solutions. This period corresponded to the time needed to reach the second steady state.

6.1.2 Characterization of the precipitates

After preparing the samples for *post-mortem* analysis, and before the dissolution of the precipitate was performed, small aliquots from the precipitation zones in cells S3-CEL, S13-CEL° and S14-CEL° were analyzed by SEM-EDX. Representative SEM backscatter images are shown in fig. 6.4. The precipitates took the form of microscopic crystals aggregates of various shapes and sizes. Some of the aggregates were piles of tabular crystals, while others in the direct neighborhood were clusters of needle-shaped crystals. The shape of the celestite crystals was shown to be highly dependent upon the Sr/SO_4 molar ratio by Sun et al. (2012).

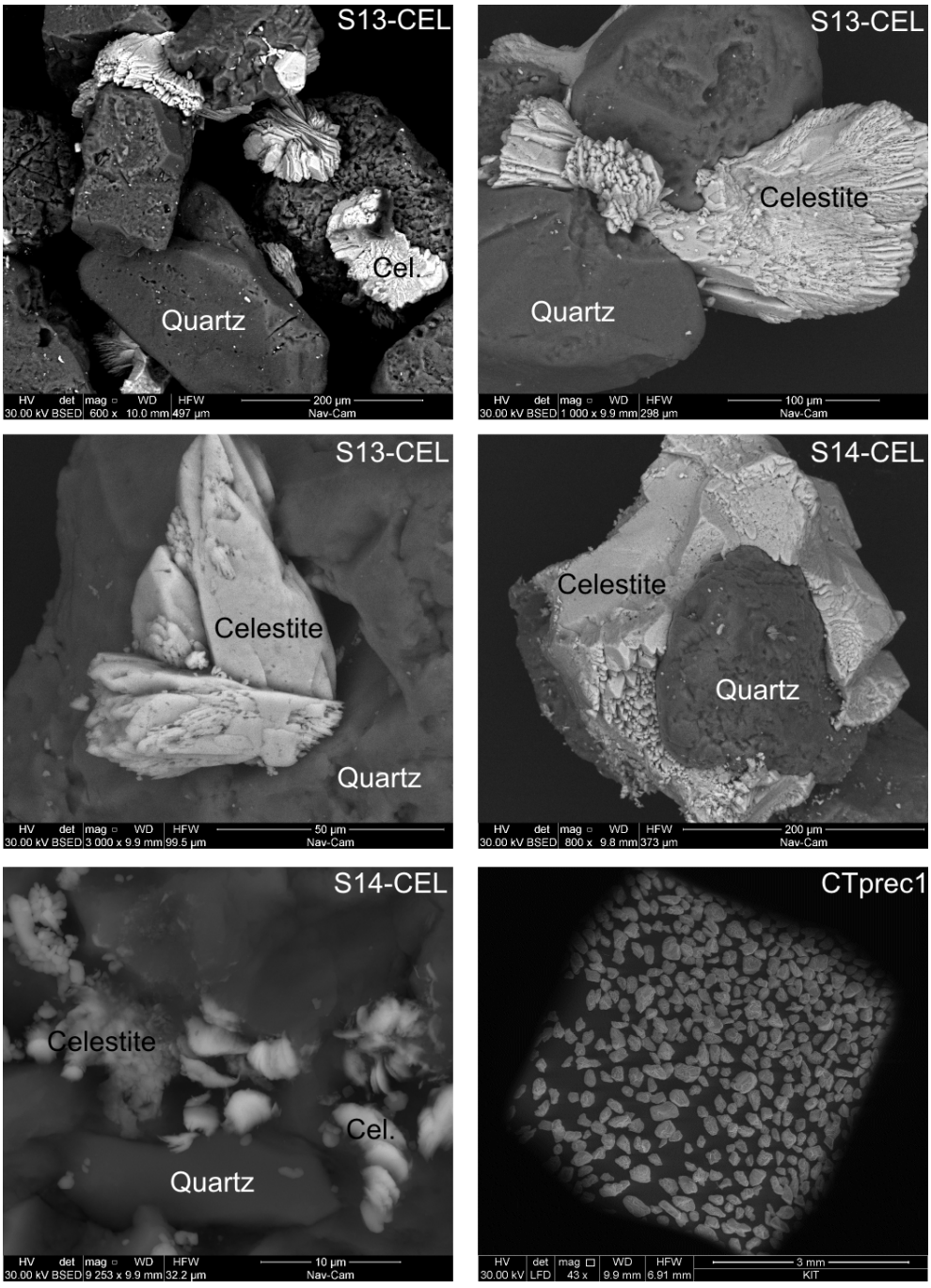

Figure 6.4: Back scatter images of solid samples from experiments S13-CEL° and S14-CEL° before selective digestion of the celestite, and of CTprec1 after selective digestion of the celestite.

Thus, it is possible that the different shapes appeared at different stages of the counter ion diffusion, for different molar ratios. The precipitates seemed to prefer the rough surface of the sand grains, filling the micro-cracks. The aggregates were found isolated on the grains surface, or filling the pore space between several grains, thus cementing them together. The size of the celestite crystals ranged from a few μm to more than 50 μm. A significant number of small crystals were found as isolated "dust" on the surface of the sand grains, very often observed on surface cavities or micro-crack.

An EDX analysis on some of the crystals confirmed that the precipitate was stoichiometric celestite ($SrSO_4$) and that strontianite ($SrCO_3$) has not been formed even though the experiments were performed under atmospheric condition. The saturation index of $SrCO_3$ under the experimental conditions was estimated to be -0.42 for a mixture of 0.5 mol $\cdot$ L^{-1} $SrCl_2$ and 0.5 mol $\cdot$ L^{-1} Na_2SO_4 and solutions in equilibrium with atmospheric CO_2.

Table 6.1: Mass of celestite (m_{SrSO_4}) in 4 experiments, and approximate distance of the precipitation front from the filter supports of the Sr-reservoir (d_{front}).

Diffusion cell	m_{SrSO_4} mg	d_{front} mm
CTprec1	21.7 ± 0.4	21.0 ± 1.0
S3-CEL	15.6 ± 0.3	26.2 ± 0.4
S13-CEL°	31.6 ± 0.5	12.5 ± 2.5
S14-CEL°	35.6 ± 0.5	17.5 ± 2.5

The mass of precipitate, as well as the approximate position of the precipitation fronts, are reported in table 6.1. As can be seen from the celestite mass profiles (fig. 6.5), the front position is variable, but it's amplitude is reproducible. The position is

very approximate, as the solid samples used for the digestion were 5 mm thick, and the position was not measured precisely (except for S3-CEL). Most of the precipitated mass is concentrated in one 5 mm distance interval for each experiment, with part of the precipitation front within the neighbor intervals. No celestite was found in intervals further away from the front. The selective digestion method proved to be efficient, as no celestite remained in the sample from the precipitation front of experiment CTprec1 after dissolution (fig. 6.4).

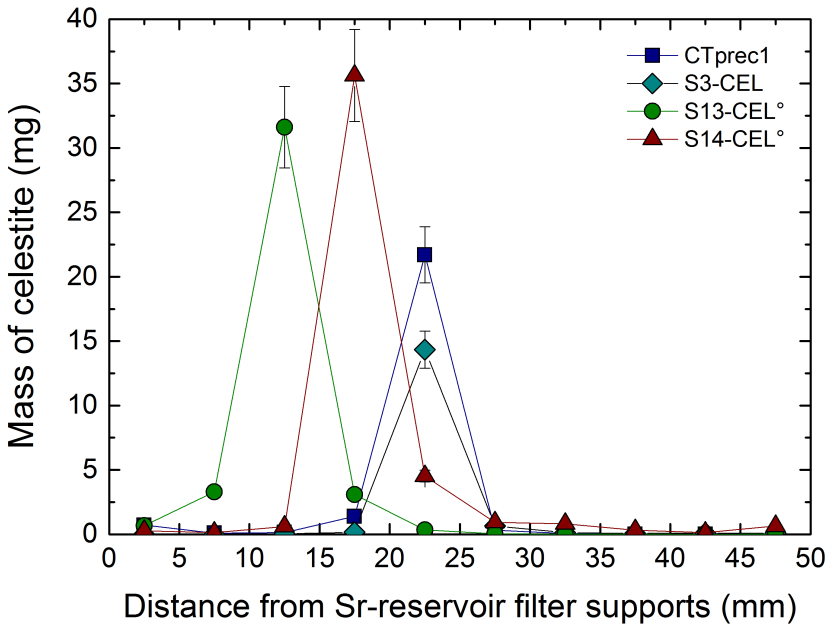

Figure 6.5: Mass of precipitated celestite as a function of the distance from the Sr-reservoir filter supports from selective dissolution analysis.

6.1.3 μCT imaging

Two CT measurements of CTprec1 precipitation front after 63 days of reaction time were made: one at low resolution (15.12 μm), measuring the central 30 mm of the diffusion column, and one at higher resolution (5.89 μm), measuring the central 12 mm

across the precipitation area. The low and high resolution data sets were analyzed with a simple VCA, and the high resolution data set was further segmented and implemented in the pore morphology model.

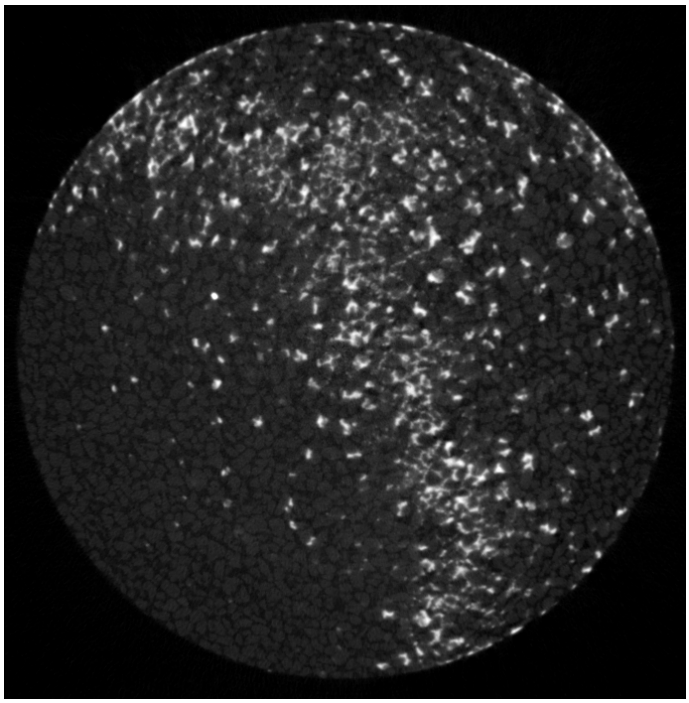

Figure 6.6: μCT slice of cell CTprec1 showing the celestite precipitation front (light gray values) within the sand (medium gray values). The pores appear as the darkest gray values. Diameter is 10 mm.

Under both resolutions, the precipitation front could be clearly distinguished from the sand grains and water filled pore space. The celestite grains appeared as bright white spots after reconstruction (fig. 6.6), as strontium X-Ray mass energy-absorption coefficient is very high compared to silicon (Hubbell and Seltzer, 1995). The precipitation front was symmetrical and constituted of two distinct components: a dense precipitation disk of about 0.35 mm thickness surrounded on both sides by a homogeneously disperse precipitation zone of about 3 mm thickness. In the dense disk, the precipitates appeared to cement the sand grains

together by filling the pores and some of the pore throats. The celestite did not fully cement the sand, as some pathways remained open, connecting one side of the front to the other. In the disperse precipitation zone, the precipitates were isolated and appeared to fill only the pores, and not the pore throats.

Porosity and mass quantification in low resolution

The low resolution data set had a very high contrast between the celestite precipitate and the other components of the porous material (sand grains and pore space). Due to that contrast, the variations in gray levels assigned to either one of these components in the precipitation zone was very important in the X, Y and Z directions. Therefore, the sand grains and pore space could not be segmented in 3D. However, the gray levels assigned to the celestite were very constant and easy to threshold in the X-Y plane (perpendicular to the direction of diffusion).

A VCA was performed, attempting to estimate the mass of precipitate in the pore space and the remaining porosity. A volume of 5.1 $\pm$ 0.8 mm^3 celestite, and a corresponding mass of 20.2 $\pm$ 3.2 mg were estimated. This mass is in good agreement with the dissolved amount of celestite in the 5 mm thick sample containing the precipitation front during the *post-mortem* analysis of the same diffusion cell (21.7 $\pm$ 0.4 mg, see table 6.1 CTprec1).

The initial porosity of the sand column was estimated with a similar VCA for the pore space in the regions far from the precipitation zone. In these regions, the absence of celestite allowed for homogeneous gray levels in the 3 Cartesian directions. An initial porosity of 0.44 $\pm$ 0.05, in good agreement with all other experimental results (0.40 to 0.42), was estimated. From the volume of precipitated celestite and the initial porosity, the minimum porosity reached in the 350 μm thick dense precipita-

tion disk could be estimated. Considering that approximately 75% of the precipitate was included in this dense precipitation disk, a minimum porosity of 0.28 ± 0.03 was estimated. Unfortunately, it was not possible to estimate the connectivity of this remaining porosity with this low resolution set of images.

Porosity and mass quantification in high resolution

The mass of celestite precipitate and the porosity profile were also determined with VCA on the segmented volume. This method gave 30.2 ± 0.5 mg celestite, a value higher than the quantification by dissolution (21.7 ± 0.4 mg). This over estimation could be due to the selection of the gray values threshold corresponding to celestite selected prior to the beam hardening correction. A similar measurement on the raw (untreated) data set gave 25 ± 5 mg. The discrepancy observed does not reside in an incomplete dissolution of the precipitate during the *post-mortem* analysis, as SEM-EDX analysis showed that no celestite remained after treatment (fig. 6.4). It might however come from a microporosity of the precipitate. Indeed, a close look to the untreated CT images reveals that the precipitate has variable grey values, corresponding to possible variable densities. On the SEM images of the precipitates of experiments S13-CEL° and S14-CEL°, the aggregates appeared to have a micro- or nanoporosity.

The shape of the celestite aggregates seems to indicate that the crystals have grown on the surface of the sand grains and filled the adjacent pores, thus leading to a cementation of the porous material in the precipitation zone. However, this cementation was not complete, and a significant portion of the pore space remained unclogged, as is suggested by the porosity profile obtained by VCA on the segmented CT data set of experiment CTprec1 (fig. 6.7). This observation is in good agreement

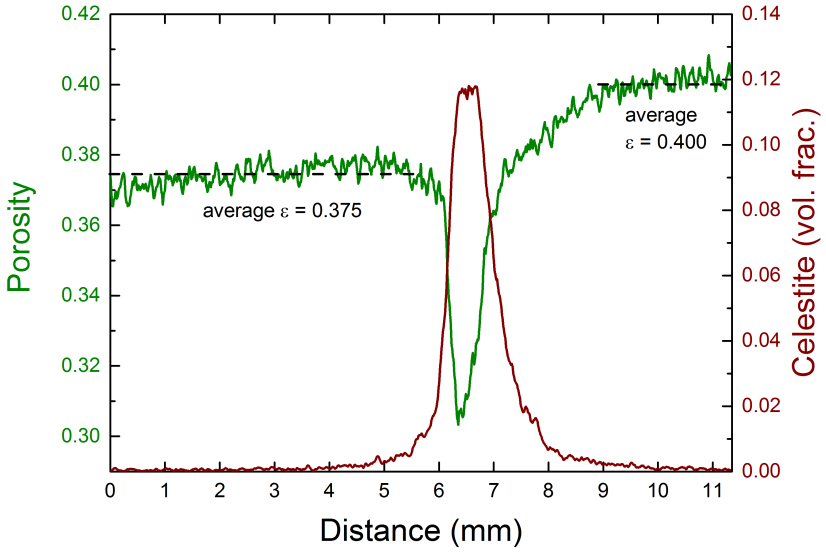

Figure 6.7: Porosity and volume fraction of precipitate along the μCT measured profile of sample CTprec1 from voxel-counting.

with the steady-state HTO through diffusion observed after the formation of the precipitation front. The minimum porosity reached in this front estimated by VCA was 0.31 $\pm$ 0.03. This value is in good agreement with the value found for the low resolution data set (0.28 $\pm$ 0.03). The small increase in porosity before and after the precipitation front observed on the porosity profile suggest a variability in the compaction of the sand, as observed for the undisturbed sand columns measured with μCT (see section 5.2.3 and fig. 5.6).

Transport parameters quantification under high resolution

The segmented 3D volume with 3 labels (pore space, sand grains and precipitate) was implemented in the pore-morphology model to quantify the transport parameters in the undisturbed material and in the precipitation zone. Different Regions of Interest (ROIs) were selected from the complete data set (fig. 6.8): (1) a cylinder cut-out from the center of the volume (ROI-all), ex-

cluding the borders to avoid rim effects, (2) three cubes of the same dimensions (3.6 mm side length) at different positions in the volume, two in the undisturbed material above (ROI-top) and below (ROI-bottom) the precipitation zone, and one in the precipitation zone (ROI-middle), and (3) a disk cut-out from the center of the volume (ROI-disk), and including the precipitation zone.

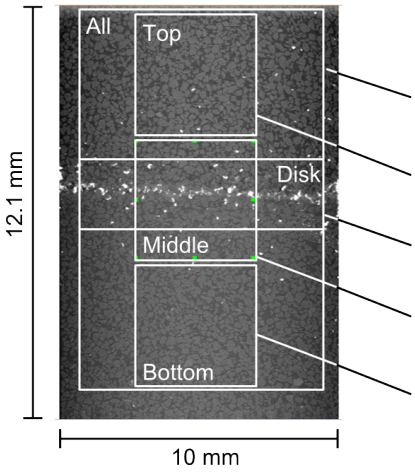

	Porosity	Diffusivity (10^{-10} m²/s)			Tortuosity		
		X	Y	Z	X	Y	Z
All	0.38						
Disk	0.41	5.00	5.05	5.03	1.83	1.82	1.83
Middle	0.35						
Top	0.37	4.09	4.16	2.39	2.04	2.00	3.49
Bottom	0.40	5.01	5.05	5.03	1.83	1.82	1.83

Figure 6.8: Schematic representation of the location of the different ROIs selected from the high resolution CT data set, and transport parameters calculated with the pore morphology model for each ROI.

As expected, the pore space geometry of the undisturbed material was found homogeneous in all three dimensions. The average porosity in the 3 Cartesian directions of the undisturbed porous material was calculated for ROI-top and ROI-bottom. The total porosity was 0.41 ± 0.01, with no isolated pores detected. This value is in good agreement with the HTO diffusion experiments (0.42 ± 0.09), the MIP (0.42 ± 0.02), the μCT calculations on the reference diffusion cells (0.40 ± 0.03) and the VCA on the low (0.44 ± 0.05) and high (0.39 ± 0.03) resolution data sets.

The average effective diffusivity in the 3 Cartesian directions was $(5.03 \pm 0.02)\times10^{-10}$ m$^2\cdot$ s^{-1} for the ROI-top and ROI-

bottom. This value is in good agreement with the HTO tracing experiments ($(4.48 \pm 0.17) \times 10^{-10}$ $m^2 \cdot s^{-1}$). The average tortuosity factor of the undisturbed material in the 3 Cartesian directions was calculated for ROI-top and ROI-bottom using the ratio of the pore-morphology model derived porosity and effective diffusivity. It was 1.83 ± 0.02, which is in good agreement with the geometric factor calculated based on HTO through diffusion (1.92 ± 0.44).

In the precipitation zone, the porosity calculated is only slightly smaller, as it is an average of the whole ROI-middle, which includes parts of the undisturbed material. However, the tortuosity increases and the diffusivity decreases significantly. No isolated pores were found by the model, suggesting that the remaining porosity in the precipitation zone was fully connected.

The influence of the increase in tortuosity and decrease in porosity in the precipitation zone on the transport of dissolved species can be better understood from the Laplace field calculations (Becker et al., 2011; Wiegmann and Becker, 2012) performed in the middle and bottom ROIs (fig. 6.9). The simulation was performed in all 3 Cartesian directions for both ROI-middle and ROI-bottom. The field is very homogeneous in the X, Y and Z directions for the bottom ROI, as expected for a homogeneous, undisturbed porous material. It is also homogeneous in the X and Y directions for the middle ROI, but is strongly influenced by the precipitation zone in the Z direction, the direction of diffusion from the Sr to the SO_4-reservoir.

The geometrical pore size distribution is very similar for all ROIs (fig. 6.10). A similar calculation was made for the celestite grain size distribution. The distribution curve is the same as for the pores of the material, indicating that the material fills the pore space. This observation confirms the microscopic observation of the precipitate made with SEM. The small shift towards bigger diameters indicates a possible preference of the precip-

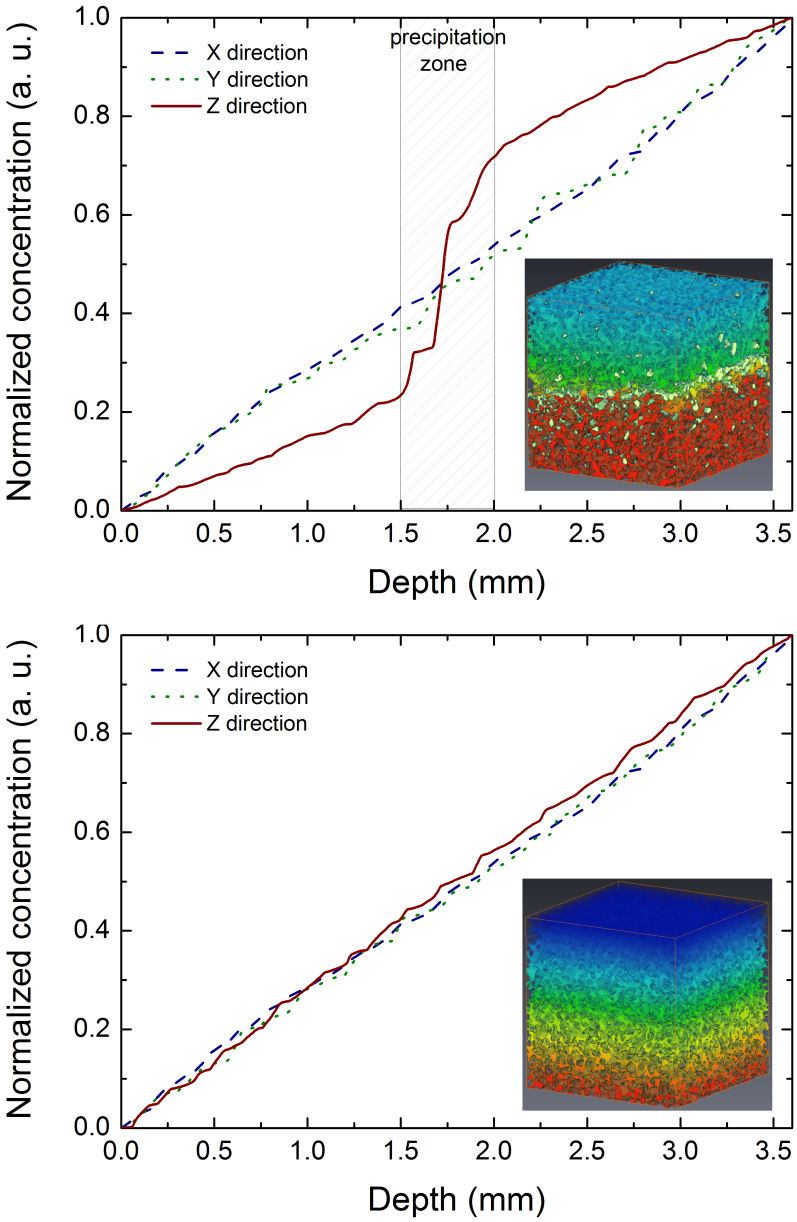

Figure 6.9: Laplace field simulations on ROI middle (including the precipitation front) and ROI bottom (undisturbed material). On the bottom left corners of the graphs are the 3D renderings of the calculations. The red to blue color gradient represents the high to low particle concentration gradient.

itate for the biggest pores. Emmanuel and Ague (2009) have shown through theory and modeling that in systems with small pores, the SI of a precipitating phase was pore size dependant. It has also been shown on the μCT images that the precipitates are mostly localized in pores and not in pore throats.

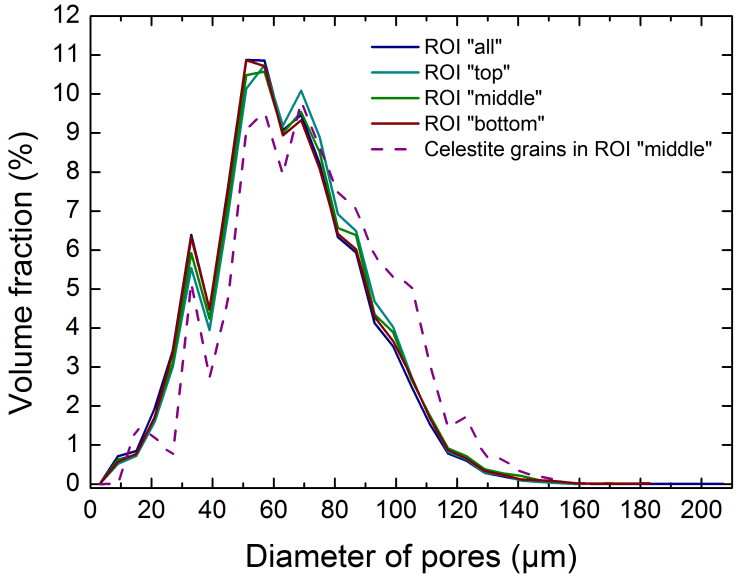

Figure 6.10: Pore and celestite grain size distributions for different ROIs.

6.2 The compacted illite-du-Puy

The *post-mortem* analysis of compacted illite-du-Puy consisted of autoradiographic measurements of 4 polished surfaces of the ^{14}C-PMMA impregnated IdP1 sample. The autoradiography allowed the estimation of the average accessible porosity of selected areas and transects.

6.2.1 Through diffusion of tracers

HTO and ^{36}Cl diffusion breakthrough curves (fig. 6.11) in the absence of celestite precipitation show lower diffusion fluxes for

^{36}Cl than for HTO (after renormalization to their respective self-diffusion coefficient in water). This behavior has been repeatedly reported for diffusion in charged clay materials (e.g., Glaus et al., 2010) and is related to the semi-permeable membrane properties of those materials and the partial exclusion of anions. As discussed earlier, the anion exclusion phenomenon is due to the high and permanent surface charge of the clay particles, forming a negatively charged water layer at their contact. Due to their own negative charge, anions cannot enter this water layer, and are thus excluded form part of the pore water.

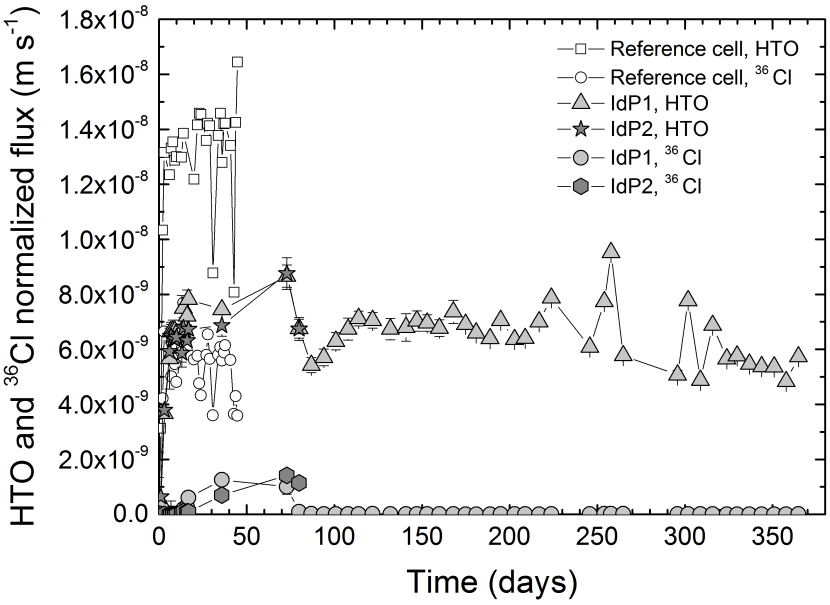

Figure 6.11: HTO and ^{36}Cl through diffusion fluxes in compacted illite-du-Puy, prior to (open symbols) and during (full symbols) porosity reduction by celestite precipitation.

The precipitation of celestite in the porosity of illite had a marked effect on the HTO diffusion flux, decreasing it by a factor two. The two samples that were investigated exhibit very consistent behaviors. This drop in the diffusive flux is due to the decrease of the porosity and also potentially to a resulting more tortuous pathway for HTO diffusion. At day 70-80, a further

drop in the HTO diffusivity is apparent. This second stage is not a measurement artifact as evidenced by its excellent reproducibility. This decrease in diffusivity must then correspond to a change in the structure of the connected porosity.

The ^{36}Cl diffusion data gives further insights: by day 70, ^{36}Cl diffusion flux was reduced by a factor four as compared to the reference sample. Since ^{36}Cl diffusion is more affected than is HTO diffusion, it can be concluded that the precipitation of celestite must take place in the pore fraction where most of ^{36}Cl diffusion occurs. Based on recent studies, it seems reasonable that mineral precipitation occurs preferentially in the largest pores (Putnis et al., 1995; Stack et al., 2014). The largest pores are also those where the least anion exclusion takes place and thus are the most favorable for anion diffusion (Tournassat and Appelo, 2011). Consequently, by blocking a large part of ^{36}Cl diffusion pathway in this pore fraction, celestite precipitation decreases more dramatically the ^{36}Cl diffusion flux than it does the HTO diffusion flux. At day 70, a precipitous decrease in the ^{36}Cl diffusion flux is evident. It corresponds exactly to the drop in HTO flux. However, in contrast to the HTO flux, ^{36}Cl diffusive flux dropped to zero: the precipitation of celestite has completely disrupted the connectivity of ^{36}Cl diffusion pathway. Since HTO can still diffuse through the system, the present result means that a non-negligible part of the porosity is impermeable to ^{36}Cl diffusion. A conceptual view of this phenomenon is illustrated in fig. 6.12.

Based on the experimental results alone, it is neither possible to quantify unambiguously the volume of this part of the porosity nor the minimum size of the pores leading to total anion exclusion. Still, the present result can be put in perspective with molecular dynamics simulation results (Rotenberg et al., 2007). According to those simulations, a pore with two layers of water ($\approx$ 6 Å) between two negatively charged clay surfaces

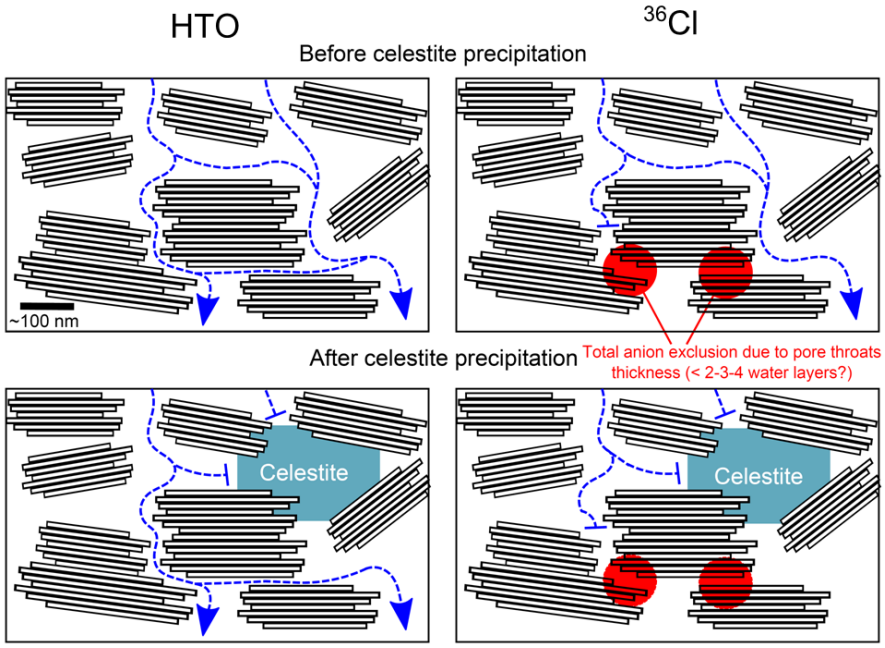

Figure 6.12: Conceptual view of how HTO and ^{36}Cl through diffusion is affected by celestite precipitation.

should not be accessible to anions. The work of Malusis et al. (2012) has theoretically proven that compacted clays have semi-permeable membrane properties, but stated that the experimental work needed to certify the theory was missing. VanLoon et al. (2007) and Garcia-Gutierrez et al. (2004) measured anions through diffusion in highly compacted clays, but continued to observe anions diffusion through the material even at very high compaction states (1900 Kg·m^{-3}). The present study gives the first clear experimental evidence for this ideal membrane property of clay (infra)nanopores.

6.2.2 Porosity evolution

The through diffusion of the stock solutions in the compacted illite-du-Puy sample IdP2 was stopped at 80 days of run, and a μCT scan was performed 19 days later at a relatively low

resolution (27.2 μm). A 3D view of the precipitation front is reported on fig. 6.13. The precipitation front has the shape of a half-disk, which radius spreads from the center of one filter to the middle of the diffusion cell wall. This shape is very different from the disk-shaped precipitation fronts observed in the sand system, where the disks were perpendicular to the direction of diffusion. The precipitation front could not be investigated in more details by μCT, as the resolution was too low to resolve the pores ($\leq$ 1 μm for various compacted clays, including illitic clays, e.g.; Vasseur et al. (1995); Djeran-Maigre et al. (1998)). However, it was a helpful measurement to select the surfaces that would later be used in autoradiography measurements.

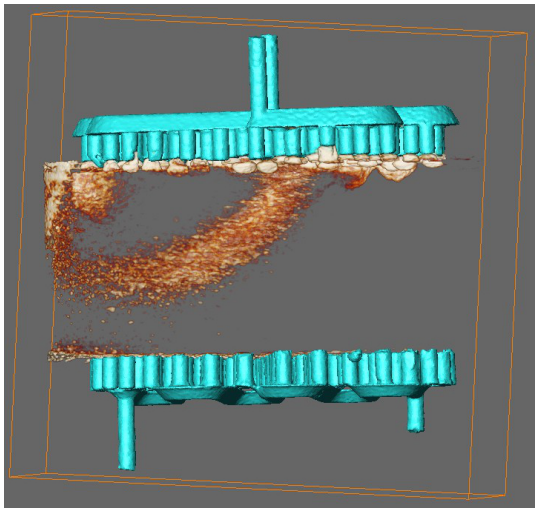

Figure 6.13: 3D reconstitution of the precipitation front (orange) in the compacted illite sample IdP2, from a 27.2 μm resolution CT scan.

The average accessible porosity was measured for each polished surfaces by autoradiography, on several selected areas of various dimensions (fig. 6.14). Some areas contained both the undisturbed zone and parts of the precipitation front, while others were positioned exclusively either in the undisturbed material or in the precipitation front. The estimated average accessible porosity values are reported in table 6.2.

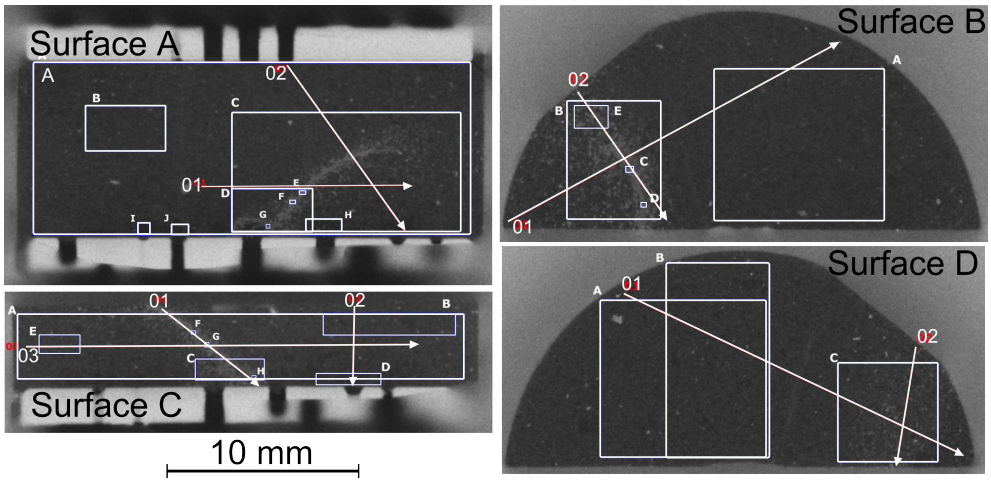

Figure 6.14: Autoradiographs of the surfaces A to D of the sample IdP2. The lighter the grey value, the lower the porosity. Areas of measurements and transects are marked by boxes and lines, respectively.

The average porosity is of 0.529 and 0.294 in the undisturbed material and in the precipitation front, respectively. The average accessible porosity of the material is reduced by a factor 1.8 in the precipitation front. The tracers through diffusion evidenced that the precipitation affected the free-water porosity, leaving the anion-exclusion porosity open and connected. When deducing the porosity value of 0.294 in the precipitation zone from the porosity value in the undisturbed zone, a value of 0.235 is obtained. This is in good agreement with published values for anion accessible porosity (0.18 $\pm$ 0.05, Glaus et al. (2010) and 0.25 $\pm$ 0.08, Tomas Kupcick, unpublished work). Therefore, from the autoradiography results, one can conclude that the anion-exclusion porosity is about half the total connected porosity, as would be expected for this material in these conditions.

The relatively high values of average connected porosity in surface A, areas I and J and in surface C, area D, show an heterogeneity in the porosity distribution through the material, as evidenced by the porosity profiles (fig. 6.15). The porosity sig-

Table 6.2: Average accessible porosities (ε_a) calculated from the autoradiographs for each selected areas of the surfaces A to D of sample IdP2.

Surface	Area	ε_a	Surface	Area	ε_a
A	A	0.485	B	A	0.492
A	B	0.499	B	B	0.410
A	C	0.466	B	C	0.270
A	D	0.448	B	D	0.278
A	E	0.268	B	E	0.382
A	F	0.277	C	A	0.504
A	G	0.320	C	B	0.506
A	H	0.575	C	C	0.427
A	I	0.617	C	D	0.583
A	J	0.582	C	E	0.500
D	A	0.492	C	F	0.288
D	B	0.490	C	G	0.304
D	C	0.452	C	H	0.343

nificantly increases from one filter to the other (in the direction parallel to the direction of diffusion), and is very homogeneous in the direction perpendicular to the diffusion. These higher porosity values in the neighboring region of one of the filter could be due to the compaction method. The illite-du-Puy powder was introduced in the half-closed diffusion cell and compressed from the top with a piston, and the diffusion cell was then closed. It would be reasonable to assume that in such conditions, the material at the bottom of the diffusion cell would be more compacted than the one on the top, which would result in porosity gradients such as the one observed for the sample IdP2. However, such a hypothesis should be tested by measuring a freshly compacted material which was not yet used in any diffusion experiments. In addition, illite is known to have a small swelling pressure, mostly due to the presence of small amounts of il-

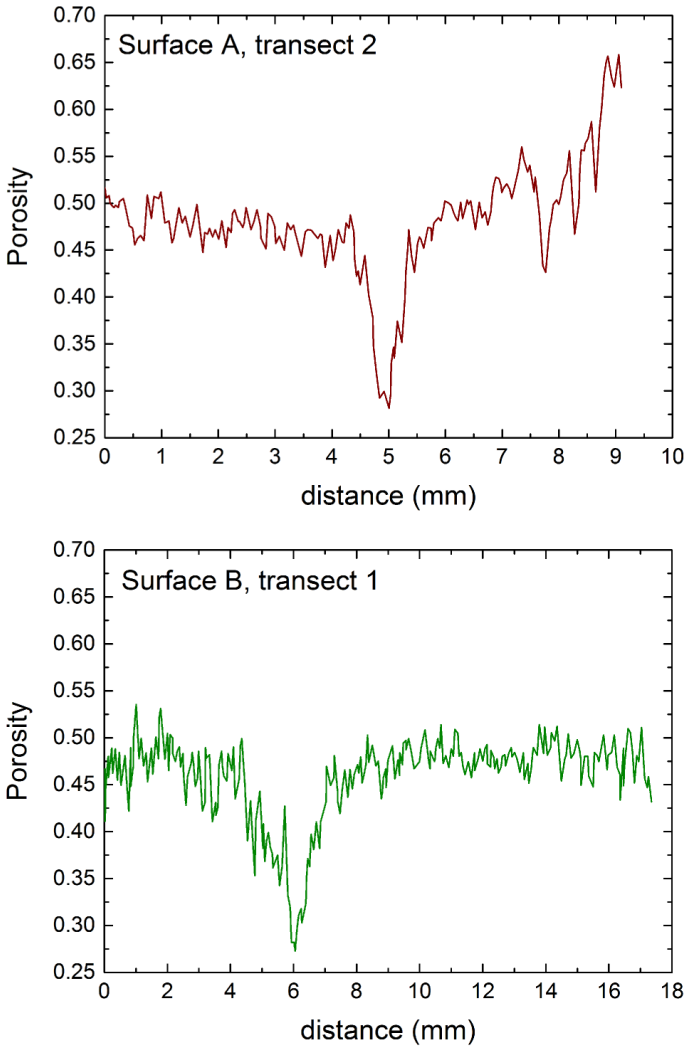

Figure 6.15: Porosity profile along transect 2 of surface A (parallel to direction of diffusion) and 1 of surface B (perpendicular to direction of diffusion).

lite/smectite mixed layers (Fialips and Robinet, 2011). It could possibly swell in the filter supports holes. It should happen on both sides of the diffusion cells, unless the compaction method limits the swelling in the lower part by partly filling the holes.

A SEM analysis of the surface A showed that the precipitate was stoechiometric celestite in the form of aggregates of

sizes ranging between 20 and 160 μm. Those aggregates fill the macropores of the compacted illite, as suggested by the tracers through diffusion results. While most of the celestite could be found within the compacted clay, a few aggregates were present in the holes of the filter from which the precipitation spreads.

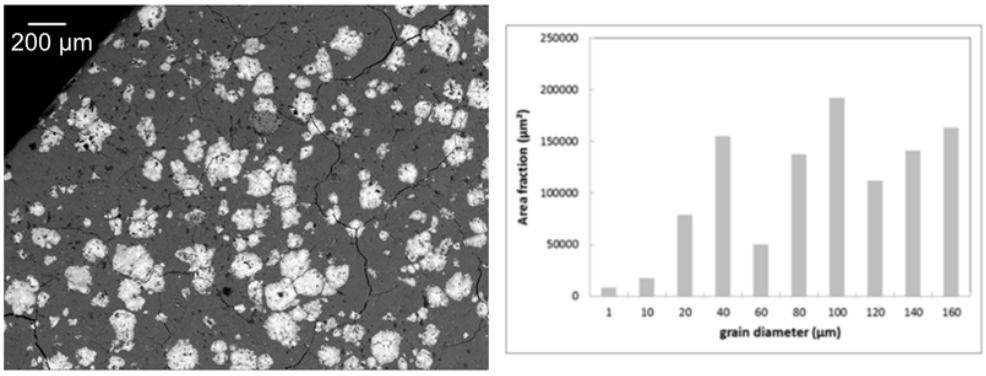

Figure 6.16: SEM image of celesite aggregates within the pore space of compacted illite-du-Puy (left) and grain size distribution (right).

Chapter 7

Reactive transport modeling

An extensive sensitivity analysis of the models was conducted and is presented as supplementary material in appendix B. The results obtained with the simple 1D models were found to be independent of the mesh size during the sensitivity analysis. However, this was not the case for the precipitation models. A dependence on the mesh size was also reported by Marty et al. (2009). Therefore, to keep all models comparable and consistent, a mesh size of 0.1 mm in X and Y directions was set for all runs.

As mentioned earlier (section 4.1.1), the model runs were conducted with the Debye-Hückel formalism, which applicability at high ionic strength is limited. We attempted to recalculate the activity coefficients, γ, from a Pitzer fitting procedure. However, the main ions activities (Sr^{2+}, SO_4^{2-}, Ca^{2+} and CO_3^{2-}) calculated with Pitzer in conditions similar to the experiments could not be fitted with corrected Debye-Hückel coefficients. Therefore, the models presented and discussed thereafter were all run with the classical Debye-Hückel formalism.

7.1 Tracers through diffusion

The filter sets might have a significant effect on the transport parameters of the porous materials estimated by the linear re-

gression method. A simple and effective way to characterize and quantify filter effects is to use a model that takes into account the geometry (2D) and/or transport parameters (1D and 2D) of the filter sets. If the models do not fit the experimental data, it means that there are some filter effects, and therefore the transport parameters of the porous material must be changed until a good agreement between the model and the data is reached. For both the sand and the clay system, the filter sets used consisted of pierced disk of impermeable material (Plexiglas for sand, PEEK for illite). The plates were about 2 to 3 mm thick, and contained several straight cylindrical holes of 1 mm diameter (fig. 2.2). Their porosity was of 0.370 in the case of the sand system, and 0.146 in the case of the clay system.

7.1.1 The purified sea sand

The diffusion cells used for the sand system were build around a 10 mm diameter 50 mm long cylinder (or column) containing the compacted material. Filter sets were fixed at each ends of these columns. The filter sets were either 1 filter support (2 mm thick) and a membrane filter (diffusion cells S1 and S2), or a nylon gaze sandwiched between 2 filter supports, for a total thickness of 5 mm (all other diffusion cells). It is expected that the filter effects should be insignificant or small, as the porosity of the filter supports (0.370) is very close to that of the sand (0.40 - 0.42) and their thickness is much smaller than that of the porous material (7 to 17% of total length).

HTO through diffusion in 1D

First, the data of all experiments performed were fitted with a 1D model. The 1D model included the filter supports characteristics, with a porosity of 0.370 and a tortuosity factor of 1.00 (straight cylindrical pores). Two parameters can be varied to fit

the experimental data: the porosity and the tortuosity factor of the sand. As can be seen from the results of the tracing experiments (table 5.4) and μCT analysis (table 5.5), the porosity of the samples varies over a relatively wide range. Therefore, and as was previously discussed, one can suppose that the methods used to estimate the porosity (linear regression and 3D images analysis) are slightly biased. As an additional measurement of the porosity, the mass of the sand recovered from the diffusion cells CT-prec1, S3-CEL, S13-CEL°, S14-CEL° and S8-CAL for the *post-mortem* analysis was measured, and the porosity was back-calculated. The average porosity was 0.408 ± 0.028. It was decided that the porosity of all the diffusion cells would be varied within these limits for the modeling, and that the experimental data would be fitted by varying the tortuosity factor. The results are reported in table 7.1.

Effects of porosity spatial variability

The CT scans revealed a heterogeneous porosity distribution within the sand columns (see section 5.2.3 and figure 5.6), with variations of ± 0.025, and up to ± 0.050. The effects of such variations on HTO through diffusion were tested with a 1D model. The porosity in the model was varied within the limits set for the fitting procedure: 0.408 ± 0.028. A porosity variation of ± 0.028 is reasonable, and compares well with the μCT observations. The experiment S6-HTO1 was used for the test. The porosity of the first 12 mm of the sand column was 0.380 (0.408-0.028), followed by 13 mm at $\varepsilon = 0.436$ (0.408+0.028), then by 13 mm at $\varepsilon = 0.380$ and again 12 mm at $\varepsilon = 0.436$, for a total of 50 mm and an average porosity of 0.408.

First, the tortuosity of the material was the value corresponding to $\varepsilon = 0.408$ ($\tau = 0.436$). The difference with the homogeneous porosity distribution model was insignificant: the flux at

Table 7.1: Effective diffusivity (D_e, in $\times 10^{-10}$ $m^2 \cdot s^{-1}$), geometric factor (G), tortuosity (τ) and cementation factor (m) obtained by fitting the HTO through diffusion data of 10 samples of compacted sand, with a 1D model. Accessible porosity was 0.408 ± 0.028.

Experiment	D_e HTO	G $\approx \tau_f^2$	$1/G = \tau$	m
S1-HTO1	3.60 ± 0.18	2.54 ± 0.29	0.396 ± 0.045	2.04 ± 0.21
S1-HTO2	4.13 ± 0.21	2.21 ± 0.25	0.455 ± 0.052	1.89 ± 0.19
S1-HTO3	4.00 ± 0.20	2.28 ± 0.26	0.441 ± 0.050	1.92 ± 0.20
S2-HTO1	4.00 ± 0.21	2.28 ± 0.26	0.440 ± 0.050	1.92 ± 0.20
S2-HTO2	4.08 ± 0.21	2.24 ± 0.26	0.449 ± 0.051	1.90 ± 0.19
S2-HTO3	4.13 ± 0.21	2.21 ± 0.25	0.454 ± 0.052	1.89 ± 0.19
S2-HTO4	3.84 ± 0.20	2.38 ± 0.27	0.442 ± 0.048	1.97 ± 0.20
S3-HTO1	3.51 ± 0.19	2.49 ± 0.51	0.408 ± 0.068	2.02 ± 0.31
S3-HTO2	4.08 ± 0.22	2.24 ± 0.26	0.449 ± 0.053	1.90 ± 0.20
S4-HTO1	4.04 ± 0.21	2.26 ± 0.26	0.445 ± 0.052	1.91 ± 0.20
S5-HTO1	3.96 ± 0.21	2.31 ± 0.27	0.435 ± 0.051	1.94 ± 0.20
S6-HTO1	3.97 ± 0.22	2.30 ± 0.27	0.437 ± 0.052	1.93 ± 0.20
S7-HTO1	4.05 ± 0.21	2.25 ± 0.26	0.446 ± 0.052	1.91 ± 0.20
S8-HTO1	4.12 ± 0.22	2.22 ± 0.26	0.454 ± 0.053	1.89 ± 0.20
S9-HTO1	4.04 ± 0.22	2.26 ± 0.26	0.445 ± 0.052	1.91 ± 0.20
S10-HTO1	4.01 ± 0.22	2.28 ± 0.27	0.441 ± 0.052	1.92 ± 0.20
Average	3.97 ± 0.46	2.30 ± 0.24	0.440 ± 0.044	1.93 ± 0.11

steady state was only 0.3% smaller. When a heterogeneous distribution of τ was implemented - with the value corresponding to each porosity (0.485 for $\varepsilon = 0.380$ and 0.423 for $\varepsilon = 0.436$) - the difference between the two models was further reduced to 0.03%. The results discussed here are not shown on graphs, as a visual distinction between all curves could hardly be made.

One can conclude that a heterogeneous porosity distribution of the present order (± 0.028) has no significant influence on the outcome of the models. Therefore, it is not necessary to take it into account, which simplifies the modeling procedure.

HTO through diffusion in 2D

The same fitting procedure was followed with a 2D model that included a realistic geometry of the filter supports. The geometry of the filter supports, an impermeable plate pierced by straight cylindrical holes, was reproduced by alternating, in the Y direction, 10 cells with a porosity of 1×10^{-14}, 11 cells with a porosity of 1.000 and again 9 cells with a porosity of 1×10^{-14}. The very low value of 1×10^{-14} was chosen because the model does not compute with a value of 0.000. The number of cells is unequal, to have a total porosity of the supports of 0.370. The results of the fitting procedure are reported in table 7.2. The results obtained are only slightly different from those obtained with the 1D modeling, with an average difference in the D_e of about $+0.10\times10^{-10}$ $m^2\cdot s^{-1}$ (+2.5%). For all other parameters, the difference is about 2.5 times bigger for the 2×5 mm thick supports than for the 2×2 mm thick filter supports systems, though still insignificant. The filter supports have an insignificant impact on the through diffusion of the tracer through the sand.

7.1.2 The illite-du-Puy

The simple through diffusion of HTO and ^{36}Cl in illite-du-Puy was also modeled with a 1D and 2D model, however in a slightly different manner. The experimental data available were scarce (only one for each tracer) and were obtained on a different sample than those used in the precipitation experiments. An attempt was made to model these data with the values of poros-

Table 7.2: Effective diffusivity (D_e, in $\times 10^{-10}$ $m^2 \cdot s^{-1}$), geometric factor (G), tortuosity (τ) and cementation factor (m) obtained by fitting the HTO through diffusion data of 10 samples of compacted sand, with a 2D model. Accessible porosity was 0.408 ± 0.028.

Experiment	D_e HTO	G $\approx \tau_f^2$	$1/G = \tau$	m
S1-HTO1	3.69 ± 0.19	2.51 ± 0.33	0.400 ± 0.040	2.03 ± 0.22
S1-HTO2	4.23 ± 0.22	2.19 ± 0.28	0.460 ± 0.047	1.88 ± 0.21
S1-HTO3	4.11 ± 0.21	2.26 ± 0.29	0.446 ± 0.046	1.91 ± 0.21
S2-HTO1	4.10 ± 0.21	2.26 ± 0.29	0.445 ± 0.045	1.91 ± 0.21
S2-HTO2	4.18 ± 0.22	2.21 ± 0.28	0.454 ± 0.046	1.89 ± 0.21
S2-HTO3	4.23 ± 0.22	2.19 ± 0.28	0.459 ± 0.047	1.88 ± 0.21
S2-HTO4	3.94 ± 0.20	2.35 ± 0.30	0.427 ± 0.043	1.96 ± 0.22
S3-HTO1	3.60 ± 0.19	2.54 ± 0.30	0.396 ± 0.047	2.04 ± 0.21
S3-HTO2	4.18 ± 0.22	2.18 ± 0.25	0.461 ± 0.054	1.87 ± 0.19
S4-HTO1	4.14 ± 0.21	2.20 ± 0.25	0.456 ± 0.053	1.88 ± 0.19
S5-HTO1	4.06 ± 0.22	2.25 ± 0.26	0.447 ± 0.052	1.91 ± 0.20
S6-HTO1	4.07 ± 0.22	2.24 ± 0.26	0.449 ± 0.052	1.90 ± 0.20
S7-HTO1	4.16 ± 0.22	2.19 ± 0.25	0.458 ± 0.053	1.88 ± 0.19
S8-HTO1	4.22 ± 0.23	2.16 ± 0.25	0.465 ± 0.054	1.86 ± 0.19
S9-HTO1	4.15 ± 0.22	2.20 ± 0.25	0.457 ± 0.053	1.88 ± 0.19
S10-HTO1	4.11 ± 0.22	2.22 ± 0.26	0.453 ± 0.053	1.89 ± 0.20
Average	4.07 ± 0.47	2.26 ± 0.28	0.446 ± 0.050	1.91 ± 0.13

ity available in the literature (for HTO: 0.42 ± 0.11, Van Laer et al. (2014); 0.60 ± 0.21, Glaus et al. (2012) and 0.43 ± 0.09, Tomas Kupcik, personal communication). In the model, the HTO accessible porosity of the material was varied within the 0.400-0.600 range, and the ^{36}Cl accessible porosity was set to half the value of the HTO accessible porosity (0.250 ± 0.050).

As for the sand, the data were fitted by varying the tortuosity of the porous material. The thickness of the clay pellet was set to 10 mm, although it was measured to be 9.44 mm for sample IdP2 during the post-mortem analysis. For the 2D model, the geometry and porosity of the filter supports were reproduced by alternating, in the Y direction, 29 cells with a porosity of 1×10^{-14}, 10 cells with a porosity of 1.000 and again 29 cells with a porosity of 1×10^{-14}. The results are reported in table 7.3.

Table 7.3: Effective diffusivity (D_e, in $\times10^{-10}$ m^2s^{-1}), geometric factor (G), tortuosity (τ) and cementation factor (m) obtained by fitting the HTO and ^{36}Cl through diffusion data of a sample of compacted illite-du-Puy, with an accessible porosity of 0.500 ± 0.100 for HTO and 0.250 ± 0.050 for ^{36}Cl.

Experiment	D_e	G $\approx \tau_f^2$	$1/G = \tau$	m
HTO, 1D	1.72 ± 0.16	6.53 ± 1.73	0.158 ± 0.041	3.84 ± 1.13
HTO, 2D	2.86 ± 0.16	3.93 ± 1.05	0.263 ± 0.067	3.08 ± 0.93
^{36}Cl, 1D	0.70 ± 0.05	8.04 ± 2.10	0.129 ± 0.033	2.51 ± 0.41
^{36}Cl, 2D	1.09 ± 0.09	5.15 ± 1.32	0.200 ± 0.051	2.19 ± 0.36

The D_e values obtained with the 1D model are in good agreement with literature values (for HTO: $(1.8 \pm 0.3)\times10^{-10}$ m$^2\cdot$ s^{-1} (Van Laer et al., 2014) and $(2.1 \pm 0.2)\times10^{-10}$ m$^2\cdot$ s^{-1} (Glaus et al., 2012)), and depend very little on the porosity, as evidenced by the small error range. The literature data cited above were also obtained with a 1D transport model fitting. The effective diffusivity obtained with the 2D model are significantly higher than the ones obtained with the 1D model, for both HTO (1.7 times) and ^{36}Cl (1.6 times). The geometric factor is significantly lower, meaning that the path is less tortuous with a 2D model than with a 1D model. These results show the importance of taking into account the precise geometry of the filter

sets in the calculations, as their influence on the final results is great. It is more important for the illite-du-Puy than for the sand, as the porosity of the filter supports is much lower than that of the material in the former case, and the thickness of the filters sets in the illite system is more important (29% of the total length of the system).

7.2 Clogging of the porous materials

For the modeling of the sand and illite clogging, the precipitation of celestite was induced by adding $SrCl_2$ in one reservoir and Na_2SO_4 in the opposite reservoir. For the precipitation of calcite, $CaCl_2$ and Na_2CO_3 were added instead. The transport parameters determined by fitting the HTO through diffusion results for each experiments were used as initial parameters (tables 7.1 and 7.3), and the initial conditions (concentration of salts and pH) were the same as the corresponding experiments.

7.2.1 The purified sea sand

All the experiments that were carried out with porosity clogging were modeled in 1D. The experiments S13-CEL° and S14-CEL° were performed in freshly prepared diffusion cells, without any prior tracing. For these experiments, the average values of D_e, porosity and cementation exponent obtained by 1D model fitting were used (see table 7.1). For the experiments S3-CEL and S8-CAL°, the HTO tracing and the precipitation experiments were performed one right after the other, without out-diffusion and renewing of the pore solution. The models used reproduced the same conditions. For the experiments S1-CAL and S2-CAL, the initial transport parameters used were the average of all S1-HTO and S2-HTO runs. The models were not run in 2D, as it was previously shown that it has little effect on the outcome (section

7.1 and appendix B). Moreover, the 2D models are particularly long to run in reactive conditions (more than 10 hours for a 100 days calculation) and often encounter convergence issues due to the very high number of grid cells (16230 to 18030 grid cells), as seen during the sensitivity analysis (appendix B). The models were all run for a reaction time of 360 days. The results obtained are discussed thereafter, and compared to the experimental data on several aspects: (1) the minimum porosity, (2) the mass of precipitate and position of the precipitation front and (3) the HTO flux curves.

Minimum porosity

The minimum porosity of the sand after clogging was estimated at 0.30 ± 0.06 with μCT in the precipitation front of the diffusion cell CTprec1. As the experimental conditions for CTprec1 were the same as for S13-CEL° and S14-CEL°, the μCT value of minimum porosity (0.30) was entered in the model for these two experiments. The modeled HTO flux was largely overestimated (fig. 7.1). The best fit of the experimental data was obtained for a minimum porosity of 0.014.

Mass of precipitate and position of precipitation front

The experimental and modeled results are compared in table 7.4. The models were run for a minimum porosity of 0.014. The modeled position of the precipitation front is in good agreement with the experimental ones for CTprec1, S3-CEL and S8-CAL°. The front position of experiments S13-CEL° and S14-CEL° are much closer to the Sr-reservoir than for all other experiments. The model overestimated the mass of precipitate by a factor of 3.0 (S13-CEL°) up to 6.1 (S3-CEL). The longer the reaction time, the bigger the difference. This difference could be due to the bigger portion of the pore space available for precipitation

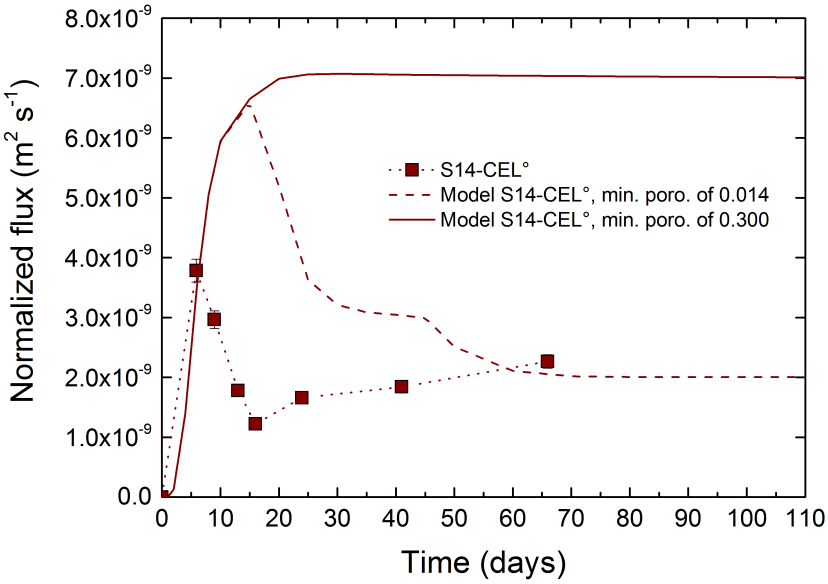

Figure 7.1: Experimental and modeled HTO fluxes obtained during porosity clogging by celestite and calcite precipitation.

Table 7.4: Experimental and modeled precipitated mass of celestite and calcite and position of the precipitation front. The front position is relative to the boundary between the sand column and the filter supports of the Sr-/Ca-reservoirs.

Experiment	Time	Front position (mm)		Mass of precipitate (mg)	
	days	Experimental	Modeled	Experimental	Modeled
CTprec1	29	21.0 ± 1.0	24.9 ± 0.2 [a]	21.7 ± 0.4	96.7 [a]
S3-CEL	67	26.0 ± 0.4	24.9 ± 0.2	15.6 ± 0.4	95.6
S13-CEL°	28	12.5 ± 2.5	24.9 ± 0.2	31.6 ± 0.5	93.4
S14-CEL°	66	17.5 ± 2.5	24.9 ± 0.2	35.6 ± 0.5	166.7
S8-CAL°	67	20.0 ± 0.5	22.4 ± 0.2	15.3 ± 0.4	81.9

[a] Estimated from the model used for S14-CEL° (identical conditions).

(0.408 - 0.014 = 0.394 for the model and 0.408 - 0.300 = 0.108 for the experiments). However, when using a minimum porosity of 0.300 in the model, the mass of precipitate at 66 days for experiment S14-CEL° was of 367.2 mg, a value 10.3 times higher

than the experimental one. This can be explained by a broader precipitation front ($\approx$ 1 mm for a minimum porosity of 0.300 against $\approx$ 0.3 mm for a minimum porosity of 0.014).

HTO flux curves

The modeled HTO fluxes are reported in fig. 7.2, and compared to the corresponding experimental data. Some general trends can be seen. The models almost always predict 2 successive drops in the HTO flux within the time of run (360 days), with the exception of the low concentration experiments (S4-CEL and S1-CAL, with 0.01 $mol \cdot L^{-1}$ stock solution, and S5-CEL, with 0.05 $mol \cdot L^{-1}$ stock solutions). The first drop, of about 50% of the highest flux value, corresponds to one of the grid cells reaching the minimum porosity value (0.014). The second drop, of about 35% of the average value reached after the first drop, corresponds to a second grid cell in the direct neighborhood of the first reaching the minimum porosity value. It can also be seen that the higher the stock solution concentration, the earlier the drops in flux are observed. Thus, one can easily imagine that if the models were run over a longer period, these two drops would also be observed for the lowest stock solution concentrations. For example, the first drop in the flux was observed for the S4-CEL model after 3000-4000 days of reaction time. Experimentally, only one drop in the HTO curve was observed throughout the duration of the experiments, the flux reaching a stable value about 38 to 96% lower than the highest value.

Another general trend that can be observed is that the model underestimates the flux (or overestimates the precipitation and its effects on the flux) for the lowest stock solution concentrations (0.01-0.05 $mol \cdot L^{-1}$ and 0.10 $mol \cdot L^{-1}$ for celestite), and overestimates the flux (or underestimated the effects of the pre-

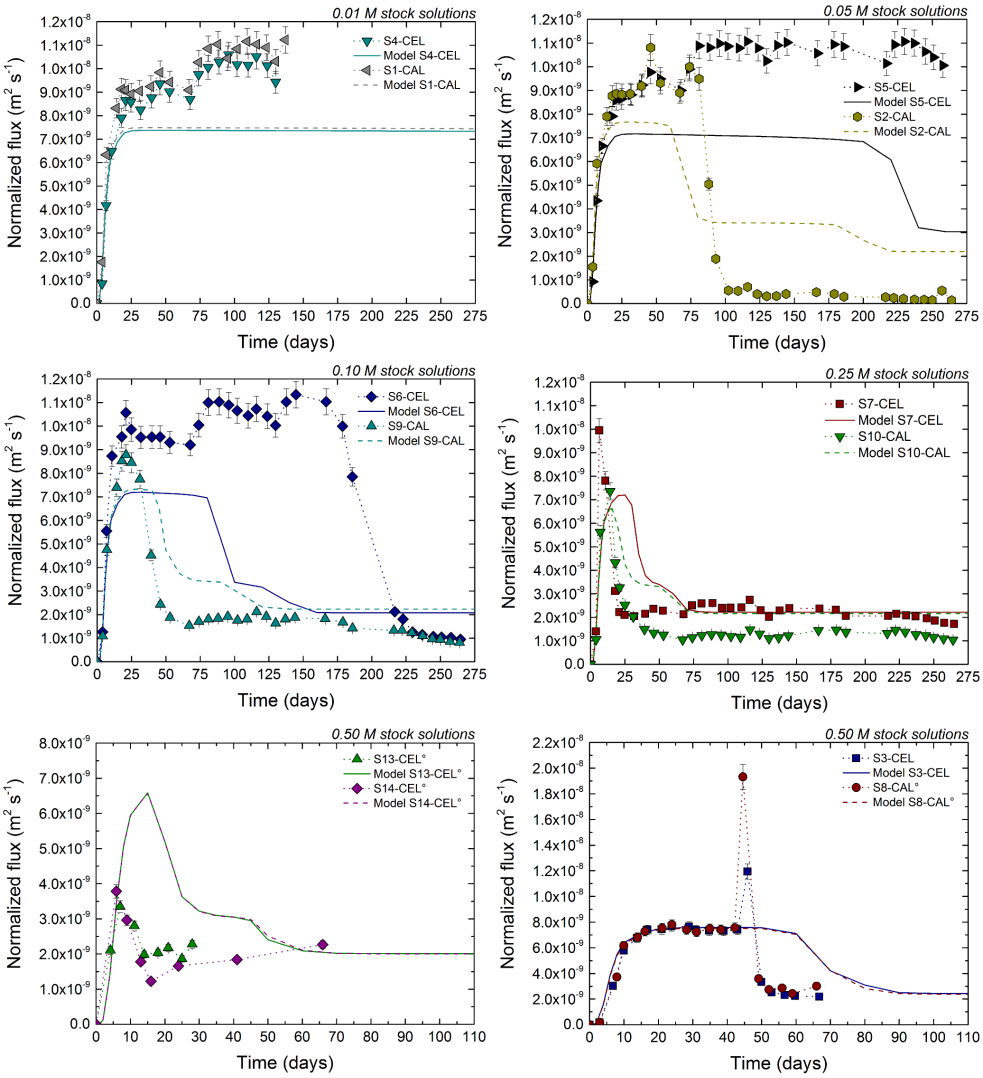

Figure 7.2: Experimental and modeled HTO fluxes obtained during porosity clogging by celestite and calcite precipitation.

cipitation on the flux) for the highest stock solution concentrations (0.10 mol $\cdot$ L^{-1} for calcite and 0.25-0.50 mol $\cdot$ L^{-1}). It also always over estimates the amount of precipitate for the highest concentrations, as seen earlier. A similar trend can be observed for the onset time of the first drop: it is overestimated for the lowest concentrations (comes earlier than observed) and underestimated for the highest ones.

The model also predicts a slower clogging with celestite than with calcite. This can be explained in terms of molar volume differences, as discussed earlier (section 6.1.1). The precipitation kinetics regime (kinetics or local equilibrium) has very little effect of the results, as shown by the sensitivity analysis study (appendix B). For low concentrations, the model predicts a flux drop significantly earlier than experimentally observed for the celestite precipitation. This demonstrates the important role of silicon in solution as an inhibitor, and the minor role of the molar volume (Pina and Tamayo (2012); Louis Temgoua, personal communication). Indeed, the model takes into account the later, but not the former. The inhibition effects of H_4SiO_4 seem to decrease with increasing concentrations, as the differences between celestite and calcite decrease with increasing concentration. A model that takes into account the inhibition processes should be developed in order to match the experimental results. For that purpose, the effect of silicon on the critical saturation index (degree of supersaturation needed to start precipitation) and induction time (time needed to start precipitation) should be precisely determined in similar experimental conditions (4.8 ppm silicon).

Effects of porosity spatial variability

The effects of a heterogeneous porosity distribution on HTO through diffusion were tested in precipitation conditions. The experiment S6-CEL was used for the test, and the model used in the precedent section for S6-HTO1 was adapted to these conditions. The results are reported in fig. 7.3. The model used for experiment S6-HTO1 had a porosity distribution $\Delta\varepsilon_1$: 12 mm at 0.380, 13 mm at 0.436, 13 mm at 0.380 and 12 mm at 0.436. This model, when used in precipitation conditions for S2-CEL, showed a delayed flux drop as compared to the homogeneous

porosity model. The drop was smoother, and occurred about 25 days later. This was due to the front forming in a zone with a porosity of 0.436, larger than for the homogeneous porosity model (0.408). Thus, the celestite took more time to clog the pore space.

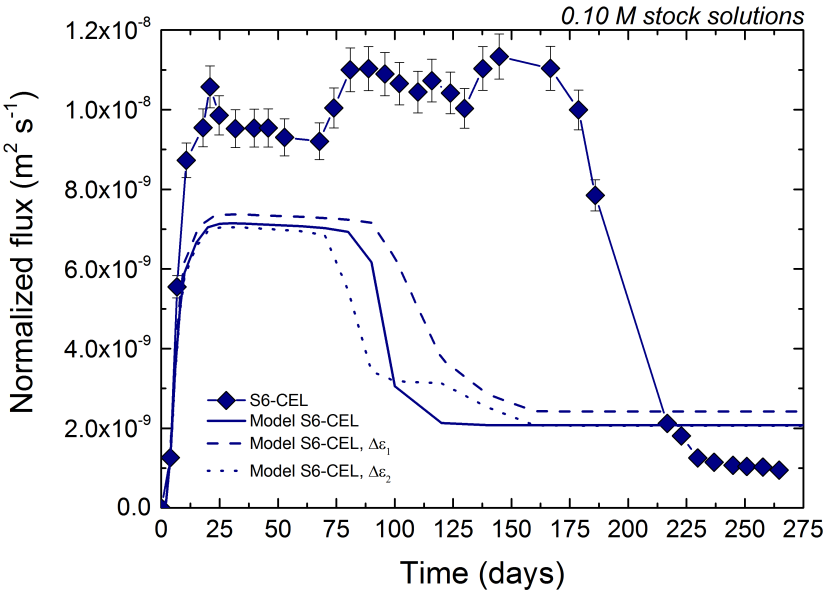

Figure 7.3: Experimental and modeled HTO fluxes obtained during porosity clogging by celestite in sample S6-CEL. The models were run for a homogeneous porosity ($\varepsilon = 0.408$, full line), and two heterogeneous porosity distributions (0.380/0.436/0.380/0.436, dashed line; 0.436/0.380/0.436/0.380, doted line).

When the porosity distribution was inverted ($\Delta\varepsilon_2$: 12 mm at 0.436, 13 mm at 0.380, 13 mm at 0.436 and 12 mm at 0.380), the precipitation occurred 25 days earlier compared to the homogeneous porosity model. These differences are significant for short time scale models. However, such porosity variations cannot be implemented in the models, as the porosity distribution would have to be measured for each sample separately prior to diffusion experiments. In addition, only one value of the cementation exponent can be entered in the model, and the tortuosity approach cannot be used in precipitation conditions (see appendix

B). This is a serious limitation in the present case, as a different cementation exponent should correspond to each different porosity. Describing a system with a spatial porosity variability with only one m is not sufficient.

Upper and lower limits

The models presented above were run for a porosity of 0.408, corresponding to the average porosity calculated from *post-mortem* analysis, with the corresponding cementation exponent for each diffusion cell. It was shown that the models tend to underestimate the initial HTO flux (before the drop) for low and average cations and anions concentrations, regardless of the clogging phase. To attempt finding a better agreement between models and experimental data, the model for S6-CEL was run for the upper and lower values of porosity (0.380 and 0.436) and cementation exponent (1.73 and 2.15). None of the models could satisfactorily reproduce the experimental data (fig. 7.4). The differences in the initial flux ($\approx$ 20 to 30 days) were only 10% between lowest and highest limits, and still 20 to 30% lower than the experimental flux.

To model the initial flux, it was necessary to add a small flow to the model (fig. 7.5). To test the effects of a flow, the model was first run without flow and without preciptiation. The HTO flux obtained was similar to the no-flow model discussed above, about 25% lower than the experimental flux. Then, a small flow was introduced in the model - still without precipitation - until the modeled HTO flux matched the experimental data. A flow of $(5.0 \pm 1.0) \times 10^{-9}$ m $\cdot$ s^{-1} matched best the experimental diffusion flux. Finally, the flow model was run for precipitation. The HTO diffusion flux drop was similar as for the no-flow model, and in the same order of magnitude. Overall, the flow-model greatly overestimates the steady state flux (after

the precipitation).

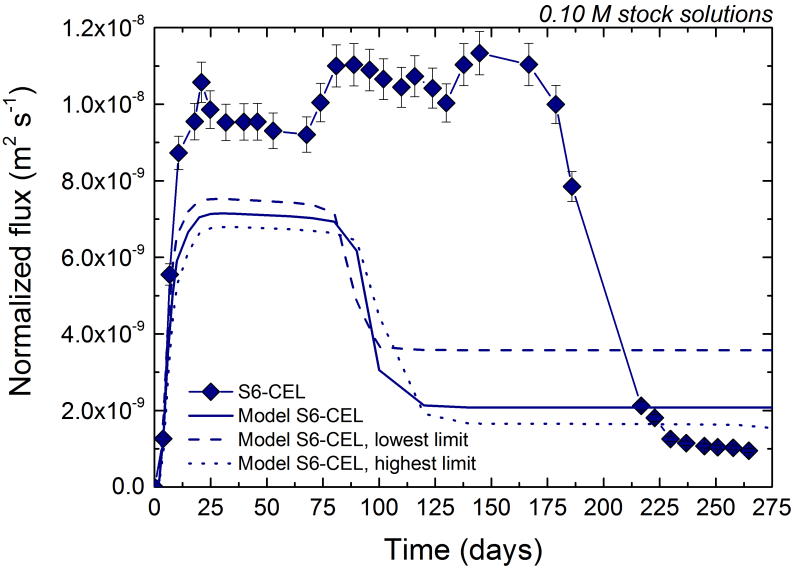

Figure 7.4: Experimental and modeled HTO fluxes obtained during porosity clogging by celestite in sample S6-CEL for average, lowest and highest values of porosity and cementation exponent.

The precipitation experiment could also not be satisfactorily reproduced by that model. A small flow present at the beginning of the experiments, which stopped when clogging started, could explain the high flux values. However, the presence of a flow in the experiments is highly unlikely, as the columns were well closed and kept horizontal. The high initial flux might be caused by fast through diffusion due to high concentration gradients in moderate to high saline conditions. These high experimental flux values were also observed for the continuous through diffusion experiments (S3-CEL and S8-CAL°, 7.2), when the NaCl reservoir solutions were exchanged for the Sr and SO4 bearing solutions. The reason behind such high fluxes is unknown, but might be related to the cations and anions bearing solutions (e.g.; differences in concentration and contents).

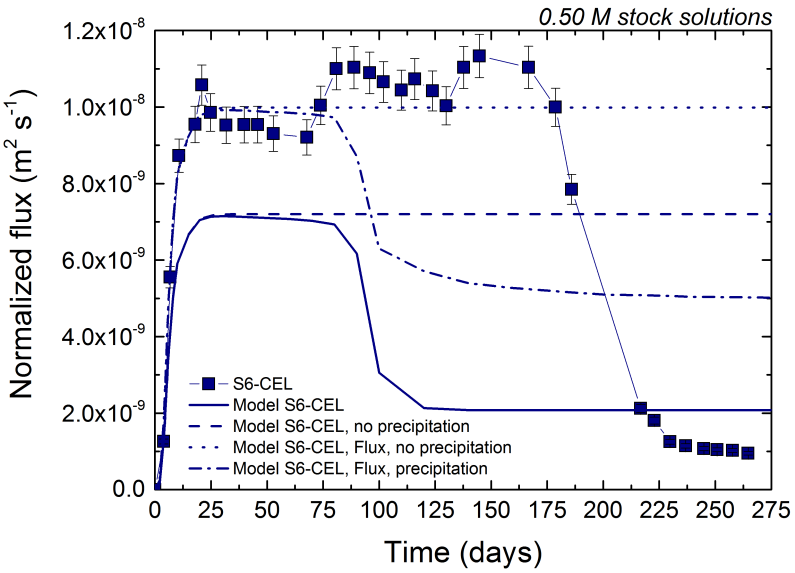

Figure 7.5: Experimental and modeled HTO fluxes obtained during porosity clogging by celestite in sample S6-CEL with and without flux ($(5.0 \pm 1.0) \times 10^{-9} m \cdot s^{-1}$) and with and without precipitation.

7.2.2 The illite-du-Puy

The porosity distribution in the model reproduced the real porosity distribution measured with autoradiography: the first 0.5 mm (in contact with Sr-reservoir filter supports) had a porosity of 0.600, the next 0.5 mm had a porosity of 0.550, and the rest of the material had a porosity of 0.500. The modeled HTO fluxes are compared to the experimental data in fig. 7.6. First, the model was run in 1D for a minimum porosity of 0.260, corresponding to the porosity measured in the precipitation front by autoradiography. This model overestimated the HTO flux by a factor 1.8. The experimental flux could be reproduced for a minimum porosity of 0.175 ± 0.015, a value lower than the experimental (0.260) and published values (0.18 ± 0.05, Glaus et al. (2010) and 0.25 ± 0.05, Tomas Kupcik, unpublished work).

As for the sand, the model does not reproduce the experiments. In additions to an over-simplification of the pore geome-

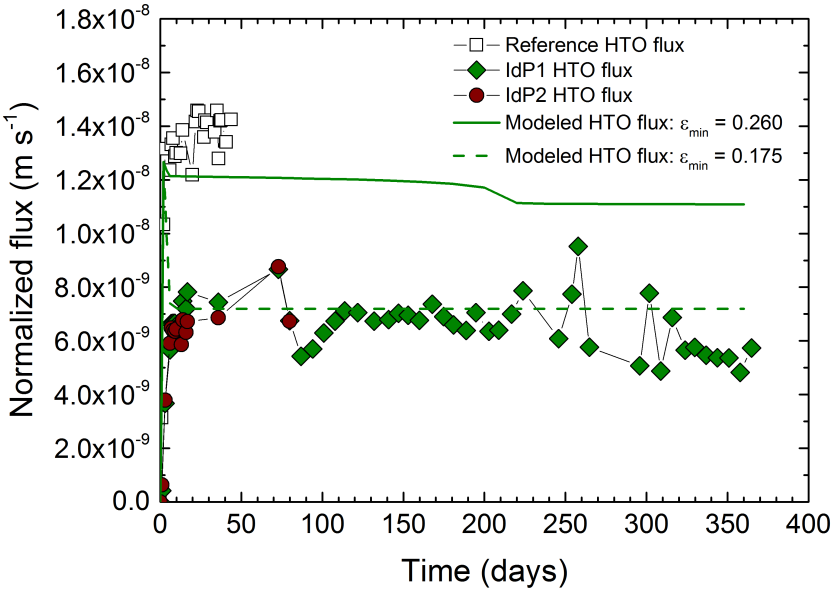

Figure 7.6: Experimental and modeled HTO fluxes obtained during porosity clogging by celestite precipitation in illite-du-Puy.

try - only one cementation exponent can be implemented in the model, even when several porosities co-exist - it does not take into account the dual porosity caused by surface charges and leading to anion exclusion. To better reproduce the experimental data, building a pore-scale model, as for the sand system, with in addition the presence of surface charges should be recommended. Such models are in development in the scientific community (e.g.; Alt-Epping et al., 2014).

Conclusion and Outlook

A complete experimental method allowing for the characterization of two porous materials with different characteristics and properties (sand and clay, both compacted in the laboratory) was successfully developed. This method consisted of diffusion experiments coupled to imaging techniques (μCT for the sand and autoradiography for the clay) from which the transport properties of the materials could be reliably determined, even during and after reduction of the pore space by controlled precipitation of a salt. The design of the diffusion cells itself made possible high quality μCT measurements of the sand. The transport properties determined for the two undisturbed porous materials compared well with published data, further confirming the reliability of the experimental approach chosen. It is believed that the approach developed within the present work is applicable to other types of materials (cores of natural materials, other compacted powders) and different geochemical conditions (advective flow, colloidal transport, dissolution), with only minor modifications to the cells design.

It could be shown that the empirical Archie's law and similar relationships are limited to accurately describe systems with an evolving porosity. Furthermore, the 1D/2D continuum reactive transport modeling approach showed many limitations in terms of precipitation processes and porosity description. For example, the model used (CrunchFlow) does not take into account the inhibition effects of silicon in solution on celestite

precipitation, and only one precipitation rate can be used. This means that the model cannot be run for both heterogeneous nucleation and surface growth. SEM observations of the celestite precipitate revealed a wide range of shapes and sizes, suggesting that both mechanisms occur either one after the other or simultaneously. In addition, only one cementation exponent can be determined for the system, even though precipitation renders the system highly heterogeneous and two types of porosities coexist in the clay system. Some published works suggested that complex systems could only be described by a combination of two cementation exponents (e.g.; Tyagi et al. (2013)).

The main limitation of the models resides in the over-simplification of the pore geometry: grid cells represent the porous material, which can be described as a combination of pores and mineral phases. The precipitation of a mineral phase in such grid cells will affect only the porosity, but not the complexity of the diffusion path. This explains the need to impose a very small minimum porosity compared to the experimental porosity value reached in the precipitation front. In the real system, the precipitation will affect in greater proportions the diffusivity if it occurs in pore throats than if it occurs at the surface of the sand grains in large pores. In a next step a pore-scale model approach is needed to model the system. For simple systems as sand, the meshing could be built on μCT images. In such models, part of the grid cells will correspond to pores only, and the rest to mineral phases. This would allow a better description of the precipitation effects on diffusivity due to changes in the migration pathways. For more complex systems such as clays, dual porosities due to permanent surface charges could be implemented.

The experimental data produced for this work can be used to calibrate those models. They are needed to predict transport behaviors in more complex or natural systems on long time

scales, unreachable to the experimentalist (0.1, 1, 10k years). Once the effects of porosity changes on transport properties are better understood, it will be possible to implement other mechanisms, such as incorporation of contaminants into mineral lattices by co-precipitation with secondary mineral phases. Some work has already been performed in this direction: the co-precipitation of lanthanides (Eu^{3+}) and actinides (Cm^{3+}) with celestite and strontianite was characterized in a published work (Holliday et al. (2012), appendix A), and is presented here as complementary material.

Appendix A

Publications

List of publications

- Holliday, K.; **Chagneau, A.**; Schmidt, M.; Claret, F.; Schäfer, T. and Stumpf, T. (2012). *Discriminating factors affecting incorporation: comparison of the fate of Eu^{3+}/Cm^{3+} in the Sr carbonate/sulfate system.* Dalton Transactions, Vol. 41, pp. 3642-3647.

- **Chagneau, A.**; Claret, F.; Enzmann, F.; Wolf, M.; Kersten, M.; Mad, B. and Schäfer, T. *Celestite precipitation-induced pore clogging and its effect on transport parameters in diffusion-controlled porous media.* Geochemical Transactions, *under peer review.*

- **Chagneau, A.**; Tournassat, C.; Steefel, C. I.; Bourg, I. C.; Gaboreau, S.; Esteve, I.; Kupcik, T.; Claret, F.; Enzmann, F. and Schäfer, T. *Complete restriction of $^{36}Cl^-$ diffusion in nanopores of compacted illite.* Environmental Science & Technology Letters, *under peer review.*

Discriminating factors affecting incorporation: comparison of the fate of Eu^{3+}/Cm^{3+} in the Sr carbonate/sulfate system

Kiel Holliday, Aurélie Chagneau, Moritz Schmidt, Francis Claret, Thorsten Schäfer, and Thorsten Stumpf

Abstract

The aim of this work is to assess the effect of ligand strength, symmetry, and coordination number on solid solution formation of trivalent actinides and lanthanides in carbonate and sulfate minerals. This is of particular importance in radionuclide migration where trivalent actinides such as Pu, Am, and Cm are responsible for the majority of radiotoxicity after 1000 years. Time-resolved laser fluorescence spectroscopy was used to study trace concentrations of the dopant ion after interaction with the mineral phase. This study expands on previous work with aragonite and gypsum where it was found that aragonite incorporates Eu^{3+} and Cm^{3+} while only surface sorption is observed in gypsum. This study uses isostructural minerals strontianite ($SrCO_3$) and celestite ($SrSO_4$) to decouple the effect of structure from that due to the anion. It is demonstrated that while distribution coefficients can predict the amount of dopant ion associated with the mineral phase, they do not have any correlation with solid solution formation. This substitution mechanism is most likely dictated by the symmetry of the site being substituted and the electronic structure of the dopant atom.

Introduction

The watermineral interface is a highly complex system offering a multitude of possible interactions for ions in solution. These interactions are typically defined as either sorption to the surface

or incorporation into the bulk of the mineral. An ion sorbing to the mineral surface may retain its hydration sphere, so-called outer-sphere sorption, or it may exchange part of its hydration sphere at the mineral surface, which is referred to as inner-sphere sorption. The only incorporation mechanism discussed in this study is that of isomorphic substitution, where the dopant ion replaces an ion in the mineral crystal structure without significantly altering the local symmetry, creating a solid solution.[A1] More complicated methods of incorporation such as interstitial incorporation and secondary phase formation are not discussed simply because they were not found to be relevant to the systems and conditions that were investigated.

The type of interaction, be it sorption or incorporation, can have drastic implications in geochemical processes such as radionuclide migration.[A2] An ion that is outer-sphere sorbed may be remobilized by a simple change in ionic strength, while an ion that is inner-sphere sorbed would require a change in pH to be released from the mineral surface. In the case of the incorporated species, remobilization would require the dissolution of the host material. Therefore, it is important that efforts to predict radionuclide migration on the geological time scale take into account not only the strength of the interaction, typically quantified by a distribution coefficient (K_d), but also what type of interaction it is.

Those factors that govern whether an ion will be incorporated or merely sorbed to the surface are speculative at best.[A3–A5] It is widely accepted that an ion needs to be able to fit in the site,[A6] but this basic requirement is hardly able to describe all instances of incorporation and surface sorption.[A7–A9] For instance, in the case of Eu^{3+} and Cm^{3+} interaction with $CaCO_3$, the aragonite morphology shows only incorporation while the calcite morphology has both incorporation and surface sorption in predictable quantities.[A10]

The study preceding this by Schmidt et al. aimed at determining some of the aspects governing incorporation versus adsorption by studying the substitution of Ca^{2+} by Eu^{3+} and Cm^{3+} in aragonite ($CaCO_3$) and gypsum ($CaSO_4{\cdot}2H_2O$).[A11] That study showed two calcium based minerals can have very different interactions toward a trivalent doping ion. In the case of aragonite only incorporation was observed. In gypsum, only innersphere surface sorption was evident. This clearly indicated that more than ionic radii must be taken into consideration for solid solution formation. Because the structures of aragonite (orthorhombicdipyramidal, space group: *Pmcn*) and gypsum (monoclinicprismatic, space group: *A2/a*) are different, it was unclear whether this difference was due to the structure or the anion (CO_3^{2-} and SO_4^{2-}).[A12,A13] This study expands on those results to study the aragonite isostructural minerals strontianite ($SrCO_3$) and celestite ($SrSO_4$).[A14,A15] In this way, the difference in structure can be isolated from the difference in anion and a definitive determination of those factors determining incorporation or sorption can be made.

Time resolved laser fluorescence spectroscopy (TRLFS) is a versatile tool for probing the chemical environment of a luminescence emitting ion (here Eu^{3+} and Cm^{3+}) in solids, liquids and at the interface.[A16–A28] Eu^{3+} TRLFS allows determination of the different species to be found in a system by excitation from the $^7F_0$ ground state to the $^5D_0$ state. In this transition both levels are non-degenerate due to their $J = 0$ nature and thus only one singlet signal is observed for each species. Consequently, the number of non-equivalent species is equal to the number of observed transitions as long as resolution and line widths allow an unambiguous separation. In addition, the signal position of the F_0 band gives a first indication of the local environment of the respective Eu^{3+} species: stronger coordination generally results in lower energy transition, *i.e.* stronger bathochromic shift of the

signal.[A29−A31] Consecutive selective excitations of the respective species yield "single species" emission spectra and lifetimes. The emission spectra allow identification of the ion coordination environment in this site, using the splitting pattern and the relative intensity of the ($^5D_0 \rightarrow^7 F_1$) and ($^5D_0 \rightarrow^7 F_2$) transitions, the so-called hypersensitive effect.[A32] The determination of the number of water molecules in the first coordination sphere is possible using Horrocks equation, giving a simple empiric linear relationship between the number of water molecules in the first coordination sphere q and the decay constant k:[A33] q = 1.07 × k - 0.62.

The major advantage of Cm^{3+} luminescence spectroscopy is its very high sensitivity. The detection limit for Cm^{3+} by TRLFS is as low as 10^7 atoms mm^{-2} and spectroscopic characterization of single species is possible even below 1 ppm.[A26,A34,A35] The signal of the ($^6D_{7/2} \rightarrow^8 S_{7/2}$) transition in Cm^{3+} shows significant shifts with changes of the coordination environment. A stronger bathochromic shift ("red shift) indicates a stronger coordination, usually compared to the Cm^{3+} aquo ion with emission at 593.8 nm.[A36] For Cm^{3+} as well, determination of the coordinating water ligands in the first coordination sphere is possible by a empiric linear correlation of q and k, here called Kimuras equation:[A37] q = 0.65 × k - 0.88. Additional information can be gained from high-resolution emission spectra of Cm^{3+}. In all, except centrosymmetric crystal fields, splitting of the ground state level in all four Kramers doublets should be observed. The magnitude of this splitting is highly sensitive to both strength and symmetry of the crystal field. The strength of the field is determined by the metal to ligand distance and the character of the bond.[A38,A39]

Experimental

Sample preparation

Celestite and strontianite precipitation in the presence of Eu^{3+} and Cm^{3+} was performed in a mixed flow reactor (MFR) as described by Schmidt et al.[A11] In this way three solutions are used to feed a chamber containing 160 mg of the parent mineral phase, which is stirred at 850 rot min^{-1}. These three feed solutions are pumped into the chamber at 0.2 mL min^{-1} each and contain the cation, anion, and doping solution, respectively. Each solution is prepared with 0.1 mol $\cdot$ L^{-1} NaCl as a background electrolyte to maintain ionic strength. By maintaining a low to moderate saturation index (SI), surface growth controlled precipitation is the dominant process. The experiments were performed in a glove box under a controlled Ar atmosphere (carbonate free) and with argon exchanged MilliQ water in order to prevent carbonate growth in the sulfate system. All chemicals are reagent grade purchased from Merck with the exception of the ^{248}Cm solution ($\tau_{\frac{1}{2}} = 3.4 \times 10^5$ years). The isotopic composition of the long-lived curium solution is 97.3% ^{248}Cm, 2.6% ^{246}Cm, 0.04% ^{245}Cm, 0.02% ^{247}Cm and 0.009% ^{244}Cm in 1.0 mol $\cdot$ L^{-1} $HClO_4$. Details for each experiment can be found in table A.1. The solution passes through a 0.22 μm filter before the outlet to avoid loss of the solid sample or sampling of colloids in the outlet solution. The outlet solution was sampled throughout the experiment to determine concentrations via ICP-MS. The product was confirmed to be either strontianite or celestite by Xray diffraction (Bruker D8 Advance) using Bruker EVA software.

Time Resolved Laser Fluorescence Spectroscopy

TRLFS was performed using a pulsed (20 Hz) XeCl-excimer laser (Lambda Physics, EMG, 308 nm) pumped dye laser (Lamb-

da Scanmate). The following dyes were used: QUI for UV excitation, Rhodamine 6G for direct excitation of Eu, and Rhodamine B for direct excitation of Cm. Indirect excitation of Eu and Cm was performed at 394.0 nm and 396.6 nm respectively. The range used for the direct excitation of Eu was 575-582 nm and the direct excitation of Cm was done at 600-613 nm. The laser wavelength was monitored using a Toptica WS7 wavemeter ($>10^{-5}$ nm accuracy). Measurements were detected by an optical multichannel analyzer that consists of a polychrometer with 300/600/1200 lines per mm gratings (Jobin Yvon) and an intensified, gated photodiode array (Spectroscopy Instruments). Maximum resolution at 300 and 1200 lines per mm was measured to be 0.9 and 0.2 nm, respectively. The samples were cooled to 16 K by a helium refrigerated cryostat (CTI-cryogenics) to improve resolution. For the discrimination of Rayleigh and Raman scattering the minimum gate delay between laser pulse and camera gating was set to 1.0 μs. The gate width of the camera was fixed at 10 ms to ensure the collection of the entire fluorescence signal. Fluorescence lifetime measurements were made with a delay time step between 15 and 200 μs and a total of 60 steps were taken for each lifetime measurement.

Results and discussion

Europium doped strontianite

Strontianite ($SrCO_3$) doped with Eu^{3+} as described above was analyzed by TRLFS. The excitation wavelength was varied and the fluorescence signal from the ${}^5D_0 \rightarrow {}^7F_{0,1,2}$ was integrated to create the excitation spectra shown in Fig. A.1. By varying the energy of the laser around the non-degenerate F_0 transition energy, the number of peaks is a direct measure of the number of unique Eu^{3+} environments. As can be seen by Fig. A.1, only a

Table A.1: Basic growth parameters and dopant concentrations for the investigated samples compared with previous study [A11]. The experiment duration is given as t in hours

Sample	SI	t hours	$[M^{3+}]$ mmol $\cdot$ L^{-1}	pH
Eu-$SrCO_3$	3.52	341	450	9.7
Cm-$SrCO_3$	3.43	288	24	9.3
Eu-$SrSO_4$	0.78	405	450	6.6
Cm-$SrSO_4$	0.84	288	69	5.3
Eu-gypsum [A11]	0.1	523	450	-
Cm-gypsum [A11]	0.1	236	1	-
Eu-aragonite [A11]	1.16	657	600	-
Cm-aragonite [A11]	1.16	528	1	-

single peak is evident for the strontianite sample, indicating only one Eu species is present in this system and the F_0 transition is at 578.5 nm. This compares well to the previous study on the aragonite ($CaCO_3$) which had a similar energy transition at 579.4 nm.[A11]

The decay of the Eu^{3+} fluorescence signal is mono-exponential (data not shown) further indicating the presence of one Eu species, given the slow exchange expected at 16 K. The lifetime of this fluorescence was found to be 1.6 ms by fitting to the standard mono-exponential decay (Table A.2). The reciprocal observed lifetime (k) is related to the number of water molecules in the immediate coordination sphere by the Horrocks equation,[A33] which is used to distinguish between outer sphere sorption, inner sphere sorption, and incorporation. By this relationship the long lifetime of 1.6 ms indicates a complete loss of the hydration sphere and incorporation into the bulk. The lifetime is the same as that found for the isostructural $CaCO_3$ (aragonite) where it was determined that Eu^{3+} incorporates through

isomorphic substitution on a Ca^{2+} site.[A11]

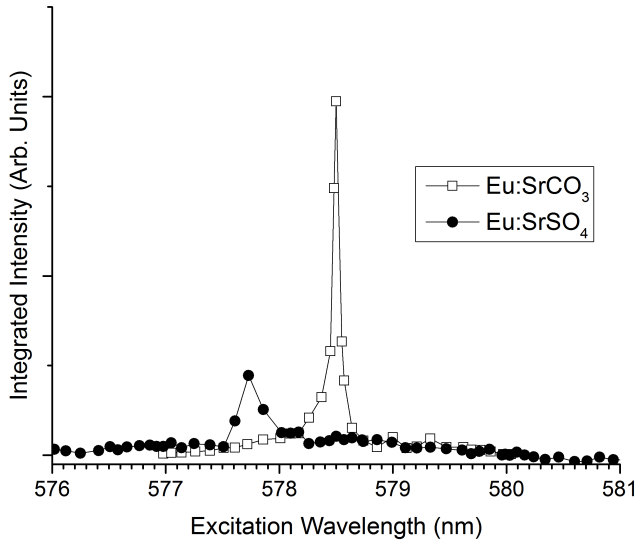

Figure A.1: Excitation spectra of Eu^{3+} doped strontianite and celestite integrated over the $^5D_0 \rightarrow ^7 F_{0,1,2}$ transitions at low temperature (16 K).

Table A.2: Lifetime and position of fluorescence emission in Eu^{3+} and Cm^{3+} doped aragonite, strontianite, and celestite.

Sample	Wavelength (F_0 or $S_{7/2}$) nm	Lifetime ms
Eu-$CaCO_3$ [A11]	579.4	1.6
Eu-$SrCO_3$	578.5	1.6
Eu-$SrSO_4$	577.7	3.1
Cm-$CaCO_3$ [A11]	612.7	0.64
Cm-$SrCO_3$	608.5	0.47
Cm-$SrSO_4$	596.3	1.1

Further proof of isomorphic substitution can be seen in the fluorescence emission spectrum of Eu^{3+} doped strontianite as compared to aragonite (Fig. A.2). The Eu^{3+} occupies the same

site in both systems as shown by the very similar emission spectra. The strontianite shows less of a bathochromic shift, most likely due to slightly less electron orbital overlap in the larger lattice. The fully degenerate 3-fold splitting of the F_1 and 5-fold splitting of the F_2 transitions indicate a low symmetry in agreement with the C_s symmetry of the cation site. It can be concluded; therefore, that Eu^{3+} undergoes isomorphic substitution in strontianite as was expected from previous studies with aragonite.[A11]

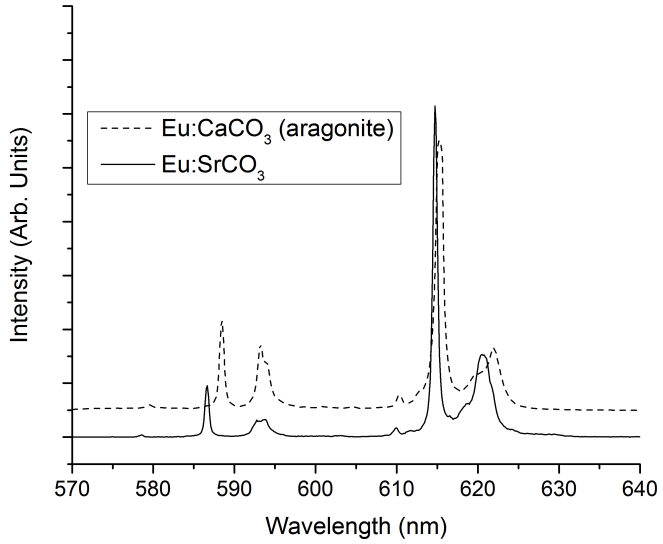

Figure A.2: Emission spectra of Eu^{3+} oped aragonite[A11] and strontianite after direct excitation to $^5D_0$ at low temperature (16 K).

Curium doped strontianite

Curium doped strontianite was prepared and analyzed in the same way as the Eu^{3+} sample. The excitation spectrum and emission spectrum from indirect excitation (396.6 nm) show the same quadruple peak around 608.5 nm (Fig. A.3). This

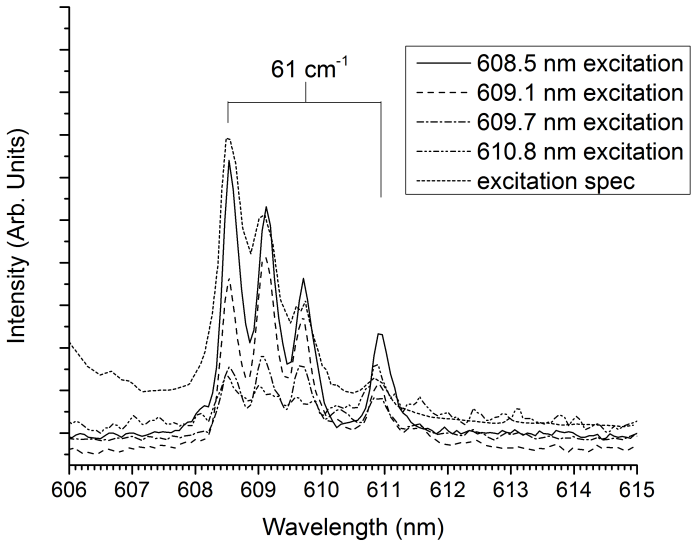

Figure A.3: High resolution emission spectra of Cm^{3+} doped strontianite after excitation to each Kramer doublet as compared to the excitation spectrum at low temperature (16 K).

large bathochromic shift from the aqueous Cm^{3+} species (593.8 nm)[A39] is indicative of the strong complexation with the carbonate ligand. This quadruplet was shown to arise from the same Cm^{3+} species by direct excitation. The emission spectra produced by exciting at each fluorescence maximum in the excitation spectra produce identical results. The quadruplet is therefore a 4-fold splitting of the $^8S_{7/2}$ ground state in a single Cm^{3+} species. Although this splitting is extremely large at 61 cm^1, it is slightly less than the Cm^{3+} doped aragonite that had a ground state splitting of 66 cm^1.[A11] This slight decrease in the strength of splitting indicates less orbital mixing between the Cm^{3+} and the carbonate ligand.[A38] This is also evident in the peak position of Cm^{3+} doped strontianite (608.5 nm) compared with aragonite (612.7 nm). The weaker bathochromic shift in strontianite indicates less interaction with the surrounding lig-

ands. This is presumed to be due to the $SrCO_3$ lattice being larger than the isostructural $CaCO_3$, creating a larger CmO bond distance, resulting in less electron orbital overlap. The average cation to oxygen distance in aragonite is 2.528 Å, while it is 2.636 Å in strontianite.[A14]

The fluorescence lifetime shows a mono-exponential decay reinforcing the conclusion of a single Cm^{3+} species. The lifetime of the fluorescence decay was measured to be 0.47 ms (Table A.2). This can be related to the number of water molecules in the immediate coordination sphere by the Kimura equation,[A35] which shows a complete loss of the hydration sphere. This is consistent with the results from the Eu^{3+} doped strontianite and indicates that Cm^{3+} also undergoes an isomorphic substitution onto the Ca^{2+} site.

Europium doped celestite

Celestite, as compared to strontianite, offers the unique opportunity to analyze the anion effect on uptake and solid solution formation while maintaining the same structure and cation. Celestite had very little uptake of the trivalent dopant ion as determined by ICP-MS, which can be related to the weakness of SO_4^{2-} as a ligand.[A11,A34,A41] Evidence of this can be seen in the signal to noise ratio of the excitation spectra of Eu^{3+} doped celestite (Fig. A.1). The maximum excitation wavelength for Eu^{3+} in celestite at 577.7 nm produces a much lower fluorescence signal than that of strontianite despite efforts to maximize the signal (more accumulations, greater laser power, etc.). Unfortunately, exact values for uptake could not be determined in either case. In celestite the difference in concentration between input solution and output was not significant enough for reliable quantification. In strontianite the amount of Eu^{3+} in the output solution was insufficient for quantification. Therefore, it can be

said that at these concentrations Eu^{3+} is quantitatively associated with the strontianite, while less than 5 wt.% is associated with celestite under similar conditions. Quantification of kinetic and thermodynamic parameters in these systems will be a focus of future studies.

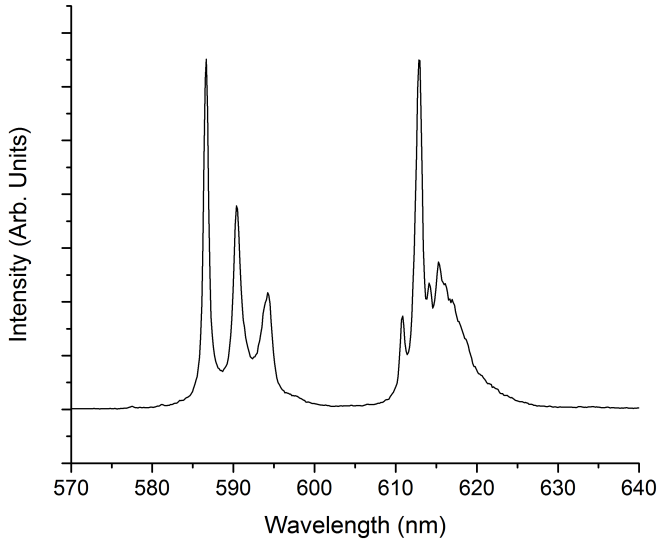

Figure A.4: Emission spectrum of Eu^{3+} doped celestite after indirect excitation (394 nm) at low temperature (16 K).

The emission spectrum from indirect excitation (394 nm) for Eu^{3+} doped celestite is shown in Fig. A.4. As can be seen there is a 3-fold splitting of the $^5D_0 \rightarrow^7 F_1$ transition between 585 and 595 nm indicating low symmetry, as can be expected by both surface sorbed and incorporated species due to the low symmetry of the Ca^{2+} site. The $^5D_0 \rightarrow^7 F_2$ transition from 610620 nm shows multiple peaks although the signal is not strong enough to achieve adequate resolution. The fluorescence decay was measured time resolved as previously performed for strontianite and was shown to be mono-exponential indicating a single species of Eu^{3+}. This was fitted to the standard exponential decay equa-

tion and the lifetime was determined to be 3.1 ms. This long fluorescence lifetime proves that Eu^{3+} is incorporated into the celestite crystal structure despite having a very weak interaction with the solid. It is presumed to be occupying a Ca^{2+} site and not an interstitial or grain boundary site due to the well defined nature of the site.[A40] This would also be consistent with the isostructural strontianite and aragonite.

Curium doped celestite

Cm^{3+} doped celestite was prepared and analyzed in the same way as the previous samples. As was the case for Eu^{3+}, uptake of Cm^{3+} by celestite was significantly less than that of strontianite due to the weaker binding of the SO_4^{2-} ; however, reliable quantification was not possible. This will be addressed in further studies to establish kinetic and thermodynamic constants. Nevertheless, it was possible to probe the Cm^{3+} by TRLFS due to the low detection limit of the technique. The emission spectrum shows a single peak at 596.3 nm, which can be compared to the Cm^{3+} peak in strontianite at approximately 608.5 nm (Fig. A.5) as well as the Cm aquo ion (593.8 nm[A39]). Clearly, the ligand field of the celestite cation site demonstrates a much smaller bathochromic shift than strontianite due to a weaker interaction with the SO_4^{2-} than with CO_3^{2-}. Additionally, the presence of a single peak suggests that there is only one Cm^{3+} species present.

The fluorescence decay was measured to confirm the presence of only one Cm^{3+} environment and determine whether that species was incorporated into the bulk or sorbed to the surface.

Fig. A.6 shows the lifetime measurements of two different samples with two different time steps to ensure that only one species is present. The first lifetime was taken with time steps of 75 μs to a maximum of 3.8 ms and the second lifetime was taken with a time step of 5 μs to ensure that there is no shorter lived

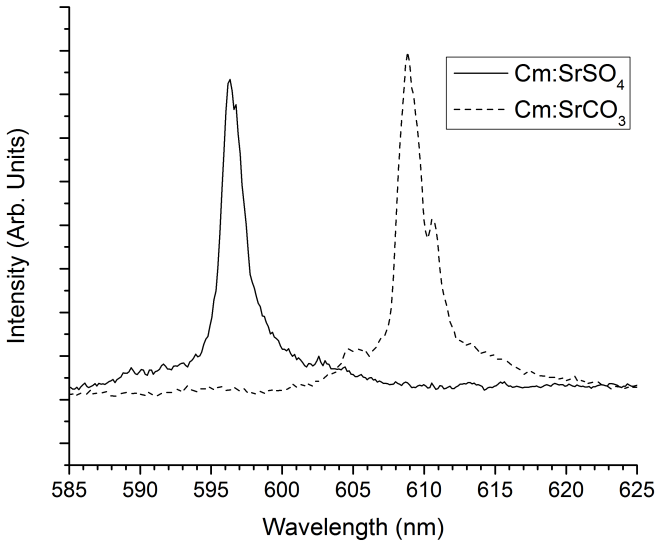

Figure A.5: Emission spectra of Cm^{3+} doped strontianite and celestite after excitation to ${}^6D_{7/2}$ at low temperature (16 K).

species not shown in the larger time step measurement. This was repeated in the same way for the second sample. All four data sets show a mono-exponential lifetime proving the presence of only a single Cm^{3+} species. All four data sets were fitted, with similar results, and produce the same fluorescence lifetime of 1.1 ms clearly indicating a loss of the hydration sphere and proving that Cm^{3+} is also incorporated into the bulk. This is consistent with the data obtained for Eu^{3+}. These results show that even though the SO_4^{2-} has a much weaker interaction than CO_3^{2-}, resulting in a lower uptake of trivalent cations, it is not the driving factor for solid solution formation.

Conclusions

This study aims to address the fundamental parameters affecting uptake and solid solution formation. By examining the isostruc-

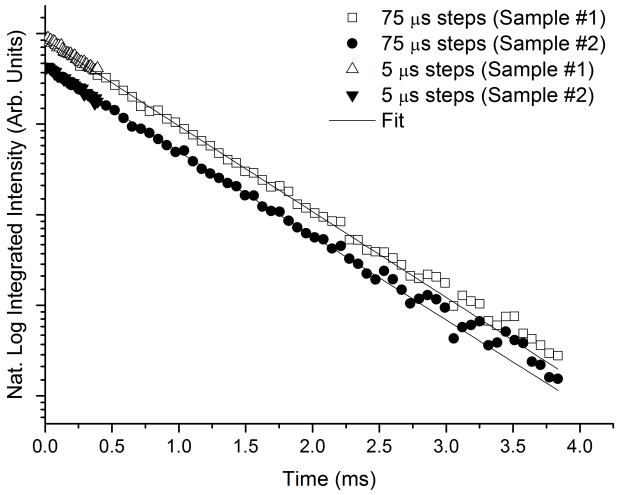

Figure A.6: Lifetime measurements of two celestite samples performed with time steps of 5 and 75 μs at low temperature (16 K). Lines represent the fit from the standard mono-exponential decay equation.

tural minerals celestite and strontianite and comparing to past studies of calcite,[A10] aragonite, and gypsum[A11] one is able to compare the effect of cation, anion, and structural parameters in a systematic way. It was found that while the cation has the least effect, it can still change the local structure at the atomic level. This can be seen by comparing strontianite ($SrCO_3$) to the isostructural aragonite ($CaCO_3$). Here it was shown that the strontianite has slightly less molecular orbital interaction between the incorporated trivalent cation and the surrounding oxygen due to the larger distance maintained by a larger crystal structure.

The anion was found to have the most dramatic effect on the uptake of the trivalent cation by the solid mineral phase, which was seen by comparing the much stronger CO_3^{2-} ligand having greater uptake than the weak SO_4^{2-} ligand in isostructural strontianite and celestite, respectively. This is the strength

of determining distribution coefficients and has been the common practice for predicting radionuclide migration.[A2] This does not, however, determine the ability of a mineral to incorporate the trivalent contaminant into a solid solution. This was evident in celestite, which had very little uptake of both Eu^{3+} and Cm^{3+} from solution. The Eu^{3+} and Cm^{3+} that was associated with the solid phase was incorporated as a solid solution, which would make it much more stable than if it were merely sorbed to the surface. This is in contrast to the previous study on gypsum, where weak uptake was also associated with surface sorption.[A11]

This leaves structure as the driving force of solid solution formation. While size is a fundamental requirement for incorporation, as has been exploited to determine charge compensation,[A10] other parameters control the interaction when a dopant will fit into the crystal lattice. This is seen in this and the previous study[A11] where exclusively incorporation (aragonite type structures), exclusively surface sorption (gypsum), and a mixture of both (calcite) has been observed in structures with very similar sized cation sites and no systematic trend is present. This same reasoning can be applied to coordination number. A 9-fold coordination results in solid solution formation, while 8-fold coordination only shows surface sorption, and 7-fold is mixed indicating no simple trend or preferred coordination number of the trivalent dopant ion in the mineral phases studied. The conclusion proposed here is that solid solution formation is dictated by the ability of the dopant ions electronic structure to adapt to the symmetry of the crystal structure to create sufficient molecular orbital overlap with the surrounding environment.

This shows the limitation in using distribution coefficients (K_d) for the determination of radionuclide migration over geologic time scales, where changing environmental factors are almost certain. The determination of how the radionuclide is

associated with the mineral phase is vital in a changing environment. While a simple change in pH or ionic strength can remobilize a radionuclide sorbed on a mineral surface, the stability of an incorporated ion is directly related to the stability of the mineral as a whole. This could mean that while a mineral such as calcite has a large uptake of trivalent actinides and lanthanides, the material might migrate further than the material associated with celestite, which has a much weaker uptake, due to the remobilization of surface sorbed species in the calcite system. This example is only to illustrate the importance of the concept and not to suggest that the radionuclide migration in celestite as compared to calcite is specifically addressed in this study. Nevertheless, an atomic scale, mechanistic understanding of processes occurring at the solidsolution interface is essential for prediction of radionuclide migration over geologic time scales.

Acknowledgements

We acknowledge ACTINET I-3 for financial support through the joint research proposal JRP-07. This work was co-financed by the Helmholtz Gemeinschaft Deutscher Forschungszentren (HGF) by supporting the Helmholtz-Hochschul-Nachwuchsgruppe “Aufklrung geochemischer Reacktionsmechanismen an der Wasser /Mineralphasen Grenzflaeche”. The authors thank S. Buechner for technical assistance with the laser fluorescence measurements. This work was performed under the auspices of the U.S. Department of Energy by Lawrence Livermore National Laboratory under Contract DE-AC52-07NA27344 and by the Department of Homeland Security, Domestic Nuclear Detection Office under Contract HSHQDC-07-C-00034.

References

A1 A. J. Tesoriero and J. F. Pankow, Geochim. Cosmochim. Acta, 1996, 60, 1053.

A2 H. Geckeis and T. Rabung, J. Contam. Hydrol., 2008, 102, 187.

A3 K. J. Davis, P. M. Dove and J. J. D. Yoreo, Science, 2000, 290, 1134.

A4 A. G. Shtukenberg, Y. O. Punin and P. Azimov, Am. J. Sci., 2006, 306, 553.

A5 S. L. S. Stipp, J. Konnerup-Madsen, K. Franzreb, D. A. Kulik and H. J. Matheiu, Nature, 1998, 396, 356.

A6 J. Bruno, D. Bosbach, D. A. Kulik and A. Navrotsky, Chemical Thermodynamics of Solid Solutions of Interest in Nuclear Waste Management, OECD Publishing, London, 2007.

A7 J. Rakovan and R. J. Reeder, Geochim. Cosmochim. Acta, 1996, 60, 4435.

A8 M. E. Fleet and Y. Pan, Am. Mineral., 1995, 80, 329.

A9 Y. Terakado and A. Masuda, Chem. Geol., 1998, 69, 103.

A10 M. Schmidt, T. Stumpf, M. M. Fernandes, C. Walther and T. Fanghnel, Angew. Chem., Int. Ed., 2008, 47, 5846.

A11 M. Schmidt, T. Stumpf, C. Walther, H. Geckeis and T. Fanghnel, Dalton Trans., 2009, 6645.

A12 A. Dal Negro and L. Ungaretti, Am. Mineral., 1971, 56, 768.

A13 P. F. Schofield, K. S. Knight and I. C. Stretton, Am. Mineral., 1996, 81, 847.

A14 J. P. R. Villiers, Am. Mineral., 1971, 56, 758.

A15 R. W. James and W. A. Wood, Proc. R. Soc. London, Ser. A, 1925, 109, 598.

A16 T. Stumpf, T. Fanghnel and I. Grenthe, J. Chem. Soc., Dalton Trans., 2002, 3799.

A17 K. Binnemans and C. Grller-Walrand, J. Alloys Compd., 1997, 250, 326.

A18 J. A. Capobianco, P. P. Proulx, N. Raspa, D. J. Simkin and D. Krashkevich, J. Chem. Phys., 1989, 90, 2856.

A19 H. Eilers and B. M. Tissue, Chem. Phys. Lett., 1996, 251, 74.

A20 V. Lavin, P. Babu, C. K. Jayasankar, I. R. Martin and V. D. Rodriquez, J. Chem. Phys., 2001, 115, 10935.

A21 V. Lavin, U. R. Rodriquez-Mendoza, I. R. Martin and V. D. Rodriquez, J. Non-Cryst. Solids, 2003, 319, 200.

A22 B. Piriou, A. Elfakir and M. Quarton, J. Lumin., 2001, 93, 17.

A23 B. Piriou, M. Fedoroff, J. Jeanjean and L. Bercis, J. Colloid Interface Sci., 1997, 194, 440.

A24 S. Stumpf, T. Stumpf, C. Walther, D. Bosbach and T. Fanghnel, Radiochim. Acta, 2006, 94, 243.

A25 T. Stumpf, A. Bauer, F. Coppin, T. Fanghnel and J. I. Kim, Radiochim. Acta, 2002, 90, 345.

A26 T. Stumpf and T. Fanghnel, J. Colloid Interface Sci., 2002, 249, 119.

A27 N. Huittinen, Th. Rabung, J. Ltzenkirchen, S. C. Mitchell, B. R. Bickmore, J. Lehto and H. Geckeis, J. Colloid Interface Sci., 2009, 332, 158.

A28 N. Huittinen, Th. Rabung, P. Andrieux, J. Lehto and H. Geckeis, Radiochim. Acta, 2010, 98, 613.

A29 G. R. Choppin and D. R. Peterman, Coord. Chem. Rev., 1998, 174, 283.

A30 G. R. Choppin and Z. M. Wang, Inorg. Chem., 1997, 36, 249.

A31 S. T. Frey and W. DeW. Horrocks, Inorg. Chem., 1995, 229, 383.

A32 D. E. Henrie, R. L. Fellows and G. R. Choppin, Coord. Chem. Rev., 1976, 18, 199.

A33 W. DeW. Horrocks and D. R. Sudnick, J. Am. Chem. Soc., 1979, 101, 334.

A34 N. M. Edelstein, R. Klenze, T. Fanghnel and S. Hubert, Coord. Chem. Rev., 2006, 250, 948.

A35 P. Lindqvist-Reis, C. Apostolidis, J. Rebizant, A. Morgenstern, R. Klenze, O. Walter, T. Fanghnel and R. G. Haire, Angew. Chem., Int. Ed., 2007, 46, 919.

A36 J. I. Kim, R. Klenze and H. Wimmer, Eur. J. Solid State Inorg. Chem., 1991, 28, 347.

A37 T. Kimura and G. R. Choppin, J. Alloys Compd., 1994, 213214, 313.

A38 P. Lindqvist-Reis, C. Walther, R. Klenze, A. Eichhfer and T. Fanghnel, J. Phys. Chem. B, 2006, 110, 5279.

A39 P. Lindqvist-Reis, R. Klenze, G. Schubert and T. Fanghnel, J. Phys. Chem. B, 2005, 109, 3077.

A40 K. S. Holliday, S. Handley-Sidhu, J. Renshaw, C. Walther, L. Mackaskie and T. Stumpf, Langmuir, DOI: 10.1021/la300014a.

A41 R. Silva and H. Nitsche, Radiochim. Acta, 1995, 70/71, 377.

Appendix B

Model sensitivity analysis

The sensitivity of the CrunchFLow reactive transport model to several parameters (mesh size, tortuosity factor, porosity, cementation exponent, mesh homogeneity and heterogeneity, kinetic regime and specific surface area of the precipitating phase) was tested in 1D and 2D, and with and without clogging. The case study of the experiment S1-HTO1 was used, with the experimental values of porosity, tortuosity and cementation exponent obtained from the linear regression method. The diffusion cell S1-HTO1 consisted of a 50 mm long, 10 mm diameter compacted purified sea sand column, with a 2 mm thick filter support at each end of the column, for a total length of 54 mm. The reservoirs and pores contained a solution of 1 $\text{mmol} \cdot \text{L}^{-1}$ NaCl, and the HTO tracing experiment lasted 26 days. The HTO concentration in the high concentration reservoir was of 4900 $\text{Bq} \cdot \text{mL}^{-1}$ (4.63×10^{-9} $\text{mol} \cdot \text{L}^{-1}$). The porosity, obtained with the Linear Regression (LR) method was 0.415 ± 0.021. The LR cementation exponent was equal to 2.10 ± 0.10, and the LR tortuosity factor to 0.391 ± 0.111.

Simple transport model (no porosity clogging)

In the present case, the sensitivity of the model was tested on the simple HTO through diffusion, prior to porosity clogging. First, the sensitivity of the model to the mesh size was tested. Then, the porosity, tortuosity factor and cementation exponent were varied of ± 5%, a value corresponding to the experimental error on the porosity, cementation exponent and HTO flux and cumulative activity.

1D model

The configurations tested are reported in table B.1. The modeled HTO fluxes are reported in fig. B.1. Two different parameters can be used in the D_e/εrelationship as described by Archie's law in the CrunchFlow code - the cementation exponent, m, or the tortuosity factor, τ:

$$\frac{D_e}{D_w} = \varepsilon^m = \varepsilon \cdot \tau \tag{B.1}$$

A specific tortuosity factor for each mesh-cell can be defined, which is an advantage in a medium with heterogeneous tortuosities such as ours. Indeed, the filter supports have a tortuosity factor of 1.00 (straight cylindrical pores), while the sand and illite have an average τ of 0.XX ± 0.XX and 0.XX ± 0.XX, respectively. However, when using the cementation exponent option, only one value can be defined for the whole system. The modeled flux curves are therefore significantly different than for the tortuosity option. To correct this, it is possible to calculate a theoretical porosity for the filter supports, that would correspond to a tortuosity of 1.00 with the cementation exponent of the porous material. For the filter supports of the sand system, the corrected porosity used in the sensitivity analysis runs was

Table B.1: Different configurations tested for the 1D transport model sensitivity analysis (no clogging).

Model ID	Mesh size	Porosity		Tortuosity	Cementation
	mm	Sand	Filter supports		exponent
1.1	1.0	0.415	0.370	0.391	not used
2.1	0.5	0.415	0.370	0.391	not used
3.1	0.1	0.415	0.370	0.391	not used
3.2	0.1	0.415	0.370	not used	2.10
3.3	0.1	0.415	0.623	not used	2.10
3.4	0.1	0.436	0.370	0.391	not used
3.5	0.1	0.394	0.370	0.391	not used
3.6	0.1	0.415	0.370	0.400	not used
3.7	0.1	0.415	0.370	0.362	not used
3.8	0.1	0.415	0.623	not used	2.21
3.9	0.1	0.415	0.623	not used	1.99

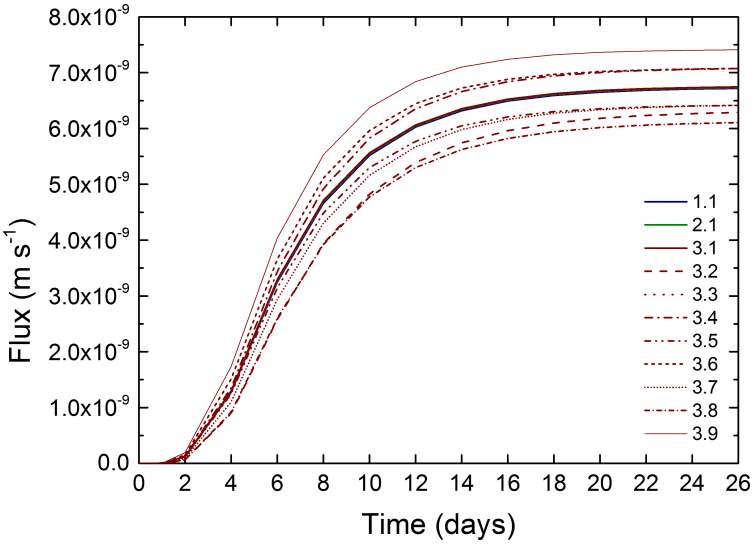

Figure B.1: Modeled HTO fluxes for different configurations tested for the 1D simple transport model (no porosity clogging) sensitivity analysis.

0.623. The flux thus modeled is in good agreement with the "tortuosity" model.

The model is not dependent on the mesh size. It is, however, quite sensitive to the cementation factor value: a variation in the cementation factor of about 5% leads to a 10% difference in the flux at 26 days. A similar variation of 5% in the tortuosity only yields to a 5% variation in the flux at 26 days. The tortuosity factor option was thus chosen over the cementation factor option, as it is more convenient, reliable (no need to recalculate a porosity for the filter supports) and as the model is less sensitive to this parameter.

2D homogeneous model

A simple 2D model was tested, with a homogeneous distribution of tortuosity and porosity for the filter supports. The sensitivity of the model to the mesh size in the X and Y directions was tested, as well as the sensitivity to number of cells in the Y direction, to the porosity, tortuosity factor and cementation exponent. The configurations tested are reported in table B.2. The modeled HTO fluxes are reported in fig. B.2.

The 2D homogeneous through diffusion model is not dependent on the number of cells in the y-direction (2, 5 and 10 cells were tested, results not shown here). As for the 1D model, there is also no dependence on the mesh size, in the case where the mesh is the same in the X and Y direction, or with a different meshing in the X and Y direction (results not shown here). The 2D-homogeneous model is as sensitive to the tortuosity factor and cementation exponent as the 1D model.

2D realistic model

2D models with a realistic filter supports geometry were tested. The aim was to reproduce in the model the geometry of the filter supports (straight holes of 1 mm diameter pierced in impermeable materials, see fig. XXXX). The straight holes were

Table B.2: Different configurations tested for the 2D homogeneous transport model sensitivity analysis (no-clogging).

Model ID	Mesh size (X-Y) mm	Porosity		Tortuosity	Cementation exponent
		Sand	Filter supports		
4.1	1.0-1.0	0.415	0.370	0.391	not used
4.1-1	1.0-1.0	0.436	0.370	0.391	not used
4.1-2	1.0-1.0	0.394	0.370	0.391	not used
4.1-3	1.0-1.0	0.415	0.370	0.400	not used
4.1-4	1.0-1.0	0.415	0.370	0.362	not used
4.1-5	1.0-1.0	0.415	0.623	not used	2.21
4.1-6	1.0-1.0	0.415	0.623	not used	1.99
4.2	1.0-0.5	0.415	0.370	0.391	not used
4.3	1.0-0.1	0.415	0.370	0.391	not used
5.1	0.5-1.0	0.415	0.370	0.391	not used
5.2	0.5-0.5	0.415	0.370	0.391	not used
6.1	0.1-1.0	0.415	0.370	0.391	not used
6.3	0.1-0.1	0.415	0.370	0.391	not used

modeled as grid cells with a porosity and tortuosity of 1.00, and the matrix with a very small porosity of 1 $\times 10^{-14}$, as a value of 0 could not be entered in the input files of the model. First, a simple filter supports geometry of 0-1-0 (a succession of grid cells with a porosity of 0, then 1 then 0 again) was tested with different mesh sizes in the X and Y directions (models 7a, 7b, 7c, 8a, 8b, 8c, 9a, 9b and 9c). Then, an even more realistic geometry was tested, with a succession of 0-1-0-1-0-1-0 over 10 mm in the Y direction (models 7a1 and 9c1). Finally, the sensitivity of the models on the porosity, tortuosity factor and cementation exponent was tested (models 7a2 to 7a8 and 9c2 to 9c8). The configurations tested are reported in table B.3.

The geometry and meshing of the filter supports used in the different models is schematically represented in fig. B.3. The

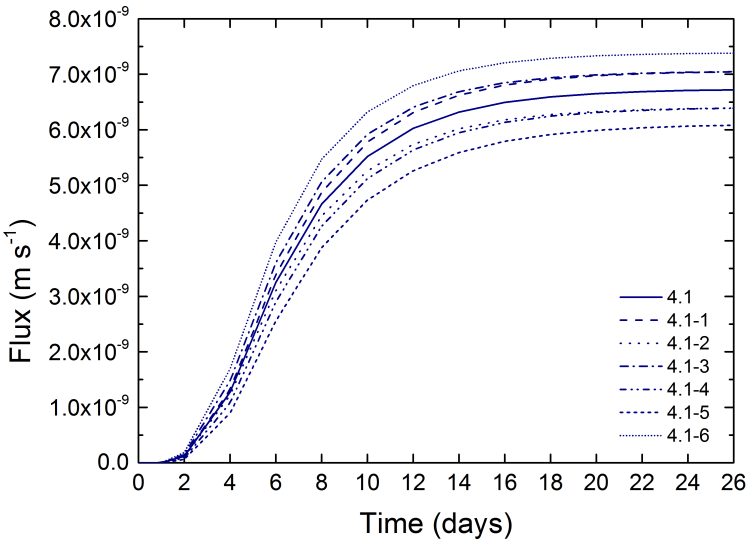

Figure B.2: Modeled HTO fluxes for different configurations tested for the 2D homogeneous simple transport model (no porosity clogging) sensitivity analysis.

modeled holes of the filter supports were always 1 mm wide in the Y direction. In all models except 7a1 and 9a1, the total accessible porosity of the filter supports was 0.333 instead of 0.370. This bias was introduced to simplify the 2D models for the sensitivity analysis (smaller models leading to smaller calculation times), and were corrected when the models were used to reproduce and predict the experimental data.

The effect of the mesh sizes in the X and Y directions is minor. Indeed, the biggest difference between the models was only of 4% in the flux value at 26 days, and was observed when comparing the 7c, 8c and 9c configurations (fig. B.4-A). The differences in the modeled fluxes are also minor when comparing the 9c and 9c1 models, where the first in a simple 0-1-0 succession in the filter supports porosities, while the second is a more realistic 0-1-0-1-0-1-0-1-0 succession (fig. B.4-B). However it is not the case when comparing the similar case of the 7a and 7a1 models, where the difference is important (18% in the flux value

Table B.3: Different configurations tested for the 2D realistic transport model sensitivity analysis (no clogging).

Model ID	Mesh size (X-Y) mm	Porosity Sand	Porosity Filter supports	Tortuosity	Cementation exponent
7a	1.0-1.0	0.415	0.333	0.391	not used
7a1	1.0-1.0	0.415	0.370	0.391	not used
7a2	1.0-1.0	0.436	0.333	0.391	not used
7a3	1.0-1.0	0.394	0.333	0.391	not used
7a4	1.0-1.0	0.415	0.333	0.400	not used
7a5	1.0-1.0	0.415	0.333	0.362	not used
7a6	1.0-1.0	0.415	0.623	not used	2.21
7a7	1.0-1.0	0.415	0.623	not used	1.99
7a8	1.0-1.0	0.415	0.623	not used	2.10
7b	0.5-1.0	0.415	0.333	0.391	not used
7c	0.1-1.0	0.415	0.333	0.391	not used
8a	1.0-0.5	0.415	0.333	0.391	not used
8b	0.5-0.5	0.415	0.333	0.391	not used
8c	0.1-0.5	0.415	0.333	0.391	not used
9a	1.0-0.1	0.415	0.333	0.391	not used
9b	0.5-0.1	0.415	0.333	0.391	not used
9c	0.1-0.1	0.415	0.333	0.391	not used
9c1	0.1-0.1	0.415	0.370	0.391	not used
9c2	0.1-0.1	0.436	0.333	0.391	not used
9c3	0.1-0.1	0.394	0.333	0.391	not used
9c4	0.1-0.1	0.415	0.333	0.400	not used
9c5	0.1-0.1	0.415	0.333	0.362	not used
9c6	0.1-0.1	0.415	0.623	not used	2.21
9c7	0.1-0.1	0.415	0.623	not used	1.99
9c8	0.1-0.1	0.415	0.623	not used	2.10

at 26 days). The reason for such a difference is unknown. The sensitivity of the model to the sand porosity, tortuosity factor

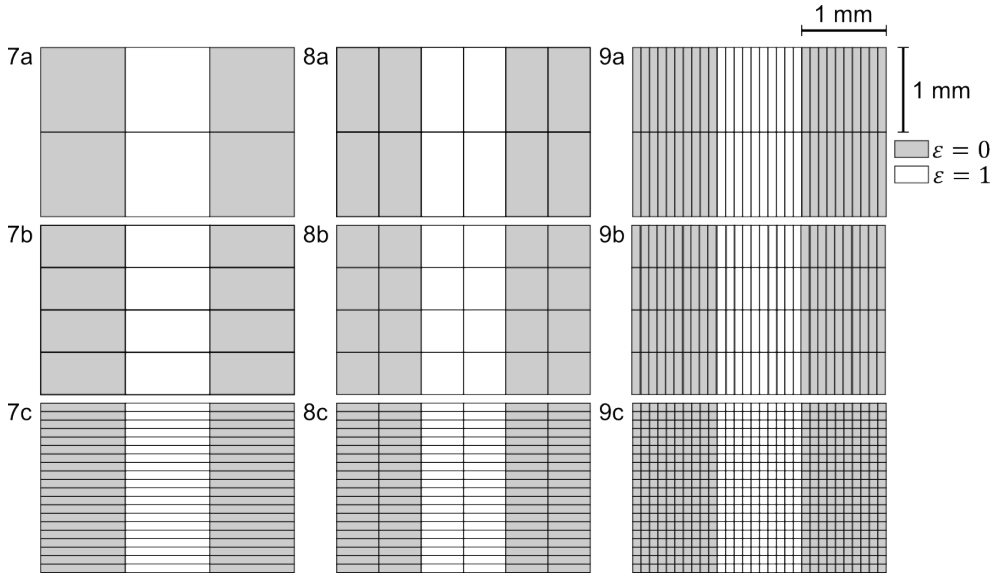

Figure B.3: Schematic representation of the meshing and geometry of the filter supports for the different 2D realistic transport models used in the sensitivity analysis.

and cementation exponent is similar to the 1D and 2D homogeneous models for the models 7a to 7a8 (fig. B.4-C). The model series 9c is however more sensitive to the cementation exponent than all other models (fig. B.4-D), but similarly sensitive to the sand porosity and tortuosity factor.

Reactive transport model (porosity clogging)

The sensitivity of the reactive transport models on the porosity, tortuosity factor and cementation exponent of the sand was tested, as for the non-reactive models previously discussed. A typical precipitation experiment was used to set-up the model. For that purpose, a 0.5 $\text{mol} \cdot \text{L}^{-1}$ $SrCl_2$ solution was introduced in the first reservoir (the one containing the tracer), and 0.5 $\text{mol} \cdot \text{L}^{-1}$ Na_2SO_4 in the second reservoir. The pore solution was 0.5 $\text{mol} \cdot \text{L}^{-1}$ NaCl.

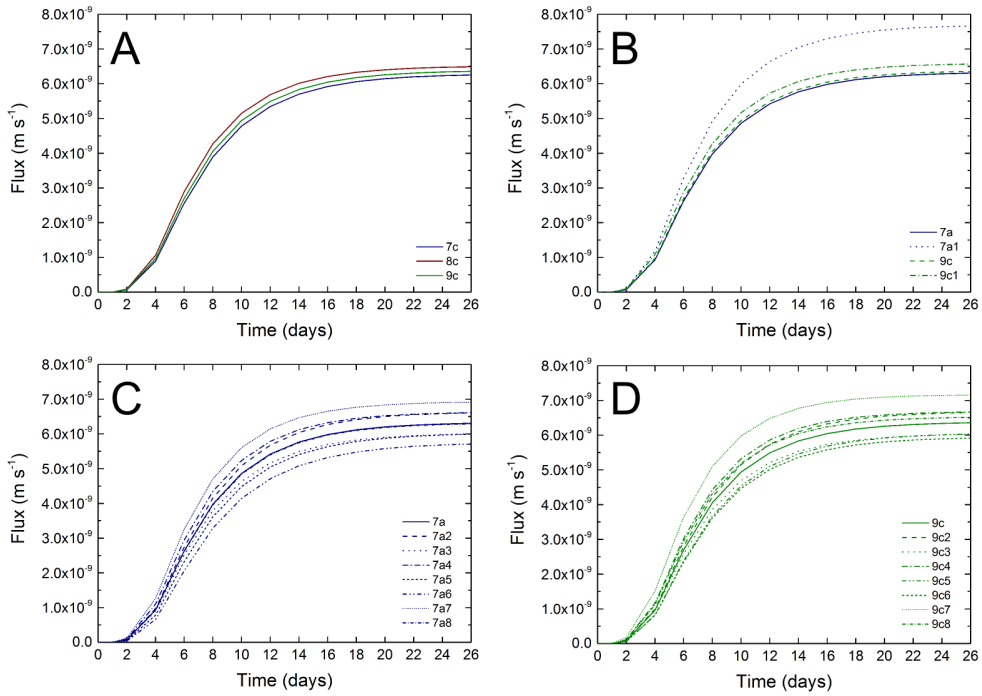

Figure B.4: Modeled HTO fluxes for different configurations tested for the 2D realistic transport model sensitivity analysis (no porosity clogging).

1D model

The major difference with the non reactive model was that the tortuosity factor could not be used, as it gave irrelevant results. Therefore, the cementation exponent was used instead, with a modified porosity for the filter supports as described previously. The different configurations tested are reported in table B.4. The modeled HTO fluxes are reported in fig. B.5.

The porosity clogging is translated in the HTO flux by a significant drop and stabilization at low values. A steep drop is representative of a fast clogging. The reactive transport model is very sensitive to the mesh size: the smaller the mesh size, the faster the clogging. This can be explained simply by the fact that a small mesh cell will be filled with the precipitate faster than a bigger one. The HTO flux is similarly sensitive to

Table B.4: Different configurations tested for the 1D transport model sensitivity analysis (with porosity clogging).

Model ID	Mesh size	Porosity		Tortuosity	Cementation
	mm	Sand	Filter supports		exponent
10a	1.0	0.415	0.623	not used	2.10
10b	0.5	0.415	0.623	not used	2.10
10c	0.1	0.415	0.623	not used	2.10
10c1	0.1	0.415	0.370	0.391	not used
10c2	0.1	0.436	0.623	not used	2.10
10c3	0.1	0.394	0.623	not used	2.10
10c4	0.1	0.415	0.623	not used	2.21
10c5	0.1	0.415	0.623	not used	1.99

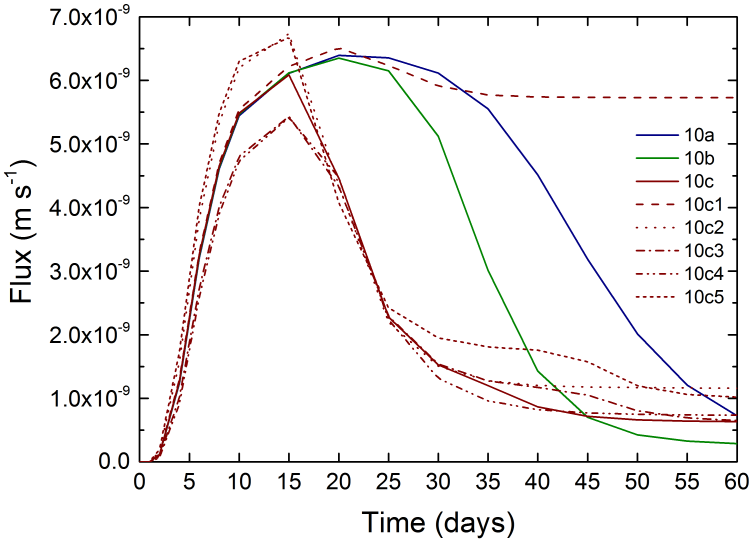

Figure B.5: Modeled HTO fluxes for different configurations tested for the 1D reactive transport model (porosity clogging) sensitivity analysis.

the sand porosity and cementation exponent. A 5% variation in either one of these parameters leads to a difference in the peak value at 15 days of 10 to 12%. The effect is also pronounced in the tailing of the flux, after the drop.

In addition to the usual parameters, the sensitivity of the model on the precipitation kinetic regime and specific surface area (SSA) of the celestite was tested. For this, the model 10c was used (which was run with precipitation kinetics), and run for celestite local equilibrium (model 10c6), and with various SSA. The SSA of the celestite precipitating in the pore space is unknown for the present system. Published data vary between 0.44 and 72.7 $m^2 g^{-1}$ (e.g. Shnel and Handlirova, 1984; Liu et al., 2005). Two commercially available powders were measured with N_2-BET in another study performed in the same laboratory, and were found to have a SSA of 0.5252 and 0.9981 $m^2 g^{-1}$. The model was run with the smallest (0.44 $m^2 g^{-1}$, model 10c7), the average (40 $m^2 g^{-1}$, model 10c) and the biggest (72.7 $m^2 g^{-1}$, model 10c8) values. Results are reported in fig. B.6. The model is only slightly dependent on the kinetic regime, the biggest difference between the 2 HTO flux curves being in the tailing, after the drop. The 2 curves seem to reach the same flux value around 60 days. In a similar way, the model in only slightly dependent on the celestite SSA. The curves for 40 and 72.7 $m^2 g^{-1}$ are very similar. The curve for the 0.44 $m^2 g^{-1}$ case is quite different, as the peak is broader: the precipitation takes about 5 additional days to influence the flux (drop). However, the minimum flux value is reached very shortly after the other cases, and the flux value reached is also very similar.

2D homogeneous model

The different configurations tested are reported in table B.5. The modeled HTO fluxes are reported in fig. B.7. The model 12a is not reported on the figure, as it did not converge. As for the 1D model, the 2D homogeneous model is very dependent on the mesh size in the X direction, but not in the Y direction (the flux curves for the runs a, b and c of each model are always

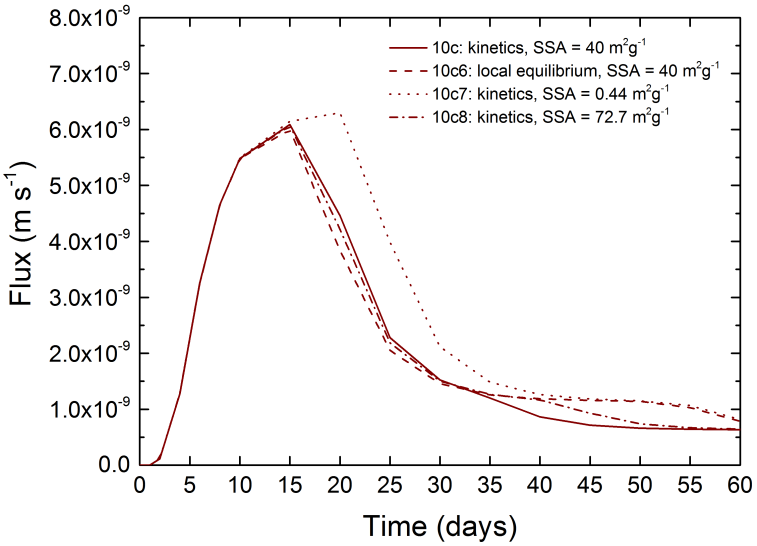

Figure B.6: Modeled HTO fluxes for different configurations tested for the 1D reactive transport model (porosity clogging) sensitivity analysis to specific surface area and precipitation kinetics of celestite.

superposed). The dependence on the porosity and cementation exponent is also the same as for the 1D model.

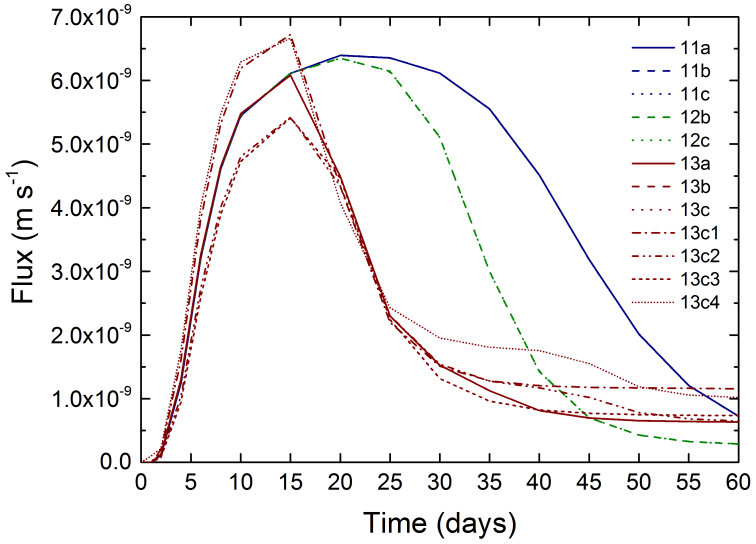

Figure B.7: Modeled HTO fluxes for different configurations tested for the 2D homogeneous reactive transport model (porosity clogging) sensitivity analysis.

Table B.5: Different configurations tested for the 2D homogeneous reactive transport model sensitivity analysis (with porosity clogging).

Model ID	Mesh size (X-Y) mm	Porosity Sand	Porosity Filter supports	Cementation exponent
11a	1.0-1.0	0.415	0.623	2.10
11b	1.0-0.5	0.415	0.623	2.10
11c	1.0-0.1	0.415	0.623	2.10
12a	0.5-1.0	0.415	0.623	2.10
12b	0.5-0.5	0.415	0.623	2.10
12c	0.5-0.1	0.415	0.623	2.10
13a	0.1-1.0	0.415	0.623	2.10
13b	0.1-0.5	0.415	0.623	2.10
13c	0.1-0.1	0.415	0.623	2.10
13c1	0.1-0.1	0.436	0.623	2.10
13c2	0.1-0.1	0.394	0.623	2.10
13c3	0.1-0.1	0.415	0.623	2.21
13c4	0.1-0.1	0.415	0.623	1.99

2D realistic model

The 2D realistic models were built as the models 7a to 9c previously presented. The different configurations tested are reported in table B.6. As only few of the models converged, no figure is presented here, and no conclusions can be drawn.

Table B.6: Different configurations tested for the 2D realistic reactive transport model sensitivity analysis (with porosity clogging).

Model ID	Mesh size (X-Y) mm	Porosity Sand	Porosity Filter supports	Cementation exponent
14a	1.0-1.0	0.415	0.623	2.10
14b	1.0-0.5	0.415	0.623	2.10
14c	1.0-0.1	0.415	0.623	2.10
15a	0.5-1.0	0.415	0.623	2.10
15b	0.5-0.5	0.415	0.623	2.10
15c	0.5-0.1	0.415	0.623	2.10
16a	0.1-1.0	0.415	0.623	2.10
16b	0.1-0.5	0.415	0.623	2.10
16c	0.1-0.1	0.415	0.623	2.10
16c1	0.1-0.1	0.436	0.623	2.10
16c2	0.1-0.1	0.394	0.623	2.10
16c3	0.1-0.1	0.415	0.623	2.21
16c4	0.1-0.1	0.415	0.623	1.99

Bibliography

Agbogun, H. M., Al, T. A., and Hussein, E. M. (2013). Three dimensional imaging of porosity and tracer concentration distributions in a dolostone sample during diffusion experiments using X-ray micro-CT. *Journal of Contaminant Hydrology*, 145:44,53.

Alt-Epping, P., Tournassat, C. andRasouli, P., Steefel, C. I., Mayer, K. U., Jenni, A., M'ader, U., Sengor, S. S., and Fernández, R. (2014). Benchmark reactive transport simulations of a column experiment in compacted bentonite with multispecies diffusion and explicit treatment of electrostatic effects. *Computers and Geosciences*, page 15.

Andra, H., Combaret, N., Dvorkin, J., Glatt, E., Han, J., Kabel, M., Keehm, Y., Krzikalla, F., Lee, M., Madonna, C., Marsh, M., Mukerji, T., Saenger, E. H., Sain, R., Saxena, N., Ricker, S., Wiegmann, A., and Zhan, X. (2013a). Digital rock physics benchmarks-part I: Imaging and segmentation. *Computers and Geosciences UK*, 50:25,32.

Andra, H., Combaret, N., Dvorkin, J., Glatt, E., Han, J., Kabel, M., Keehm, Y., Krzikalla, F., Lee, M., Madonna, C., Marsh, M., Mukerji, T., Saenger, E. H., Sain, R., Saxena, N., Ricker, S., Wiegmann, A., and Zhan, X. (2013b). Digital rock physics benchmarks-part II: Computing effective properties. *Computers and Geosciences UK*, 50:33,43.

Appelo, C. A. J., Van Loon, L. R., and Wersin, P. (2010). Multicomponent diffusion of a suite of tracers (HTO, Cl, Br, I, Na, Sr, Cs) in a single sample of Opalinus Clay. *Geochimica et Cosmochimica Acta*, 74:1201,1219.

Archie, G. E. (1942). The electric resistivity log as an aid in determining some reservoir characteristics. *Transactions AIME*, 146:54,62.

Aydogan, S., Erdemoglu, M., Aras, A., Ucar, G., and Ozkan, A. (2006). Dissolution kinetics of celestite ($SrSO_4$) in HCl solution with $BaCl_2$. *Hydrometallurgy*, 84:239,246.

Ayora, C., Caraballo, M. A., Macias, F., Rotting, T. S., Carrera, J., and Nieto, J. M. (2013). Acid mine drainage in the iberian pyrite belt: 2. lessons learned from recent passive remediation experiences. *Environmental Science and Pollution Research*, 20:7837,7853.

Balbuena, P. B. and Gubbins, K. E. (1993). Theoretical interpretation of adsorption behavior of simple fluids in slit pores. *Langmuir*, 9:1801,1814.

Barrer, R. M. (1953). A new approach to gas flow in capillary systems. *Journal of Physical Chemistry*, 57:35,40.

Becker, J., Wieser, C., Fell, S., and Steiner, K. (2011). A multi-scale approach to material modeling of fuel cell diffusion media. *International Journal of Heat and Mass Transfer*, 54:1360,1368.

Blanc, P., Lassin, A., Piantone, P., and Burnol, A. (2007a). THERMODDEM a database devoted to waste minerals. Technical report, BRGM - Orléans, France.

Blanc, P., Legendre, O., and Gaucher, E. C. (2007b). Estimate of clay minerals amounts from XRD pattern modeling:

The Arquant model. *Physics and Chemistry of the Earth*, 32:135,144.

Boving, T. B. and Grathwohl, P. (2001). Tracer diffusion coefficients in sedimentary rocks: correlation to porosity and hydraulic conductivity. *Journal of Contaminant Hydrology*, 53:85,100.

Brunauer, S., Deming, L. S., Demings, W. E., and Teller, E. (1940). On a theory of the van der Waals adsorption of gases. *Journal of the American Society*, 62:1723,1732.

Buades, A., Coll, B., and Morel, J. M. (2005). A review of image denoising algorithms, with a new one. *Multiscale Modeling and Simulation*, 4:490,530.

Crank, J. (1975). *The mathematics of diffusion.* Clarendon Press, Oxford.

Currie, J. A. (1960). Gaseous diffusion in porous media. part 2. - dry granular materials. *British Journal of Applied Physics*, 50:318,324.

Djeran-Maigre, I., Tessier, D., Grunberger, D., Velde, B., and Vasseur, G. (1998). Evolution of microstructures and of macroscopic properties of some clays during experimental compaction. *Marine and Petroleum Geology*, 15:109,128.

Dove, P. M. and Czank, C. A. (1995). Crystal chemical controls on the dissolution kinetics of the isostructural sulfates: Celestite, anglesite, and barite. *Geochimica et Cosmochimica Acta*, 59:1907,1915.

Dye, R. F. and Dallavalle, J. M. (1958). Diffusion of gases in porous media. *Industrial and Engineering Chemistry*, 50:1195,1200.

Emmanuel, S. and Ague, J. J. (2009). Modeling the impact of nano-pores on mineralization in sedimentary rocks. *Water Resources Research*, 45:W04406.

Fialips, C. and Robinet, J. C. (2011). Technical report on complete data set regarding the known physical-chemical properties of puy illite. Deliverable 1-2a, CatClay.

Flegg, P. B. (1953). The effects of aggregation on diffusion of gases and vapors through soils. *Journal of the Science of Food and Agriculture*, 4:104,108.

Gao, Z., Hu, Q., and Liang, H. (2013). Gas diffusivity in porous media: determination by mercury intrusion porosimetry and correlation to porosity and permeability. *Journal of Porous Media*, 16:607,617.

Garcia-Gutierrez, M., Mingarro, M., Missana, T., Martin, P. L., Sedano, L. A., and Cormenzana, J. L. (2004). Diffusion experiments with compacted powder/pellets clay mixtures. *Applied Clay Science*, 26:57,64.

Garrels, R. M., Dreyer, R. M., and Howland, A. L. (1949). Diffusion of ions through intergranular spaces in water-saturates rocks. *Geological Society of America Bulletin*, 60:1809,1828.

Ghanbarian, B., Hunt, A. G., Ewing, R. P., and Sahimi, M. (2013). Tortuosity in porous media: a critical review. *Soil Science Society of America Journal*, 77:1461,1477.

Gimmi, T. and Kosakowski, G. (2011). How mobile are sorbed cations in clays and clay rocks? *Envrironmental Science and Technology*, 45:1443,1449.

Glaus, M. A., Frick, S., and Jakob, A. (2012). Diffusion of moderately and strongly sorbing radionuclides in compacted illite. Deliverable 2-1, CatClay.

Glaus, M. A., Frick, S., Rossé, R., and Van Loon, L. R. (2010). Comparative study of tracer diffusion of HTO, $^{22}Na^{+}$ and $^{36}Cl^{-}$ in compacted kaolinite, illite and montmorillonite. *Geochimica et Cosmochimica Acta*, 74:1999,2010.

Guarracino, L., Rotting, T., and Carrera, J. (2014). A fractal model to describe the evolution of multiphase flow properties during mineral dissolution. *Advances in Water Resources*, 67:78,86.

Hellmuth, K. H. and Siitari-Kauppi, M. (1990). Investigation of the porosity of rocks. impregnation with ^{14}C-polymethylmethacrylate (PMMA), a new technique. STUK-B-VALO 63, Finnish Centre for Radiation and Nuclear Safety.

Hilpert, M. and Miller, C. T. (2001). Pore-morphology-based simulation of drainage in totally wetting porous media. *Advances in Water Resources*, 24:243,255.

Holliday, K., Chagneau, A., Schmidt, M., Claret, F., Schäfer, T., and Stumpf, T. (2012). Discriminating factors affecting incorporation: comparison of the fate of Eu^{3+}/Cm^{3+} in the sr carbonate/sulfate system. *Dalton Transactions*, 41:3642–3647.

Holmboe, M., Wold, S., and Jonsson, M. (2012). Porosity investigation of compacted bentonite using XRD profile modeling. *Journal of Contaminant Hydrology*, 128:19,32.

Hubbell, J. H. and Seltzer, S. M. (1995). Tables of X-Ray mass attenuation coefficients and mass energy-absorption coefficients from 1 keV to 20 MeV for elements Z = 1 to 92 and 48 additional substances of dosimetric interest. Technical report, NIST Standard Reference Database.

Hubbell, J. H. and Seltzer, S. M. (2004). Cross section data for electronpositron pair production by photons: a status re-

port. *Nuclear Instruments and Methods in Physics Research*, 213:1,9.

Indraratna, B., Pathirage, P. U., Rowe, R. K., and Banasiak, L. (2014). Coupled hydro-geochemical modeling of a permeable reactive barrier for treating acidic groundwater. *Computers and Geotechnics*, 55:429,439.

Ioannidis, M. A., Kwiecien, M. J., and Chatzis, I. (1997). Electrical conductivity and percolation aspects of statistically homogeneous porous media. *Transport in Porous Media*, 29:61,83.

IUPAC (1997). *Compendium of Chemical Terminology, 2nd edition. (the "Gold Book"). Compiled by A. D. McNaught and A. Wilkinson.* Blackwell Scientific Publications, Oxford.

Khan, F., Enzmann, F., Kersten, M., Wiegmann, A., and Steiner, K. (2012). 3D simulation of the permeability tensor in a soil aggregate on basis of nanotomographic imaging and LBE solver. *Journal of Soils and Sediments*, 12:86,96.

Klinkenberg, L. J. (1951). Analogy between diffusion and electrical conductivity in porous rocks. *Bulletin of the Geological Society of America*, 62:559,564.

Liu, S. H., Jacques, D., Govaerts, J., and Wang, L. (2014). Conceptual model analysis of interaction at a concrete-boom clay interface. *Physics and Chemistry of the Earth*, 70:150,159.

Malusis, M. A., Shackelford, C. D., and Maneval, J. E. (2012). Critical review of coupled flux formulations for clay membranes based on nonequilibrium thermodynamics. *Journal of Contaminant Hydrology*, 138:40,59.

Marshall, T. J. (1959). The diffusion of gases through porous media. *Journal of Soil Science*, 10:79,82.

Marty, N. C. M., Tournassat, C., Brunol, A., Giffaut, E., and Gaucher, E. C. (2009). Influence of reaction kinetics and mesh refinement on the numerical modelling of concrete/clay interactions. *Journal of Hydrology*, 364:58,72.

Millington, R. J. (1959). Gas diffusion in porous media. *Science*, 130:100,102.

Minagawa, H., Nishikawa, Y., Ikeda, I., Miyazaki, K., Takahara, N., Sakamoto, Y., Komai, T., and Narita, H. (2008). Characterization of sand sediment by pore size distribution and permeability using proton nuclear magnetic resonance measurement. *Journal of Geophysical Research-Solid Earth*, 113:B07210.

Molins, S., Trebotich, D., Yang, L., Ajo-Franklin, J. B., Ligocki, T. J., Shen, C. P., and Steefel, C. I. (2014). Pore-scale controls on calcite dissolution rates from flow-through laboratory and numerical experiments. *Environmental Science and Technology*, 48:7453,7460.

Montavon, G., Guo, Z., Tournassat, C., Grambow, B., and Le Botlan, D. (2009). Porosities accessible to HTO and iodide on water-saturated compacted clay materials and relation with the forms of water: A low field proton NMR study. *Geochimica et Cosmochimica Acta*, 73:7290,7302.

Navarre-Sitchler, A., Steefel, C. I., Yang, L., Tomutsa, L., and Brantley, S. L. (2009). Evolution of porosity and diffusivity associated with chemical weathering of a basalt clast. *Journal of Geophysical Research*, 114:F02016.

Oscarson, D. W. (1994). Surface diffusion: is it an important mechanism in compacted clays? *Clays and Clay Minerals*, 42:534,543.

Park, I.-S., Duong, G. D., and Rodrigues, A. E. (1996). Measurement of the effective diffusivity in porous media by the diffusion cell method. *Catalyst Reviews: Science and Engineering*, 38:189,247.

Pina, C. M. and Tamayo, A. (2012). Crystallisation of strontium sulphates from Si-bearing aqueous solutions. *Geochimica et Cosmochimica Acta*, 92:220,232.

Poinssot, C., Baeyens, B., and Bradbury, M. H. (1999). Experimental and modelling studies of caesium sorption on illite. *Geochimica et Cosmochimica Acta*, 63:3217,3227.

Prêt, D. (2003). Nouvelles mthodes quantitatives de cartographie de la minralogie et de la porosit dans les matriaux argileux: application aux bentonites compactes des barrires ouvrages. Technical report, University of Poitiers, France.

Prieto, M., Fernandez-Gonzalez, A., and Martin-Diaz, R. (2002). Sorption of chromate ions diffusing through barite-hydrogel composites: Implications for the fate and transport of chromium in the environment. *Geochimica et Cosmochimica Acta*, 66:783,795.

Prieto, M., Fernandez-Gonzalez, A., Putnis, A., and Fernandez-Diaz, L. (1997). Nucleation, growth, and zoning phenomena in crystallizing (Ba,Sr)CO_3, Ba(SO_4,CrO_4), (Ba,Sr)SO_4, and (Cd,Ca)CO_3 solid solutions from aqueous solutions. *Geochimica et Cosmochimica Acta*, 61:3383,3397.

Putnis, A., Prieto, M., and Fernandez-Diaz, L. (1995). Fluid supersaturation and crystallization in porous media. *Geological Magazine*, 132:1,13.

Reible, D. D. and Shair, F. H. (1982). A technique for the measurement of gaseous diffusion in porous media. *Journal of Soil Science*, 33:165,174.

Rotenberg, B., Marrya, V., Vuilleumierc, R., Malikovad, N., Simona, C., and Turqa, P. (2007). Water and ions in clays: Unraveling the interlayer/micropore exchange using molecular dynamics. *Geochimica et Cosmochimica Acta*, 71:5089,5101.

Rust, R. H., Klute, A., and Gieseking, J. E. (1957). Diffusion-porosity measurements using a non-steady state system. *Soil Science*, 84:453,463.

Saenger, E. H., Enzmann, F., Keehm, Y., and Steeb, H. (2011). Digital rock physics: Effect of fluid viscosity on effective elastic properties. *Journal of Applied Geophysics*, 74:236,241.

Sammartino, S., Siitari-Kauppi, M., Meunier, A., Sardini, P.and Bouchet, A., and Tevissen, E. (2002). An imaging method for the porosity of sedimentary rocks: adjustment of the pmma method - example of a characterization of a calcareous shale. *Journal of Sedimentary Research*, 72:937,943.

Sell, K., Enzmann, F., Kersten, M., and Spangenberg, E. (2013). Microtomographic quantification of hydraulic clay mineral displacement effects during a CO_2 sequestration experiment with saline aquifer sandstone. *Environmental Science and Technology*, 47:198,204.

Shackelford, C. c. and Moore, S. M. (2013). Fickian diffusion of radionuclides for engineered containment barriers: Diffusion coefficients, porosities, and complicating issues. *Engineering Geology*, 152:133,147.

Shao, H. B., Kosakowski, G., Berner, U., Kulik, D. A., Mader, U., and Kolditz, O. (2013). Reactive transport modeling of the clogging process at maqarin natural analogue site. *Physics and Chemistry of the Earth*, 64:21,31.

Shearer, R. C., Millington, R., and Quirk, J. P. (1965). Oxygen diffusion through sands in relation to capillary hysteresis:

2. quasi-steady-state diffusion of oxygen through partly saturated sands. *Soil Science*, 101:432,436.

Sposito, G. (2004). *The surface chemistry of natural particles*. Oxford University Press, New York.

Stack, A. G., Fernandez-Martinez, A., Allard, L. F., Bañuelos, J. L., Rother, G., Anovitz, L. M., Cole, D. R., and Waychunas, G. A. (2014). Pore-size-dependent calcium carbonate precipitation controlled by surface chemistry. *Environmental Science and Technology*, 48:6177,6183.

Steefel, C. I. (2009). *CrunchFlow - Software for modeling multicomponent reactive flow and transport - User's manual*. Lawrence Berkeley Natianal Laboratory.

Steefel, C. I. and Lasaga, A. C. (1994). A coupled model for transport of multiple chemical species and kinetic precipitation dissolution reactions with application to reactive flow in single-phase hydrothermal systems. *American Journal of Science*, 294:529,592.

Steefel, C. I. and Lichtner, P. C. (1998). Multicomponent reactive transport in discrete fractures - ii: Infiltration of hyperalkaline groundwater at maqarin, jordan, a natural analogue site. *Journal of Hydrology*, 209:200,224.

Sun, J., Sun, R., Z., X., and Du, H. (2012). Facile room temperature morphology-controlled synthesis of srso4 microcrystals. *CrystEngComm*, 14:1111,1116.

Tournassat, C. and Appelo, C. A. J. (2011). Modelling approaches for anion-exclusion in compacted na-bentonite. *Geochimica et Cosmochimica Acta*, 75:3698,3710.

Tyagi, M., Gimmi, T., and Churakov, S. V. (2013). Multi-scale micro-structure generation strategy for up-scaling transport in clays. *Advances in Water Resources*, 59:181,195.

Van Laer, E., Bruggeman, C., Maes, N., and Aertsens, M. (2014). Diffusion of sorbing tracers in compacted clay. Deliverable 2-3, CatClay.

VanBavel, C. H. M. (1952). Gaseous diffusion and porosity in porous media. *Soil Sciences*, 73:91,104.

VanLoon, L. R., Glaus, M. A., and M$'$uler, M. H. (2007). Anion exclusion effects in compacted bentonites: Towards a better understanding of anion diffusion. *Applied Geochemistry*, 22:2536,2552.

VanLoon, L. R., Soler, J. M., and Bradbury, M. H. (2003a). Diffusion of HTO, $^{36}Cl^-$ and $^{125}I^-$ in Opalinus Clay sample from Mont Terri: effect of confining pressure. *Journal of Contaminant Hydrology*, 61:73,83.

VanLoon, L. R., Soler, J. M., Jakob, A., and Bradbury, M. H. (2003b). Effects of confining pressure on the diffusion of hto, $^{36}Cl^-$ and $^{125}I^-$ in a layered argillaceous rock (Opalinus clay): diffusion perpendicular to the fabric. *Applied Geochemistry*, 18:1653,1662.

Vasseur, G., Djeran-Maigre, I., Grunberger, G., Rousset, G., Tessier, D., and Velde, B. (1995). Evolution of structural and physical parameters of clays during experimental compaction. *Marine and Petroleum Geology*, 12:941,954.

Wasch, L. J., Wollenweber, J., and Tambach, T. J. (2013). Intentional salt clogging: a novel concept for long-term CO_2 sealing. *Greenhouse Gases*, 3:491,502.

Wiegmann, A. and Becker, J. (2012). GeoDict 2012 - DiffuDict tutorial. computing tortuosity factor and effective diffusivity with DiffuDict. Technical report, MATH2MARKET - Fraunhofer ITWM.

Wiegmann, A., Glatt, E., Becker, J., and Westerteiger, R. (2013). GeoDict 2012 - PoroDict tutorial. calculating pore structure characteristics with PoroDict. Technical report, MATH2MARKET - Fraunhofer ITWM.

Xie, M. L., Kolditz, O., and Moog, H. C. (2011). A geochemical transport model for thermo-hydro-chemical (THC) coupled processes with saline water. *Water Resources*, 47:14.